OCEAN ENGINEERING GROUP

Modeling of Unsteady Wake Alignment and Developed Tip Vortex Cavitation

Hanseong Lee

August 2002

Report No. 02–4

ENVIRONMENTAL AND WATER RESOURCES ENGINEERING

DEPARTMENT OF CIVIL ENGINEERING

THE UNIVERSITY OF TEXAS AT AUSTIN

Austin, TX 78712

The Dissertation Committee for Hanseong Lee
Certifies that this is the approved version of the following dissertation:

Modeling of Unsteady Wake Alignment and Developed Tip Vortex Cavitation

Committee:

Spyros A. Kinnas, Supervisor

David R. Maidment

John L. Tassoulas

Ronald L. Panton

Leszek F. Demkowicz

Modeling of Unsteady Wake Alignment and Developed Tip Vortex Cavitation

by

Hanseong Lee, B.S., M.S.

DISSERTATION

Presented to the Faculty of the Graduate School of

The University of Texas at Austin

in Partial Fulfillment

of the Requirements

for the Degree of

DOCTOR OF PHILOSOPHY

THE UNIVERSITY OF TEXAS AT AUSTIN

August 2002

"I am the way and the truth and the life.

No one comes to the Father except through me.

If you really knew me, you would know my Father as well.

From now on, you do know him and have seen him."

(John 14:6-7)

To my Lord,

and

To my family

Acknowledgments

First, I would like to thank my supervisor, Professor Spyros A. Kinnas. He continuously encouraged and inspired me to further efforts through out the years of my graduate school. His insightful comments and bright ideas always guided me onto the right path for solving problems.

I would also like to thank the other committee members: Professor David R. Maidment, Professor John L. Tassoulas from Civil Engineering, Professor Ronald L. Panton from Mechanical Engineering, and Professor Leszek F. Demkowicz from Aerospace and Engineering Mechanics. They reviewed the draft of my dissertation and gave me invaluable comments.

I would like to thank my previous advisor at Seoul National University, Professor KwangJune Bai, for his invaluable advice and incredible humor.

Many thanks goes out to all of Korean students (aka *Korean Mafia*) of Civil Engineering at UT austin for their friendship and assistance.

I also express my thanks to my friends at the CHL for all the nights we spent working together in the *Computational Hydrodynamics Laboratory*

Many thanks are extended to my high school friends who keep me posted on news from my home country.

I would like to express my love to my family. I am much indebted to my

wife, Hyunkyung, for serving and sacrificing her life to me. I also express my love to my children, Jiwon and Clare (Hannah), who make me happy everyday. My love and the profound gratitude goes to my parents and parents-in-law who pray everyday for my family.

Modeling of Unsteady Wake Alignment and Developed Tip Vortex Cavitation

Publication No. ⎯⎯⎯⎯⎯⎯⎯⎯

Hanseong Lee, Ph.D.
The University of Texas at Austin, 2002

Supervisor: Spyros A. Kinnas

A low order potential based boundary element method is applied for the numerical modeling of unsteady sheet and developed tip vortex cavitation, including fully unsteady wake alignment, on hydrofoils and marine propellers.

For the alignment of trailing wake, a finite core tip vortex is introduced at the tip of the wake sheet, and the induced velocities are evaluated at slightly deviated points instead of the actual control points on the panels, in order to avoid the numerical instability near the roll-up region.

Once the Green's formula for the perturbation potential is solved on the lifting bodies and the tip vortex surface, the three-component velocities on the tip vortex surface are calculated by numerically differentiating the given perturbation potentials. The induced velocities on the wake surface are directly determined by differentiating Green's formula. The new locations of the wake sheet and of the

center of tip vortex core are then determined by aligning them to the flow so that the force-free condition is satisfied on the wake.

The wake surface is aligned in an iterative manner, and then the shapes of the blade sheet and tip vortex cavities are determined by applying the dynamic and the kinematic boundary conditions on the cavity surfaces. The potentials on the blade sheet cavities are determined from the dynamic boundary condition (Dirichlet type), and the normal derivatives of the potentials are obtained from the solution of Green's formula. Finally, the extent and thickness of the blade sheet cavity surface is determined from the kinematic boundary condition (Neumann type).

On the other hand, the boundary value problem on the developed tip vortex cavity is solved for the perturbation potential by assuming at first that the tip vortex is a solid body of given radius. The tip vortex cavity shape is then adjusted so that the pressures match the given cavity (vapor) pressure, using a method based on the Jacobian of the pressures with respect to the cavity height adjustments. The blade sheet and the tip vortex cavity shapes are determined in an iterative manner at each time step, until both the dynamic and the kinematic boundary conditions are satisfied.

The method is applied in the case of 2-D vortex, 3-D hydrofoil, and marine propellers subjected to inclined and non-axisymmetric inflows. Comparisons with experiments are presented, and the dependence of numerical solutions on the computational parameters is studied extensively.

Table of Contents

List of Tables

List of Figures

Nomenclature

Latin Symbols

AR   Aspect Ratio

C chord length at each section for 3-D hyrofoil

C_o chord length at mid-span of 3-D hydrofoil

C_p pressure coefficient,

$C_p = (P - P_o)/(0.5\rho n^2 D^2)$ for propeller

$C_p = (P - P_o)/(0.5\rho U_\infty^2)$ otherwise

D propeller diameter, $D = 2R$

F_n Froude number based on n, $F_n = n^2 D/g$

g gravitational acceleration

G Green's function

h cavity thickness over the blade surface

h_w cavity thickness over the wake surface

J_s advance ratio based on V_s, $J_s = V_s/nD$

K_Q torque coefficient, $K_Q = Q/\rho n^2 D^5$

K_T thrust coefficient, $K_T = T/\rho n^2 D^4$

n propeller rotational frequency (rev/s)

P pressure

P_{atm} atmospheric pressure

P_c cavitating pressure

P_o	far upstream pressure, at the propeller axis
P_v	vapor pressure of water
p, q	field point and variable point
$\vec{q_t}$	total velocity
Q	propeller torque
r	radius of propeller blade section
r_T	radius of tip vortex core
$(r_T)_{mean}$	mean radius of tip vortex core
R	propeller radius or half span of 3-D hydrofoil
R_e	Reynolds number based on U_∞, $R_e = U_\infty D/\nu$
R_n	Reynolds number based on n, $R_n = nD^2/\nu$
$\vec{s}, \vec{v}, \vec{n}$	non-orthogonal unit vectors along the
	local grid directions
S_B	blade surface
S_C	partial or super cavity surface
S_H	hub surface for propeller
	foil surface for 3-D hydrofoil
S_T	tip vortex cavity surface
S_W	wake surface
S_{WS}	wetted portion of blade and hub surfaces
s, v, n	non-orthogonal coordinates on local panel
s, w, n	orthogonal coordinates on local panel
s, u, n	orthogonal coordinates on local wake panel
t	time

T	propeller thrust
t_{max}	maximum thickness at each secion for 3-D hydrofoil
$\vec{U}_{in}$	local inflow velocity (in the propeller fixed system)
$\vec{U}_{\infty}$	inflow velocity for 3-D hydrofoil
U_{up}	magnitude of upwind velocity
$\vec{U}_{w}$	effective inflow velocity (in the ship fixed system)
$\vec{u}_{wi}$	induced velocity on wake surface
V_s	ship speed
$\vec{V}_{Tip}$	total velocity at the center of tip vortex core
$\vec{V}_{w}$	total velocity on wake surface
v_{max}	total arclength of tip vortex circumference
x, y, z	propeller fixed coordinates
x_s, y_s, z_s	ship fixed coordinates
x_{TE}	x-coordinate of 3-D hydrofoil or propeller trailing edge

Greek Symbols

α	angle of attack for 3-D hydrofoil
α_{up}	angle corresponding to the upwind velocity
δ	cavity trailing edge thickness for cavity problem
	distance between actual and virtual control points
	on wake surface
Δs	distance between adjacent node points
$\delta t, \Delta t$	time step size
$\Delta \theta$	blade angle increment, $\Delta \theta = \omega \Delta t$
$\Delta x, \Delta y, \Delta z$	difference of (x, y, z) coordinates
	between adjancent node points
γ	vorticity
Γ	circulation
ω	propeller angular velocity
ν	kinematic viscosity of water
ϕ	perturbation potential
Φ	total potential
ψ	angle between $\vec{w}$ and $\vec{v}$
ρ	fluid density
σ_n	cavitation number based on n,
	$\sigma_n = (P_o - P_c)/(0.5\rho n^2 D^2)$
σ	cavitation number based on U_∞,
	$\sigma = (P_o - P_c)/(0.5\rho U_\infty^2)$

Superscripts

$+$	upper cavity, or wake surface
$-$	lower cavity, or wake surface

Acronyms

BEM	Boundary Element Method
BVP	Boundary Value Problem
CPU	Central Processing Unit (time)
DTMB	David Taylor Model Basin
FLAG	FLow Adaptive Grid
FVM	Finite Volume Method
LDV	Laser Doppler Velocimetry
NACA	National Advisory Committee for Aeronautics
PIV	Particle Image Velocimetry
VLM	Vortex-Lattice Method

Computer Program Names

MPUF-3A	cavitating propeller potential flow solver (VLM)
PROPCAV	cavitating propeller potential flow solver (BEM)
PUF-3	propeller unsteady potential flow solver (VLM)
WAKEFF-3D	effective wake solver (FVM)

Chapter 1

Introduction

1.1 Background

A marine propeller is often operating in a non-axisymmetric flow field and thus its blades are subject to an unsteady flow. Depending on operating conditions, such as ship speed, propeller submergence depth, rotational velocity of propeller, and ship maneuvering conditions, the propeller can experience different types of cavitation. The most destructive effect of cavitation on the propeller blades occurs when the cavity repeatedly grows and collapses on the propeller surface. Excessive pressures during the collapse stage cause pitting of the blades and thus accelerate blade erosion. In addition, the hydrodynamic phenomenon of the growth and the collapse of the cavity can produce severe pressure fluctuations on the adjacent hull that sometimes can cause failure of the hull panels as well as radiating noise.

Although designing a propeller without cavitation is the primary goal of propeller designers, avoiding cavitation has become more difficult in recent years, due to the development of faster and larger displacement ships. As a result, propellers have been designed to avoid excessive cavitation by allowing some portion of cavitation on the blades. Therefore the development of a computational method which can accurately predict propeller performance, including cavitation, is essential for

the design process.

The following types of cavitation patterns can occur on the propeller blades, depending on operating conditions: sheet, bubble, cloud, hub vortex and tip vortex cavitation [Carlton 1994].

Blade sheet cavitation initially appears at the leading edge of the propeller blade on the suction side, if the propeller operates at a positive angle of attack. As the angle of attack increases, or the cavitation number decreases, sheet cavitation grows over the blade surface and forms a super-cavity which extends downstream of the propeller blade trailing edge. Partial and super cavitation are shown in Figs. 1.1-(a) and -(b)[1].

Bubble cavitation usually occurs in the mid chord region of the blade section, around which the blade section usually has its maximum thickness and camber (Fig. 1.1-(c)).

Cloud cavitation appears downstream of strongly developed sheet cavitation as the form of a mist or a cloud of very small bubbles. Cloud cavitation is known as the main cause of blade surface erosion (Fig. 1.1-(d)).

Hub vortex cavitation is generated in the strong hub vortex which results from the merging of the circulation at the root of each blade. The resulting cavitation is very stable and forms a rope-like shape with strands corresponding to the number of propeller blades.

---

[1]Photographs shown in Figs. 1.1 and 1.2 are taken from the following web site with permission by Professor Hiroharu Kato. http://www.fluidlab.naoe.t.u-tokyo.ac.jp/Research/CavPictures/

The flow around the blade tip, from the pressure to the suction side, produces also a vortex (the tip vortex) which extends from the blade tip to the flow field downstream. Often, a tip vortex cavity starts cavitating somewhat downstream of the propeller trailing edge in a detached form (tip vortex cavitation inception) [Arndt et al. 1991]. As the cavitation number decreases, the detached tip vortex cavity moves closer and closer to the trailing edge of the blade, and finally attaches to the tip of the blade (developed tip vortex cavitation). A developed tip vortex cavity on a hydrofoil is shown in Fig. 1.2.

Developed tip vortex cavitation often appears together with blade sheet cavitation, and is known as one of the main sources of propeller induced pressure fluctuations on the ship hull. The prediction of developed tip vortex cavity shape is thus quite important in the assessment of the propeller performance and the corresponding ship hull pressure fluctuations.

While the developed cavitating tip vortex is swept away with the flow, it often shows a growing vortex core (so called *vortex bursting*) in wake peak region, as shown in Fig. 1.3. The vortex bursting behavior shown in photographs was observed on a 5-bladed controllable propeller of a Navy oiler [Kuiper 2001].

It is well known that the trailing wake sheet traveling downstream of a propeller blade experiences contraction and roll-up at the tip region. In the past, the wake contraction and vortex roll-up motion were determined from measurements by using Laser Doppler Velocimetry(LDV) or more recently Particle Image Velocimetry(PIV) systems. The results of these measurements were used to adjust simplified techniques which determine the location of the trailing wake sheet. Since the roll-
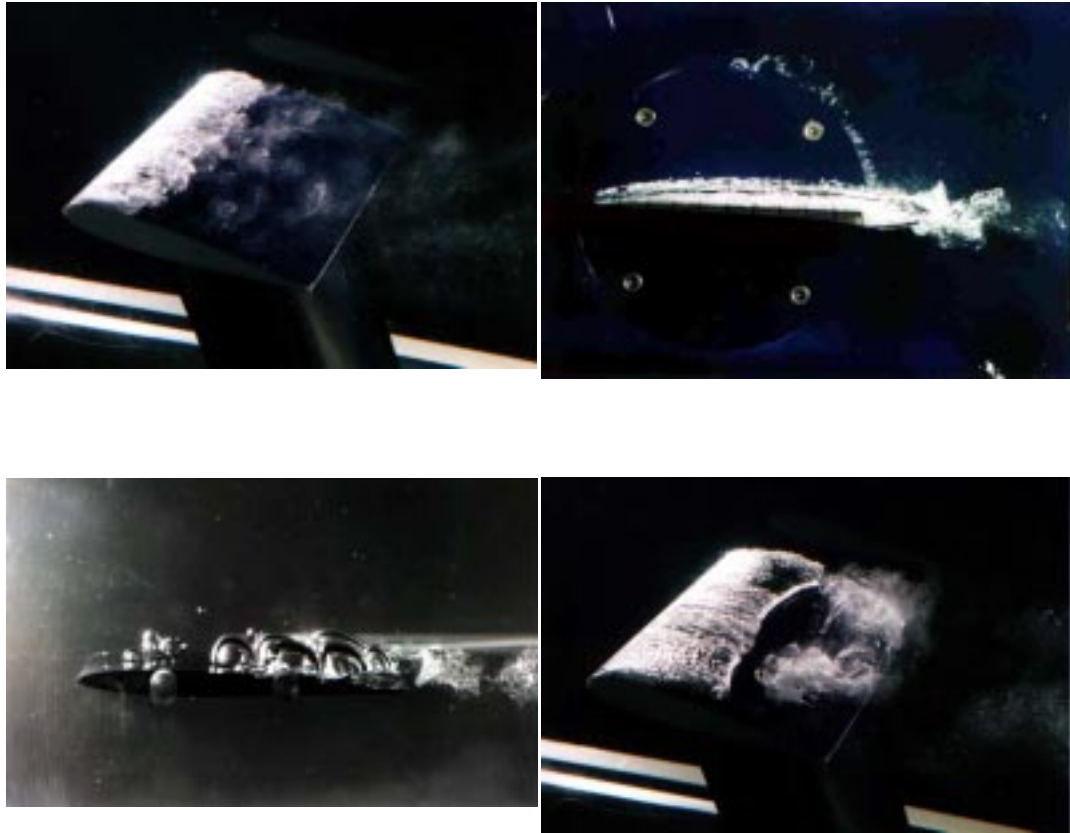
Figure 1.1: Types of cavitation on 3-D hydrofoil. (a) partial cavitation (top left), (b) super cavitation (top right), (c) bubble cavitation (bottom left), and (d) sheet and cloud cavitation (bottom right). With permission by Professor Hiroharu Kato.
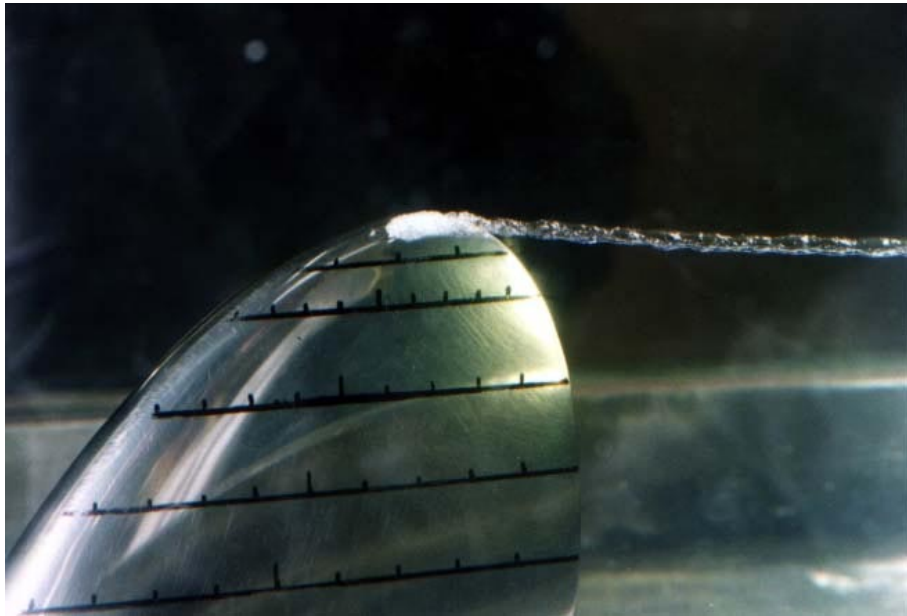
Figure 1.2: Tip vortex cavitation on 3-D hydrofoil. With permission by Professor Hiroharu Kato.

up and the contraction of vortex (wake) sheet depend on the propeller operating conditions and the geometric characteristics, the range in which the experimental measurements are applicable to the numerical calculation is confined to the near design condition of a propeller.

More recently, the accurate prediction of the wake geometry has been achieved by aligning the wake surface with the local total velocities, i.e. by applying the force-free condition on the wake surface. Since the trajectory of a tip vortex in non-cavitating conditions has been found to be close enough to that of cavitating conditions [Arndt et al. 1991], the wake alignment in a non-cavitating flow can also predict the trajectory of the cavitating tip vortex[2].

---

[2]This would be valid for limited amount of blade sheet cavitation so that the blade loading is not
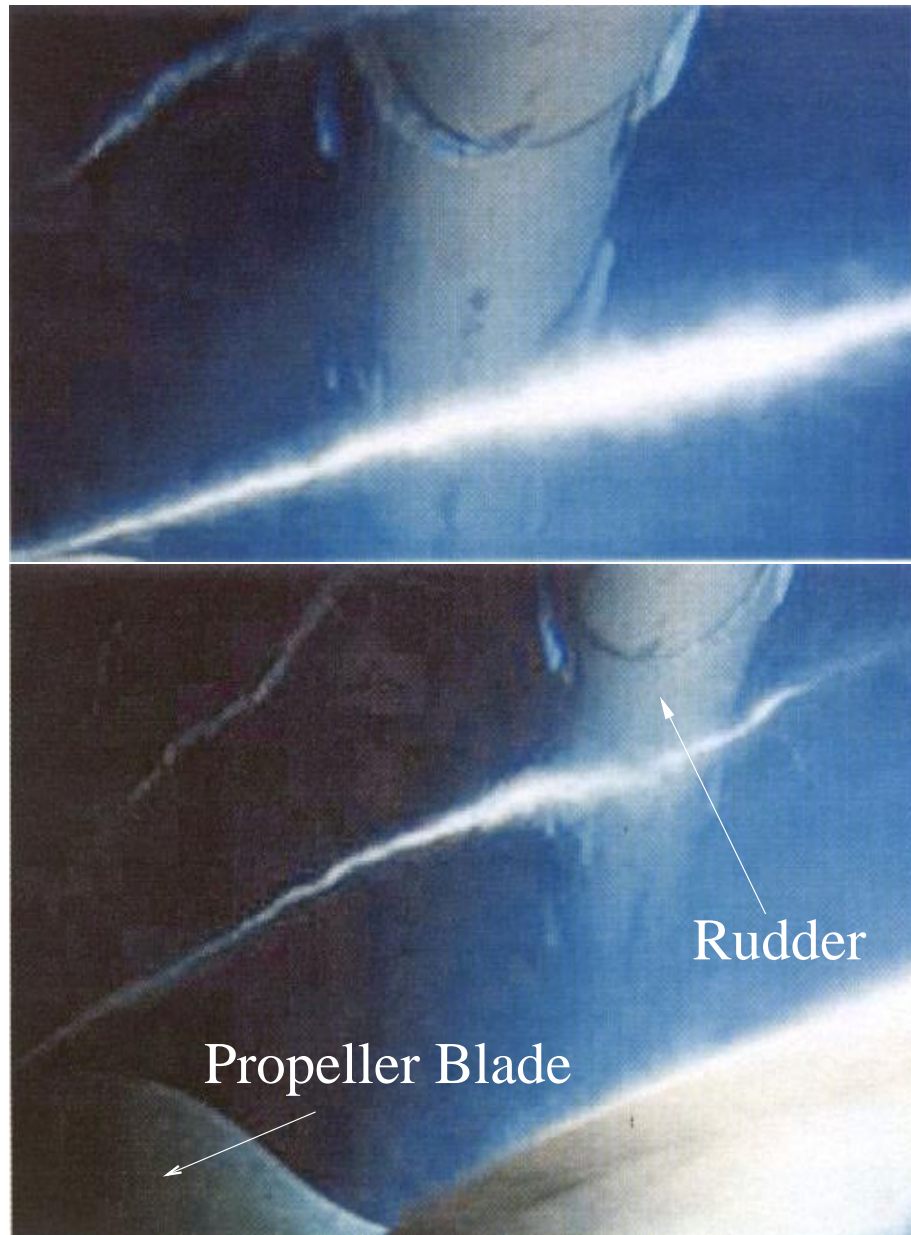
Figure 1.3: Blown up tip vortex cavity (tip vortex cavity bursting) observed on a Navy oiler with 5 bladed controllable propeller. Taken from [Kuiper 2001].

In this study, the aligned wake geometry is first determined in a fully unsteady manner to locate the trajectory of the tip vortex cavitation. The geometries of the blade sheet and developed tip vortex cavities are then determined by satisfying a constant pressure condition on their surfaces.

1.2 Motivation

Despite the fact that in most cases the inflow is non-axisymmetric, the mean performance of a marine propeller has often been predicted in steady (circumferentially averaged) flow. Even in unsteady analysis, however, the geometry of the trailing wake sheet has been treated as frozen, i.e. the wake is determined in the circumferentially averaged flow field and retained the same for all time steps (or blade angles). Especially, in the case of inclined shaft flow, the wake travels from the blade trailing edge at an inclined angle, and the variation of the predicted unsteady forces strongly depends on the wake geometry. Since the trajectory of the tip vortex core of non-cavitating condition has been found to coincide with that of cavitating condition, the accurate prediction of the wake roll-up and contraction is important for the performance prediction of non-cavitating as well as cavitating propeller.

The most common problems due to the blade sheet and developed tip vortex cavitation are excessive pressure fluctuations (broadband excitations) of the hull, and erosion [Kuiper 2001]. The pressure fluctuations generated by the tip vortex cavitation show broadband behavior, i.e. energy is radiated in all frequencies, while

---

altered.

the pressure fluctuations due to sheet cavitation radiate noise at the blade frequency or multiples of that. Even though the excitations due to the blade sheet cavitation are predominant, these excitations can be reduced by increasing tip loading, i.e. by moving loading towards blade tip, and consequently, the blade erosion due to the sheet cavitation can be controlled. However, increasing tip loading results in broadband pressure fluctuations due to the generation of strong tip vortex cavitation.

The main benefit from this work is a better understanding of the hydrodynamic characteristics of blade sheet and developed tip vortex cavitation. Furthermore, the outcome of this work will lead to a better prediction of the fluctuating pressures generated by blade sheet and tip vortex cavitation, and those effects will be considered in the propeller design stage.

1.3   Objective

The objective of this research is to develop a robust and computationally stable numerical method which can predict unsteady propeller sheet and fully developed tip vortex cavitation, and their effects on the hydrodynamic forces.

The following assumptions or approaches are implemented in order to achieve the main objective.

- The fluid domain is numerically modeled via a low order panel method based on the perturbation velocity potential.

- The trailing wake sheet is determined to satisfy the force-free condition, and modeled in an unsteady manner.

- The exact shapes of blade sheet and fully developed tip vortex cavitation are predicted by applying Neumann and Dirichlet type of boundary conditions on the aligned unsteady wake geometries.

- The range of applicability of present method is tested by comparisons with experiments and other numerical methods.

1.4 Overview

This dissertation is organized into four main chapters.

Chapter 1 contains background, motivation, objectives of this research.

Chapter 2 introduces two- and three-dimensional formulations for the wake alignment based on a boundary element method. Then, the numerical results obtained for the two dimensional vortex, the three dimensional hydrofoil and the propeller problems are presented, and compared with those of experiments and other numerical methods.

In Chapter 3, the details of the mathematical formulations for the blade sheet and the developed tip vortex cavitation are described. Numerical validation tests and comparisons with experiments are addressed in the cases of 2-D tip vortex cavity, 3-D hydrofoil, and propeller.

In Chapter 4, a method for the modeling of the unsteady 2-D tip vortex cavity bursting is proposed, as a part of recommendations for future work, and the preliminary results are also presented.

Chapter 5 presents the conclusions and contributions of this dissertation, and the recommendations for future research.

Chapter 2

Unsteady Wake Alignment

2.1 Previous Research

This section presents a literature review on computational studies which have been conducted on the subjects of vortex roll-up and wake alignment. The previous works on two dimensional vortex roll-up motion are reviewed first. Later, a review of research on three dimensional wake alignment is given.

2.1.1 Two Dimensional Vortex Roll-Up

[Westwater 1935] was first to evaluate numerically vortex sheet roll-up behind an elliptically loaded wing by using the discretized point vortex approximation of [Rosenhead 1931]. [Batchelor 1964] described the vortex rolling up process including the effects of wing viscous wake, in which the central core vortex was assumed to be laminar and the velocity field to be that of a concentrated line vortex. A spiral structure for the vortex sheet near the tip was predicted and the rate of roll-up of the vortex sheet was estimated. However, this method with increasing number of point vortices and smaller time step resulted in chaotic motion in the region of tip vortex [Takami 1964; Moore 1971]. In order to prevent the chaotic motion in the region of tip vortex, [Chorin and Bernard 1973] introduced a finite core model for the vortices, and desingularized the Cauchy principal value integral

11

for the velocity. [Kuwahara and Takami 1973] stabilized the numeric calculation by smoothing the point vortex velocity, and [Clements and Maull 1973] prevented chaotic motion by using a time step comparable with the orbital period of the closest vortices. Also, the effects of the loading along the span on the development of fully rolled-up trailing vortices were discussed by [Brown 1973].

[Moore 1974, 1975; Guiraud and Zeytounian 1977] also eliminated the chaotic motion by introducing a finite core tip vortex to represent the rolling up of the vortex sheet. Their results showed good agreement with Kaden's solution [Kaden 1931] which was derived from asymptotic expression for the roll-up spiral. Also, they found that the inner turns of the spiral were not circular, but were elliptical, and that effect was also observed by [Smith 1968] who studied steady leading edge separation from slender thin delta wings [Mangler and Smith 1959]. [Pullin 1978; Pullin and Phillips 1981] studied the roll-up of an initially planar semi-infinite vortex sheet using similarity solutions. The known similarity solutions were used to transform the time-dependent problem for the vortex sheet motion into an integro-differential equation which was approximated by finite difference method. Their vortex rolling-up showed good agreement with Kaden's asymptotic spiral solution. [Fink and Soh 1978] proposed to use re-discretization of the vortex sheet, which includes the consideration of Cauchy principal value integration and higher order terms. They obtained smooth vortex sheet behavior which included coherent spiral roll-up over longer times than previously reported. Later, [Baker 1980] investigated the stability of the re-discretization method for the case of double-branched spiraling vortex sheets, and proved that Fink & Soh's method eventually led to chaotic

12

motion as well.

A successful method which predicted two dimensional vortex sheet evolution was developed by [Krasny 1986, 1987]. He introduced a vortex blob method based on the desingularization of the Cauchy principal value integral which defines the vortex sheet velocity. Results showed good convergence with respect to refinement in the mesh size and the smoothing parameter. [McCune et al. 1990] also applied the desingularization method to compute the trailing wake behind two dimensional hydrofoil in unsteady motion.

In general, high order boundary element method produces more stable and smooth vortex roll-up than that of vortex lattice method. There have been several attempts to compute vortex sheet roll-up motion by using boundary element method.

[Mokry and Rainbird 1975] attempted to produce vortex roll-up using a low order panel method, however, their results showed numerical instability near the vortex roll-up region. [Hoeijmakers and Vaatstra 1983] introduced a second order panel method to compute the motion of the vortex sheets, and successfully computed up to four outer turns in the vortex sheet. However, a disadvantage of this method was that the solution was not self-starting and required an initial condition based on Kaden's asymptotic solution. [Nagati et al. 1987; Pyo 1995; Pyo and Kinnas 1997] presented vortex sheet modeling with curved higher order panels by distributing continuous vorticity on the curved panels. They eliminated the irregularities near the tip by introducing a smoothing scheme.

2.1.2 Three Dimensional Vortex Roll-Up

There have been many attempts to predict vortex roll-up behind three dimensional lifting bodies, and those efforts are systematically described by [Smith 1986].

A vortex lattice method has been applied to a wide range of configurations, and achieved reasonable success in predicting a vortex roll-up motion [Zhu et al. 1981; Rom et al. 1981; Almosnino 1985; Kandil 1985; Keenan 1989]. [Tavares and McCune 1993] extended classical slender wing theory, and used a desingularized method to predict leading edge vortices over slender wing. Also, a desingularization method was applied by [Ramsey 1996] to predict three dimensional vortex sheet evolution, where the relationship of the desingularized radius to the other mesh parameters, such as time step size, were also discussed. [Rule and Bliss 1998] incorporated a differential equation for inviscid roll-up with an integral conservation law model in the viscous core region. Although their model was validated for several experimental cases, the method required some care in the choice of viscous core velocity function which was one of the initial conditions.

High order panel methods were used by [Suciu and Morino 1977; Hoeijmakers and Bennekers 1979; Johnson et al. 1980] to model the trailing vortex sheet over wings with leading edge separation. [Pyo 1995; Pyo and Kinnas 1997] developed a three dimensional vortex sheet roll-up algorithm by using hyperboloidal panels and bi-quadratic dipole distribution over the trailing vortex sheet.

14

2.1.3 Wake Alignment on Propeller

A trailing wake sheet traveling downstream of a propeller experiences contraction and roll-up at the tip regions. In the past, the wake contraction and vortex roll-up motion were determined from measurements by Laser Doppler Velocimetry(LDV), or Particle Image Velocimetry(PIV). These measurements were used to adjust simplified techniques which determine the location of the trailing wake sheet.

There has been a lot of research on aligning wake geometry to predict more accurate propeller performance in uniform inflows. The effect of wake geometry on the predicted propeller torque and thrust was first investigated by [Kerwin and Lee 1978]. [Greeley and Kerwin 1982] applied a vortex lattice method to determine the trailing wake geometry of a propeller in axisymmetric inflow in an iterative manner. In their method, the roll-up of the vortex sheet was artificially suppressed by aligning the wake with the flow at the trailing edge and far downstream, and by interpolating the wake geometry in between. This modeling was extended by [Kinnas and Pyo 1999] to predict unsteady forces and moments of a propeller subjected to inclined inflows, by including the effects of shaft inclination on the radial and the tangential velocities used to align the wake sheet. Their predicted unsteady forces (first harmonics) showed good agreement with those measured in the experiment performed by [Boswell et al. 1984]. [Keenan 1989] calculated the trailing wake geometry produced by propellers in unsteady flow using a vortex lattice model. In his work, he set the induced velocity at the wake grid points to zero when a vortex point is within the prescribed cutoff radius. In addition, the damping function was introduced to suppress spurious extreme velocities. The desingularization method

was applied by [Ramsey 1996], to predict three dimensional vortex sheet evolution on propellers in uniform flow, where the relationship of the desingularized radius to the other mesh parameters such as time step size were also discussed. [Pyo and Kinnas 1997] developed a three dimensional vortex sheet roll-up algorithm for propellers in steady flow using a high order panel method, in which quadratic dipoles were distributed on the trailing vortex sheet.

2.2   Objectives

As mentioned in Section 2.1, the geometry of the wake sheet trailing from a propeller blade was generated based on user specified parameters that were obtained from the experiments. These methods have been widely used in propeller design and performance analysis. However, due to the increasing complexity of propeller geometry and higher propeller loadings, and considering that the inflow is often non-uniform and non-axisymmetric, the predicted forces from these methods were often far away from those measured in the experiments. Therefore, more reliable and robust wake aligning method is needed for the accurate prediction of propeller performance. The followings are the main objectives of this section :

- Develop a numerical algorithm which predicts vortex roll-up motion in 2-D.

- Extend the BEM to predict the aligned wake geometry of a 3-D hydrofoil.

- Extend the BEM to predict steady and unsteady geometry of the trailing wake sheet on propellers.

16
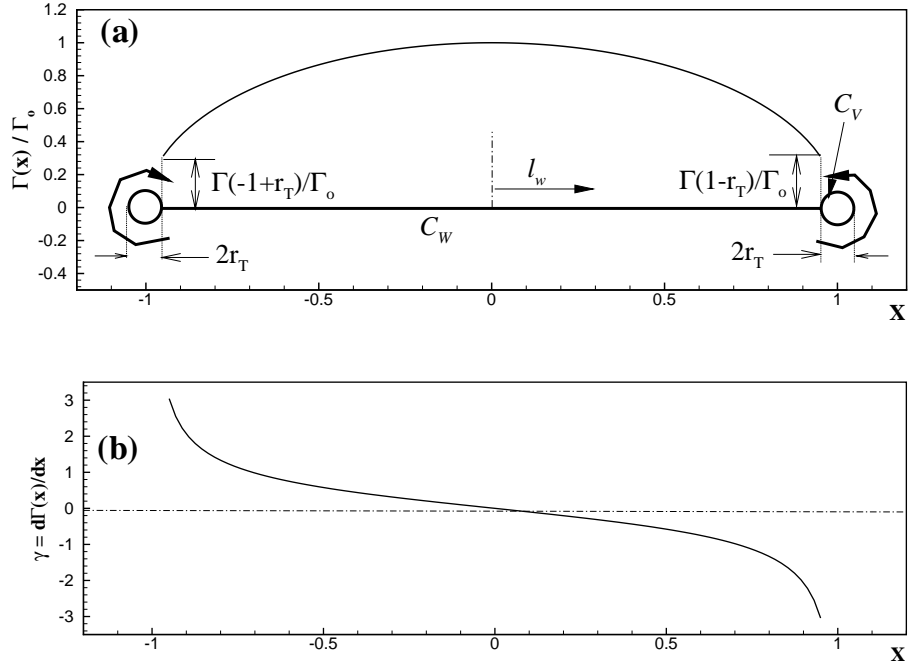
Figure 2.1: (a) Circulation Γ, and initial vortex sheet and tip vortex modeling, (b) Initial vortex sheet strength $\frac{\partial \Gamma}{\partial x}$.

2.3 The Elliptically Loaded Lifting Line Problem

2.3.1 Problem Definition

Consider an infinitely extended vortex sheet along the z-axis which intersects the xy planes, and is situated on $y = 0$ on the interval $-1 \leq x \leq 1$. The circulation is distributed elliptically along the span of the vortex line. A tip vortex of core radius r_T and non-zero circulation is modeled at the ends of the vortex sheet, as shown in Fig. 2.1.

$$\Gamma(\tilde{x}) = \Gamma_o \sin(\tilde{x}) \tag{2.1}$$

17

where $0 \leq \tilde{x} \leq \pi$, and $x = [1 - \cos(\tilde{x})]/2$.

2.3.2 Green's Formula

The fluid is assumed to be inviscid, incompressible and irrotational. This problem will be treated using the classical approach in the time domain [1] with time corresponding to the $z-$location of $z = U_\infty t$, where U_∞ is the inflow. Then, the fluid domain can be expressed in terms of potential, Φ, defined as follows :

$$\nabla \Phi(x, y, t) = \vec{q}(x, y, t) \tag{2.2}$$

where $\vec{q}$ is the velocity on the $xy-$plane. The total potential has to satisfy Laplace's equation inside the fluid domain.

$$\nabla^2 \Phi(x, y, t) = 0 \tag{2.3}$$

By applying Green's third identity to Eqn. 2.3, the integral equation for this vortex sheet problem can be expressed as follows:

$$\pi \Phi_p = \int_{C_V} \left[\Phi_q \frac{\partial \ln r}{\partial n} - \frac{\partial \Phi_q}{\partial n} \ln r \right] dl + \int_{C_w} (\Phi_w^+ - \Phi_w^-) \frac{\partial \ln r}{\partial n^+} dl \tag{2.4}$$

where C_V and C_w are the boundaries of the tip vortex core and free vortex sheet, respectively; r is the distance between the field point p and the variable point q; $\vec{n}^+$ is the unit normal vector on the vortex sheet pointing upward. Φ_w^+ and Φ_w^- are the dipole strength at the upper and lower side of the free vortex sheet related to the

---

[1]The 3-D approach, to be described next, could also be used, but we used the 2-D/time approach so that we could make comparisons with the results of other methods.

circulation distribution as follows :

$$\Phi_w^+(l_w) - \Phi_w^-(l_w) = \Delta\Phi_w(l_w) = \Gamma(l_w) \tag{2.5}$$

where l_w is defined along the arclength of the vortex sheet. Since the vortex sheet and tip vortex are freely moving in stationary flow domain, the kinematic boundary condition can be written as follows:

$$\frac{\partial\Phi}{\partial n} = 0 \tag{2.6}$$

Then, the integral Eqn. 2.4 can be simplified as follows:

$$\pi\Phi_p = \int_{C_V} \Phi_q \frac{\partial \ln r}{\partial n} dl + \int_{C_w} \Delta\Phi_w \frac{\partial \ln r}{\partial n^+} dl \tag{2.7}$$

Therefore, it is found that there is no need to distribute sources on the tip vortex. Only constant dipoles on the tip vortex and the vortex sheet are required for this problem. The shape of $C_V(l)$ will be that of a circle of radius r_T. In the present work, the shape will remain unchanged, even though the tip vortex core center is allowed to move freely [2].

2.3.3 Numerical Treatment

Once the boundary value problem is solved in terms of the unknown dipole strength on the tip vortex, then the velocity field induced by the tip vortex and the vortex sheet can be computed directly from differentiating the integral equation 2.7.

---

[2]In later sections, the shape of tip vortex core will be determined from applying the constant pressure condition on tip vortex surface.
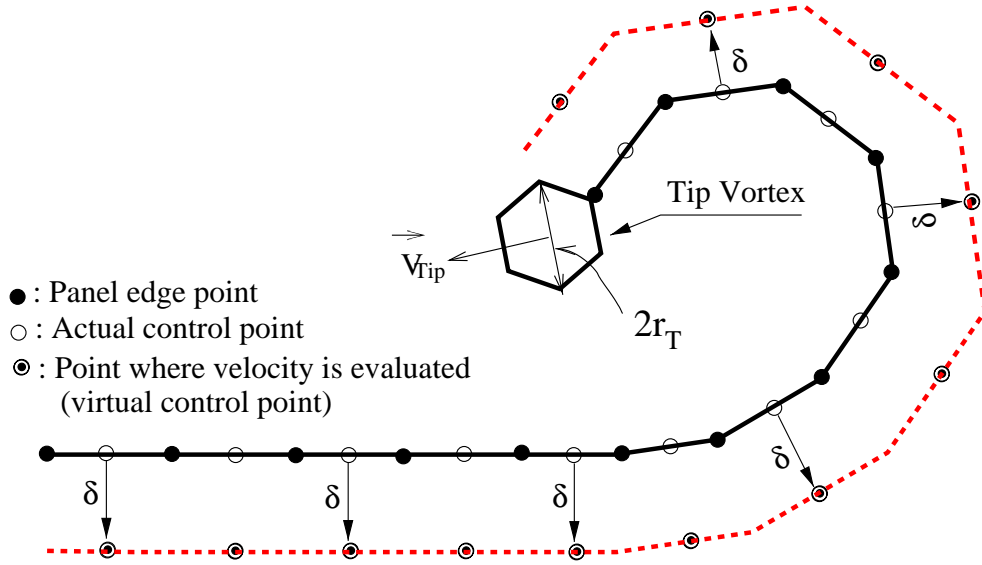
Figure 2.2: Definition of δ and points where the induced velocities are evaluated.

The induced velocity, $\vec{u}_{wi}$, on the vortex sheet is given as

$$2\pi\vec{u}_{wi} = \int_{C_V} \Phi_q \nabla \frac{\partial \ln r}{\partial n} dl + \int_{C_w} \Delta\Phi_w \nabla \frac{\partial \ln r}{\partial n} dl \qquad (2.8)$$

Since the integral equation 2.8 shows a numerical instability in the roll-up region of the vortex sheet, the induced velocity is computed at some slightly offset points (virtual control points), at local distance δ away from the control points, as shown in Fig. 2.2. This treatment of the roll-up region is similar to that of Krasny [1987].

The following numerical scheme is used to evaluate the new coordinates of free vortex sheet at time $t + \Delta t$.

1. The induced velocities are computed at the virtual control points, as shown in
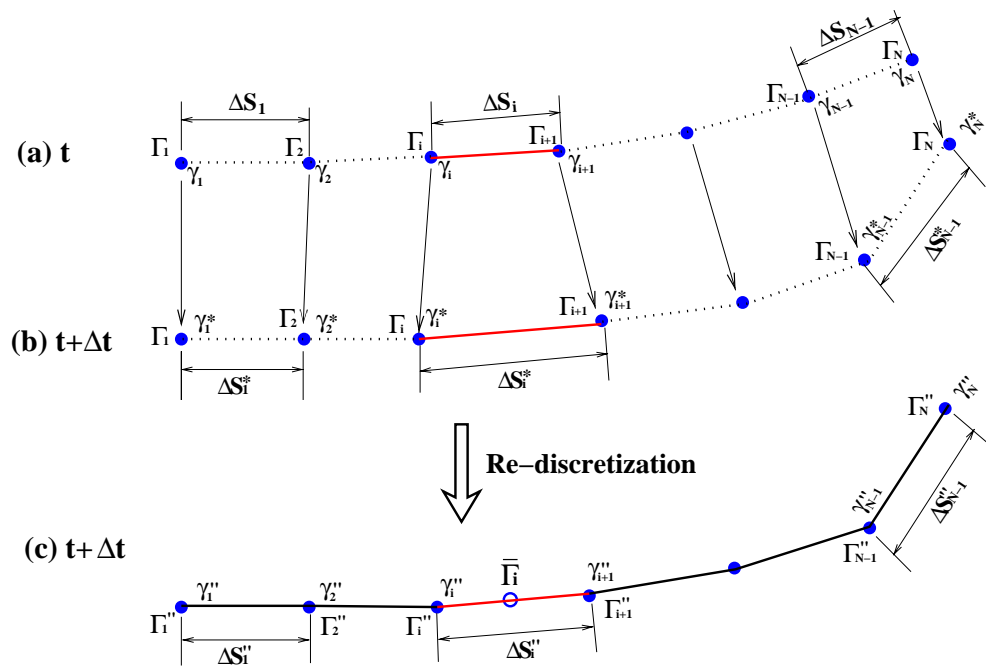
Figure 2.3: Re-discretization of vortex sheet and its strength (a) at time t, (b) at time $t + \Delta t$, and (c) the re-discretized geometry at time $t + \Delta t$

Fig. 2.2, along the vortex sheet for the given geometry and dipole strength at time t.

2. The velocity at the center of the tip vortex core, $\vec{V}_{Tip}$, is evaluated by taking the vector sum of the velocity vectors along the circumferential direction around the tip vortex core.

3. The new locations of the panel mid-points at time $t + \Delta t$ are computed using an Euler scheme.

$$\vec{X}_i(t + \Delta t) = \vec{X}_i(t) + \vec{u}_{wi}(t) \cdot \Delta t \tag{2.9}$$

where $\vec{X}_i(t) = (x_i(t), y_i(t), z_i(t))$.

4. The discretized coordinates of the panel nodal points are computed by using a cubic spline with respect to the arclength along the vortex sheet that passes through the computed control points and the center of tip vortex core.

5. The vorticity at the panel nodal point at time $t + \Delta t$ is computed by using Helmholtz's first vorticity theorem. As shown in Figs. 2.3-(a) and (b), the change in circulation between nodal points i and $i + 1$ on the vortex sheet at time t is

$$\Gamma_{i+1} - \Gamma_i = \int_{s_i}^{s_{i+1}} \gamma_s ds = \frac{\Delta s_i}{2}(\gamma_{i+1} + \gamma_i) \tag{2.10}$$

, and at time $t + \Delta t$

$$\Gamma_{i+1} - \Gamma_i = \int_{s_i^*}^{s_{i+1}^*} \gamma_s^* ds^* = \frac{\Delta s_i^*}{2}(\gamma_{i+1}^* + \gamma_i^*) \tag{2.11}$$

22

Then, the vorticity at each nodal point at $t + \Delta t$ is obtained by combining equations (2.10) and (2.11).

$$\gamma_{i+1}^* = \gamma_i^* + (\gamma_{i+1} + \gamma_i)\frac{\Delta s_i}{\Delta s_i^*} \tag{2.12}$$

where $\gamma_1 = \gamma_1^* = 0$ (due to symmetry).

6. With the cubic spline representation for $x(t + \Delta t)$ and $y(t + \Delta t)$, the vortex sheet is re-discretized to construct the new panel edge points. The spacing method for the re-discretization is the same as that of the initial geometry of vortex sheet. In other words, for constant spacing the total arclength is divided in the same number of equal length segments.

7. The vorticity (γ'') which corresponds to the re-discretized nodal point is computed from the cubic spline interpolation of γ^* over s^*. The circulation at each nodal point is evaluated by the trapezoidal rule integration of vorticity γ''.

$$\Gamma_{i+1}'' = \Gamma_i'' + \frac{\Delta s_i''}{2}(\gamma_{i+1}'' + \gamma_i'') \tag{2.13}$$

where $\Gamma_1'' = \Gamma_o$ Then, the potential at the panel center is evaluated by taking the mean value of the values at the edge points (Fig. 2.3-(c))

$$(\Delta\phi_w)_i = \frac{\Gamma_{i+1}'' + \Gamma_i''}{2} \tag{2.14}$$

8. The boundary value problem is solved for the new geometry and the above numerical scheme is repeated for the next time step.

23

2.3.4 Numerical Results

To validate the numerics of the present method, the convergence of vortex roll-up motions with number of panel is first investigated for fixed Δt, δ and tip vortex radius. Figure 2.4 shows the convergence of the present method with increasing number of vortex panels. The vortex roll-up was computed for $N = 50$, 100, 150 and 200 at $t = 0.5$, with values of $\Delta t = 0.01$, $\Gamma_o = 2.0$, $\delta = 10^{-4}$ and tip vortex radius $r_T = 0.001$. The results of two finest grids, $N = 150$ and 200, agree very well with each other. As the value of N increases, the predicted roll-up converges very quickly to that of the finest grid.

As mentioned in Krasny's work, the smoothing parameter, δ, damps the solution, as well as the short-wave instabilities. Thus, by decreasing the value of the smoothing parameter, the solution becomes unstable. As a result, the introduced short wavelength perturbation damages the solution accuracy. On the other hand, using a large smoothing parameter also introduces computational error, and under-produces the vortex roll-up motion by smoothing the solution too much. Since the present method introduced a similar parameter, δ, defined as the distance between the actual and the numerical control points, it is necessary to investigate the effect of δ. The effects of control point location defined as the parameter δ, are shown in Fig. 2.5. The large value of δ implies that the numerical control point is located away from the actual control point on the grid, and consequently δ damps the solutions and the short wavelength instabilities. As δ decreases, it forms more roll-up near the vortex tip. By using small enough value of δ, converged roll-up shapes are obtained in the cases of $\delta = 10^{-4}$ and $\delta = 10^{-5}$, as shown in Fig. 2.5.

24

The vortex structures with varying tip vortex radius are shown in Fig. 2.6. The total number of grids on the line vortex is $N = 100$, $\Delta t = 0.01$, and $\delta = 10^{-4}$. For decreasing radius of the tip vortex, more turns appear in the vortex core region, and the core region is tightly packed. In the case of $r_T = 0.0005$ and $r_T = 0.001$, the differences in the generated vortex spirals are negligible.

The variation of circulations on vortex line from $t = 0$ through $t = 1.0$ are shown in Fig. 2.7. As expected, the vorticity near the end of the vortex sheet becomes stronger with increasing time.

The computed vortex roll-up over the time interval $0 \leq t \leq 1.0$ for the elliptically loaded lifting line problem are shown in Figs. 2.8, and are compared with Krasny's result [Krasny 1987] which was predicted by using the vortex blob method. The vortex line rolls up smoothly, and forms complete rotating spiral at the tip of the vortex. The computed vortex sheet shows more complete turns than those of Krasny's results as time progresses. Since the present method used smaller δ compared with Krasny's, the formation of more spirals is expected in the result of the present method. In Fig. 2.8, it is shown that the tip vortex core moves slowly inward direction towards line of symmetry $x = 0$. For a short time, the tip vortex travels upward until the far-field effect of the other tip vortices becomes stronger, and finally, the entire vortex sheet moves downward.
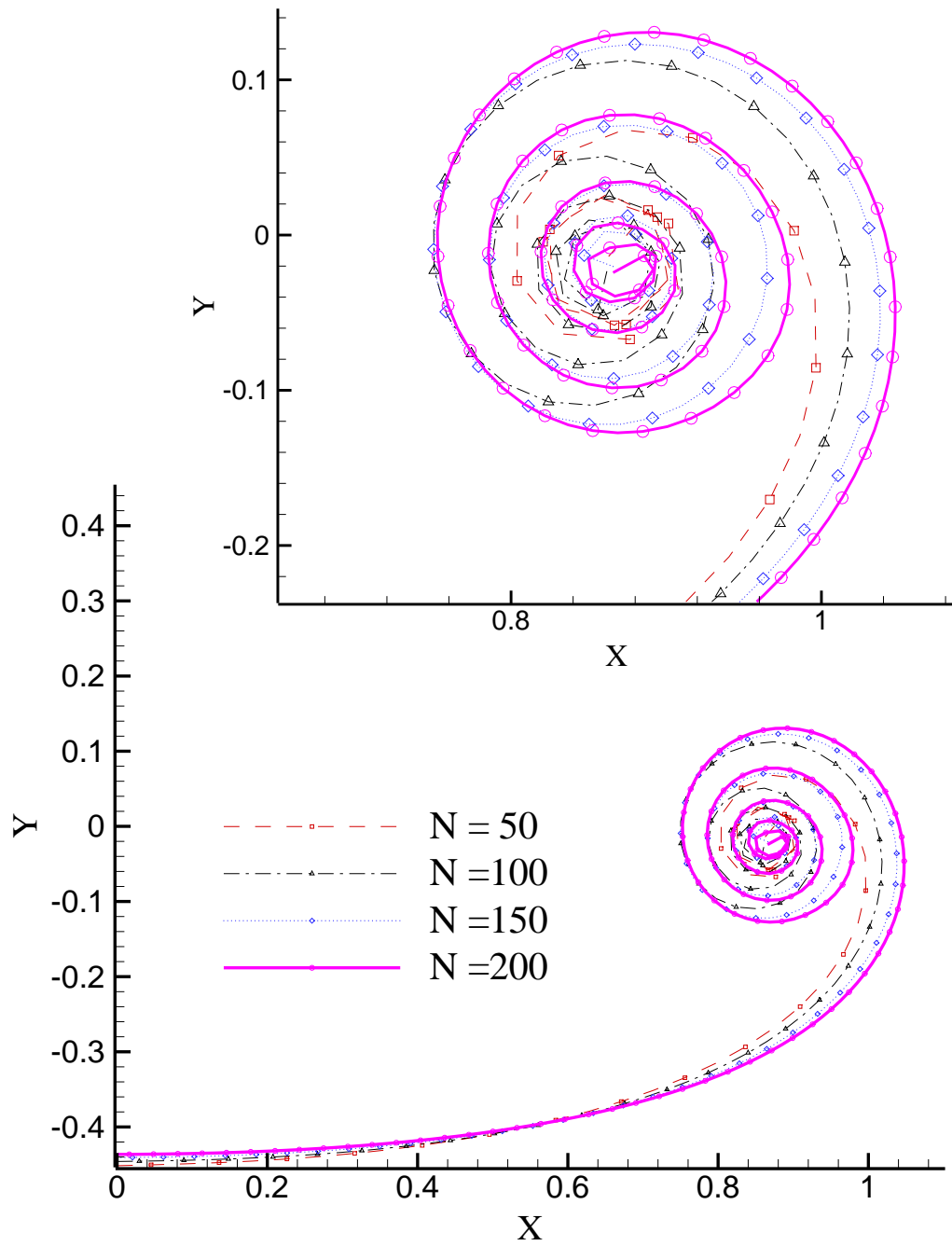
Figure 2.4: Convergence of the predicted vortex roll-up with number of grid at $t = 0.5 sec$: $\Delta t = 0.01$, $\Gamma_o = 2.0$, $\delta = 10^{-4}$, and $r_T = 0.001$.
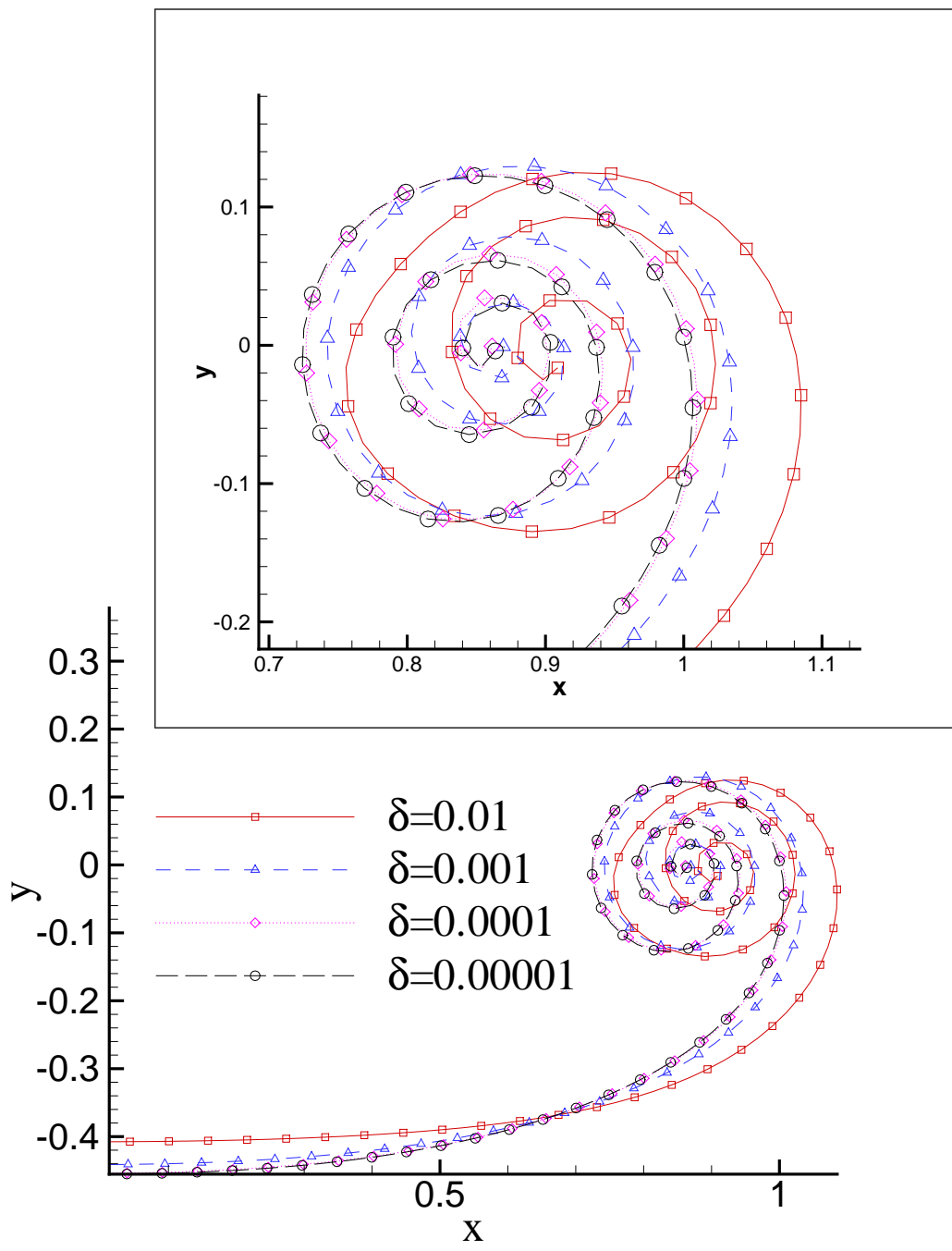
Figure 2.5: Convergence of the predicted vortex roll-up with δ at $t = 0.5$: $N = 100$, $\Delta t = 0.01$, $\Gamma_o = 2.0$, and $r_T = 0.001$.

27
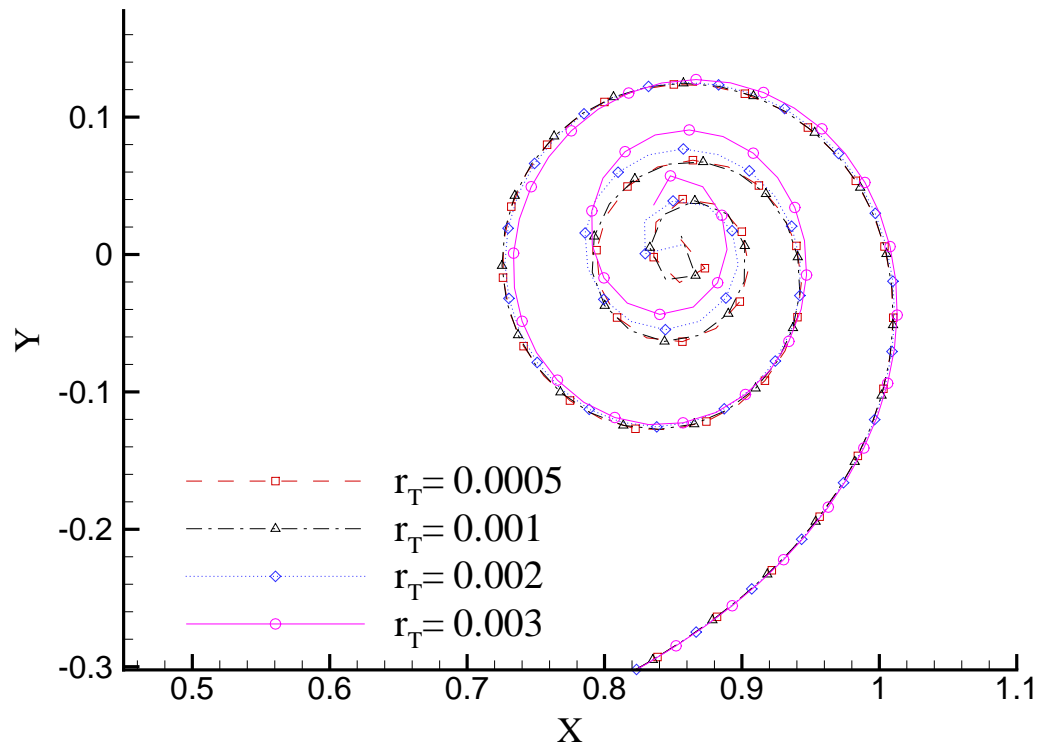
Figure 2.6: Dependence of the predicted vortex roll-up on the tip vortex radius, r_T, at $t = 0.5sec$: $N = 100$, $\Delta t = 0.01$, $\Gamma_o = 2.0$, and $\delta = 10^{-4}$.
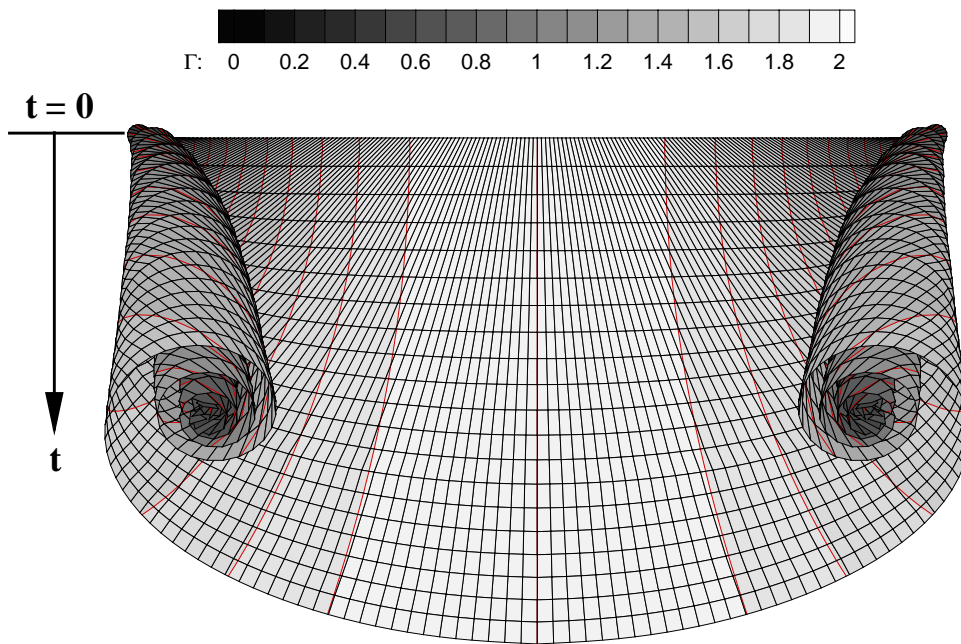
Figure 2.7: Variation of Circulation distribution on vortex line up to $t = 1.0\,sec$: $N = 100$, $\Delta t = 0.01$, $\Gamma_o = 2.0$, $\delta = 10^{-4}$, and $r_T = 0.001$.
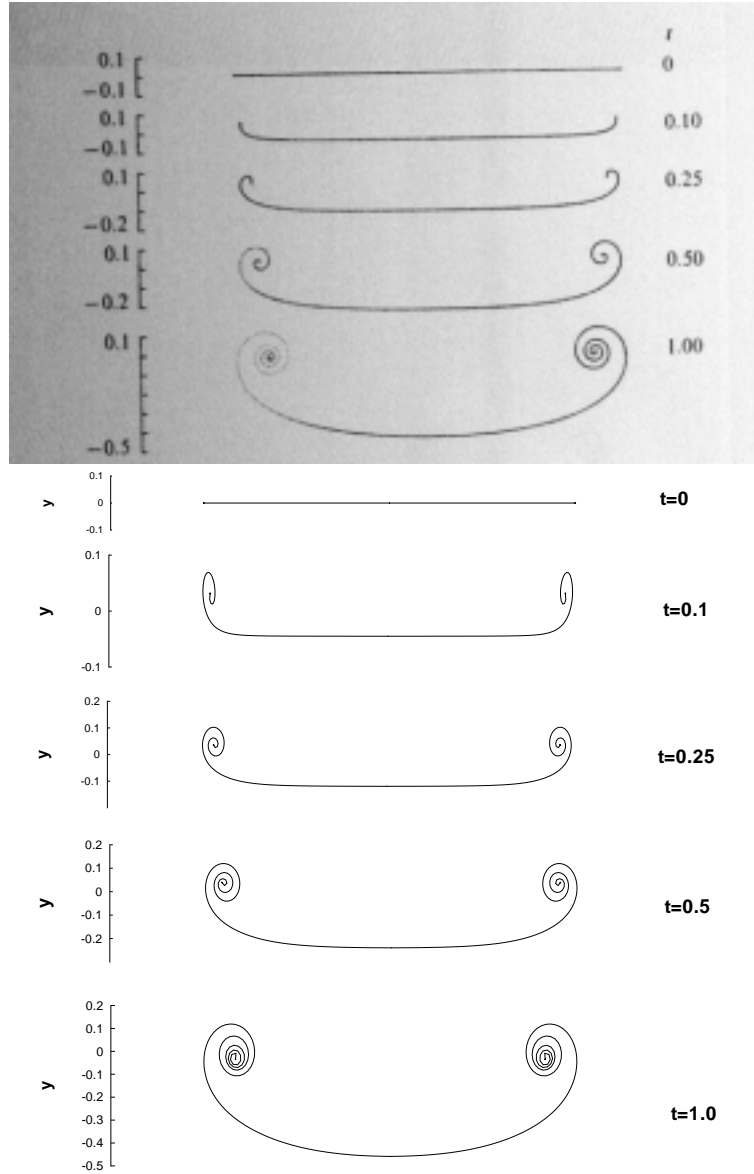
Figure 2.8: Comparison of time sequences of vortex roll-up ($0 \leq t \leq 1.0$): (a) Krasny's Results (Top), and (b) the present method (Bottom): $N = 100, \Delta t = 0.02$, $\delta = 0.0001$, $\Gamma_o = 1.0$ and tip vortex radius $r = 0.001$.

2.4   3-D Hydrofoil Problem

2.4.1   Formulation

A low order boundary element method is applied to align a trailing wake sheet behind a 3-D hydrofoil. Consider a 3-D hydrofoil which is subject to uniform inflow, U_∞, with angle of attack, α. The geometries of hydrofoil and its trailing wake, and the coordinates system are shown in Fig. 2.9. Since the shapes of the foil and the wake sheet are symmetric along xz plane, the boundary value problem is solved only over the half of the full geometry. The effect of the geometry for $y \leq 0$ is considered using a image method. The circular tip vortex is also introduced at the tip of the wake sheet, which, as in the 2-D case, is assumed to be a solid body.

The perturbation potential on the wetted hydrofoil and the tip vortex is given by the three dimensional Green's formula:

$$
\begin{aligned}
2\pi\phi_p &= \iint_{S_H \cup S_T} \left[\phi_q \frac{\partial G(p;q)}{\partial n_q} - \frac{\partial \phi_q}{\partial n_q} G(p;q) \right] dS \\
&+ \iint_{S_w} \Delta\phi_w(y_q) \frac{\partial G(p;q)}{\partial n_q} dS
\end{aligned}
\tag{2.15}
$$

where S_H, S_T and S_w represent hydrofoil, tip vortex and wake surface, respectively. Green function, $G(p;q)$, is defined as $1/R(p;q)$, and p and q are the field and variable points, respectively. $\vec{n}$ is a unit normal vector pointing into the fluid domain.

The perturbation potential on hydrofoil and tip vortex surfaces can be represented by a continuous source and dipole distribution on the foil and tip vortex surface, and a continuous dipole distribution on the trailing wake surface. The

31
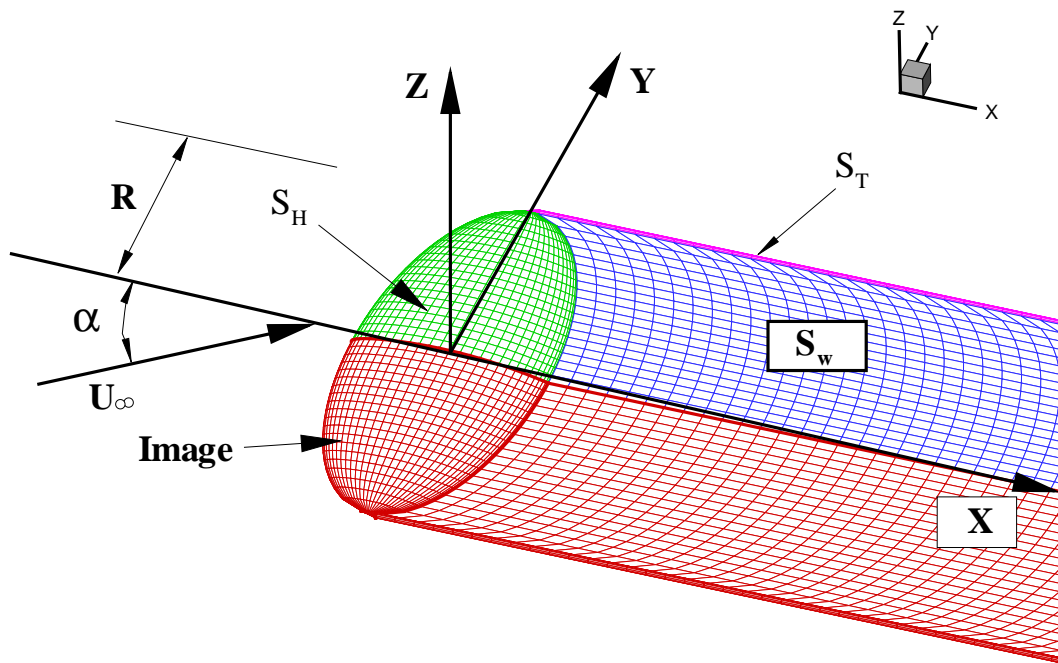
Figure 2.9: Three-dimensional hydrofoil, tip vortex, trailing wake and their images.

strength of a continuous source ($\frac{\partial \phi}{\partial n}$) on the hydrofoil and tip vortex surfaces can be determined from the kinematic boundary condition :

$$\frac{\partial \phi}{\partial n} = \vec{U}_\infty \cdot \vec{n} \tag{2.16}$$

The potential jump ($\Delta \phi_w$) on wake surface can be determined using the Kutta condition, which requires flow to be finite at the foil trailing edge [Morino and Kuo 1974].

$$\Delta \phi_w = \phi^+ - \phi^- \tag{2.17}$$

where ϕ^+ and ϕ^- are the values of the potential at the suction side and the pressure side of the foil trailing edge, respectively.

Once the boundary value problem is solved for the perturbation potential, the induced velocity on the wake surface can be evaluated by directly differentiating Eqn. 2.15.

$$\begin{aligned}
\vec{u}_{wi} &= \frac{1}{4\pi} \int\!\!\int_{S_H \cup S_T} \left[\phi_q \nabla \frac{\partial}{\partial n_q}(\frac{1}{R}) - \frac{\partial \phi_q}{\partial n_q} \nabla(\frac{1}{R}) \right] dS \\
&+ \frac{1}{4\pi} \int\!\!\int_{S_W} \Delta \phi_w(y_q) \nabla \frac{\partial}{\partial n_q}(\frac{1}{R}) dS
\end{aligned} \tag{2.18}$$

Then, the total velocity on the trailing wake surface is given by

$$\vec{V}_w(x, y, z) = \vec{U}_\infty(x, y, z) + \vec{u}_{wi}(x, y, z) \tag{2.19}$$

The streamline equation is applied to find the new location of the wake surface which is aligned with local total velocities.

$$\frac{V_w^x}{\Delta x} = \frac{V_w^y}{\Delta y} = \frac{V_w^z}{\Delta z} = \text{constant} = \frac{|\vec{V}_w|}{\Delta s} \tag{2.20}$$

33

where V_w^x denotes the x-component of the total velocity at the panel center, and Δx is the difference between the $x-$coordinates of two adjacent panel sides. Δs is defined as a distance between the centers of the two adjacent panel sides:

$$\Delta s = \sqrt{(x_{i+1} - x_i)^2 + (y_{i+1} - y_i)^2 + (z_{i+1} - z_i)^2} \qquad (2.21)$$

Then, the new coordinates at the $(n + 1)^{th}$ strip are determined as follows:

$$\begin{aligned}
x_{n+1} &= x_n + \frac{V_w^x}{|V_w|}\Delta s \\
y_{n+1} &= y_n + \frac{V_w^y}{|V_w|}\Delta s \\
z_{n+1} &= z_n + \frac{V_w^z}{|V_w|}\Delta s
\end{aligned} \qquad (2.22)$$

The procedure of solving the boundary value problem (by using Eqn. 2.15) and aligning the wake geometry (by using Eqn. 2.22) is repeated until the wake geometry is converged.

2.4.2 Numerical Results

- Elliptic hydrofoil

The 3-D wake alignment method is first applied in the case of a 3-D elliptic hydrofoil in steady flow to validate the numerical result of the trailing wake roll-up and contraction. The foil cross section shape is NACA $66_2 - 415$ and $a = 0.8$ mean camber line. The thickness to chord ratio, t_{max}/C, is 15%, the aspect ratio, and angle of attack are $AR = 3.0$ and 10°, respectively. In Fig. 2.10, the converged geometry of the wake sheet behind the elliptic wing is shown. The figure shows
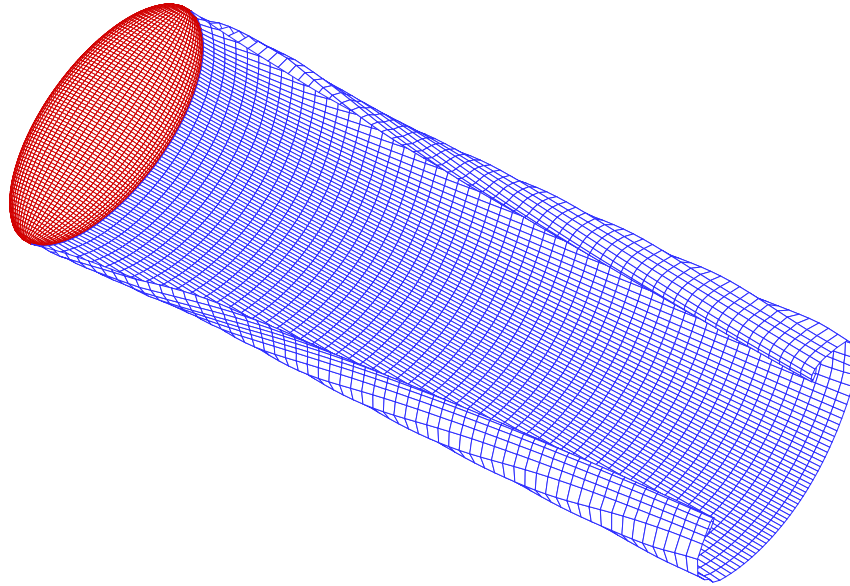
Figure 2.10: The converged wake geometry behind an elliptic wing: AR=3.0, t_{max}/C=0.15, and α=10°.

clear contraction and 3-D roll-up of the trailing wake. The convergence of the trailing wake geometries with number of panels is shown in Fig. 2.11. The wake sections at $x/R = 0.20$ and $x/R = 3.67$ are compared with varying spanwise number of panels (panels are distributed along the half span) for fixed chordwise panels (60 panels from trailing edge on the face to trailing edge on the back). As the number of panels along the spanwise direction increases, the sectional wake sheet geometry appears to converge to a limit of finest panels. Also, note that the wake ends obtained from different number of panels are located almost at the same point. Therefore, the trajectory of tip vortex core, which is important for the prediction of

the tip vortex cavity, can be predicted within reasonable accuracy by using a small number of panel.

Figures 2.12 and 2.13 show the convergence of the wake sectional shapes with number of iterations at the location $x/R = 2.0$ and $x/R = 4.5$. The convergence was tested for 60×40 panels. As shown in the figures, the wake geometry converges very quickly with increasing number of iterations.

The convergence of the circulation distribution with increasing number of panels is shown in Fig. 2.14. In addition, the circulation distribution corresponding to the initial straight wake geometry, in which the tip vortex model is not included, is depicted. Regardless of the number of panels, the circulation distributions agree well with each other. Note that the circulation of the aligned wake geometry with tip vortex model is finite at the foil tip, while the circulation of the initial wake geometry without the tip vortex model approaches "*zero*".

In figure 2.15, the tip vortex trajectory computed by the current method is compared with the trajectory of tip vortex cavity measured by [Arndt et al. 1991]. The thick line of the experimental result indicates the extent of variation of the trajectory for different physical parameters. Those experimental results range from $3.0^o \leq \alpha \leq 12.0^o$, $5.3 \times 10^5 \leq R_e \leq 10.4 \times 10^5$, and the cavitation number, σ, ranges from 0.26 to 3.19. According to Arndt's experiments, the tip vortex trajectory is almost independent of cavitation number. The tip vortex trajectory under non-cavitating conditions can be considered the same as that observed under cavitating conditions. The tip vortex cavity trajectory shown in Fig. 2.15 is currently computed under non-cavitating conditions, and shows good agreement with that

36
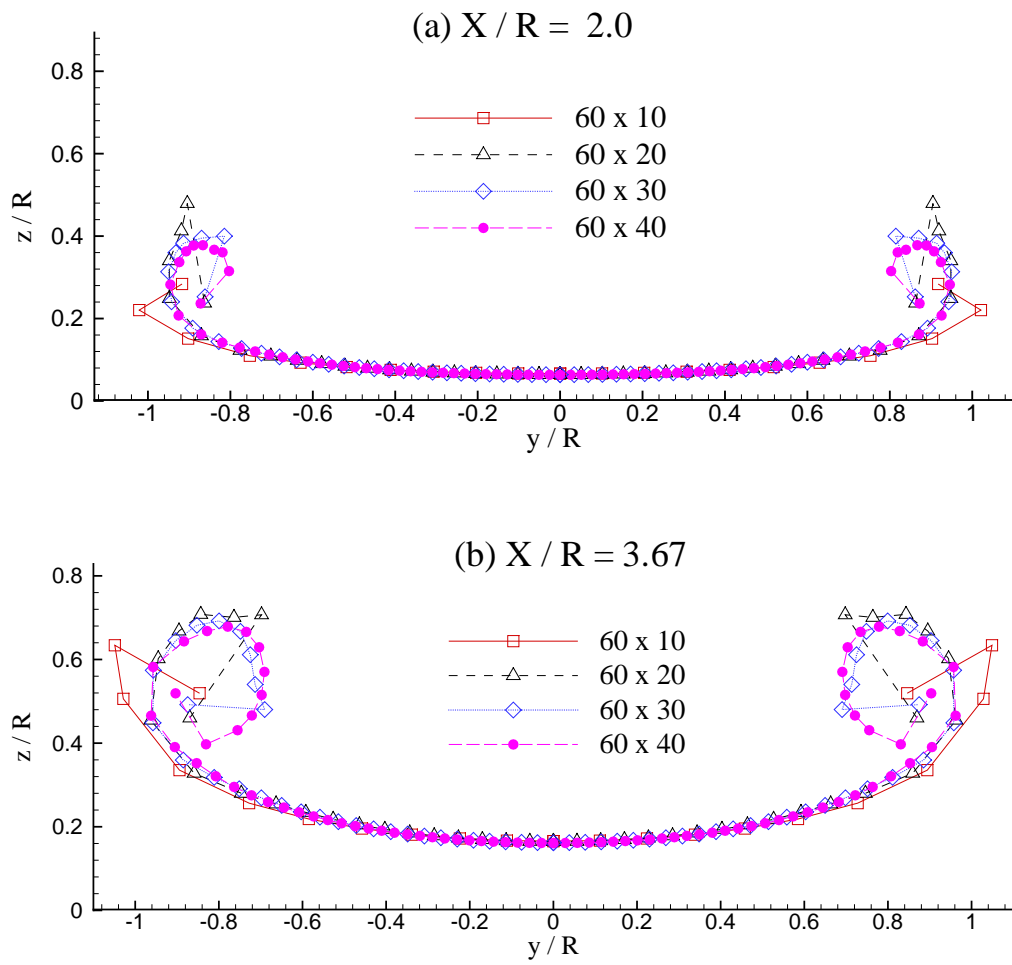
Figure 2.11: Convergence of wake sheet with number of panels at (a) x/R = 2.0, and (b) x/R = 3.67: AR=3.0, t_{max}/C=0.15, and α=10°.
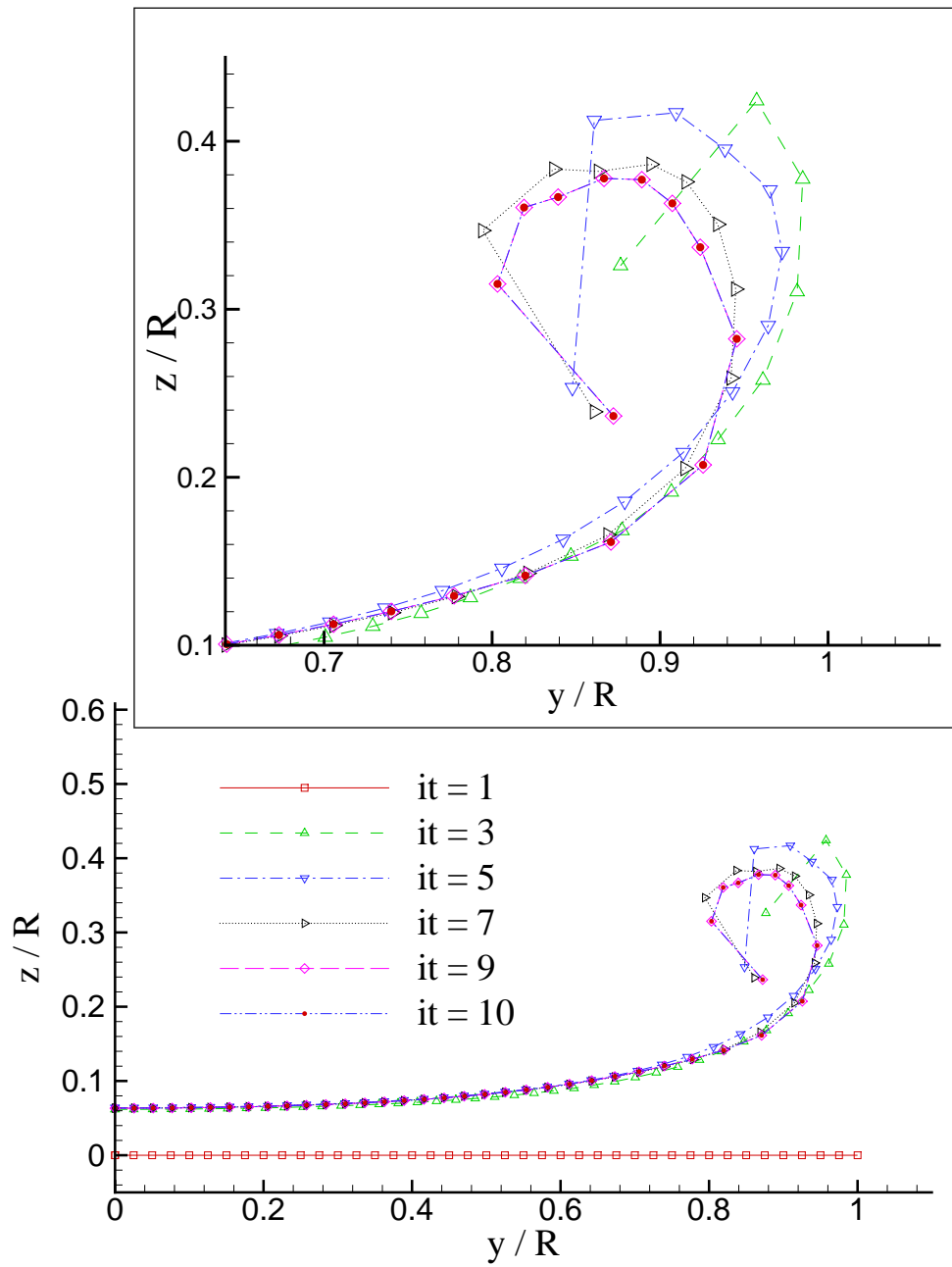
Figure 2.12: Convergence of wake sheets with number of iterations at x/R = 2.0. The total number of mesh on hydrofoil is 60 (chordwise) $\times$ 40 (half span): AR=3.0, $t_{max}/C = 0.15$, and α=10°.
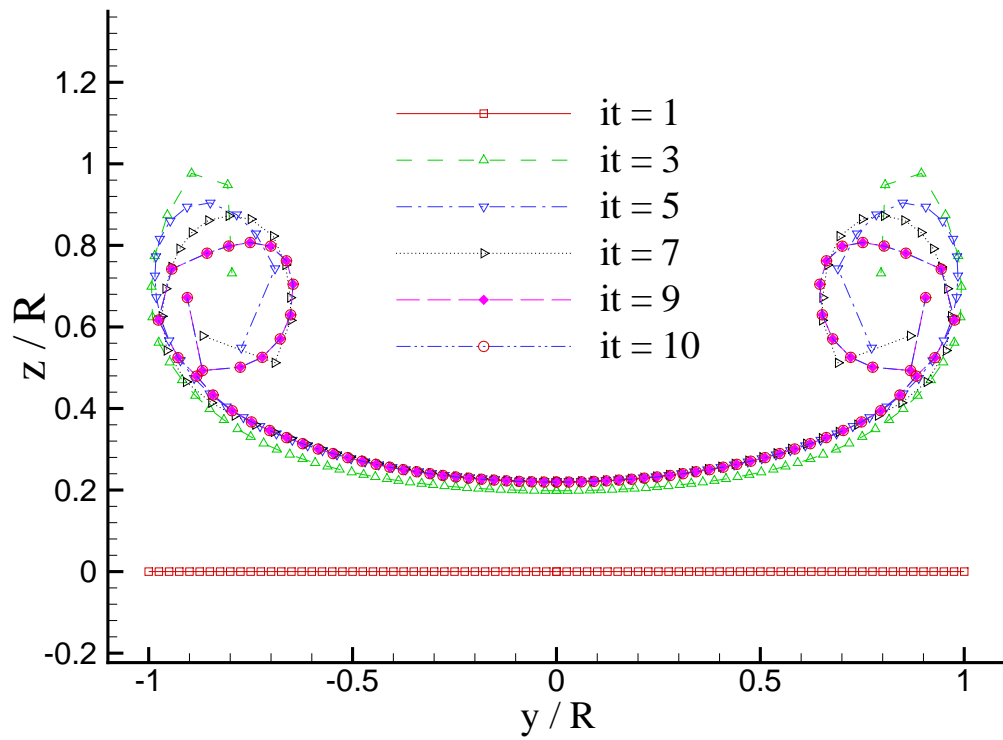
Figure 2.13: Convergence of wake sheets with number of iterations at x/R = 4.5. The total number of mesh on hydrofoil is 60 (chordwise) $\times$ 40 (half span): AR=3.0, $t_{max}/C = 0.15$, and α=10°
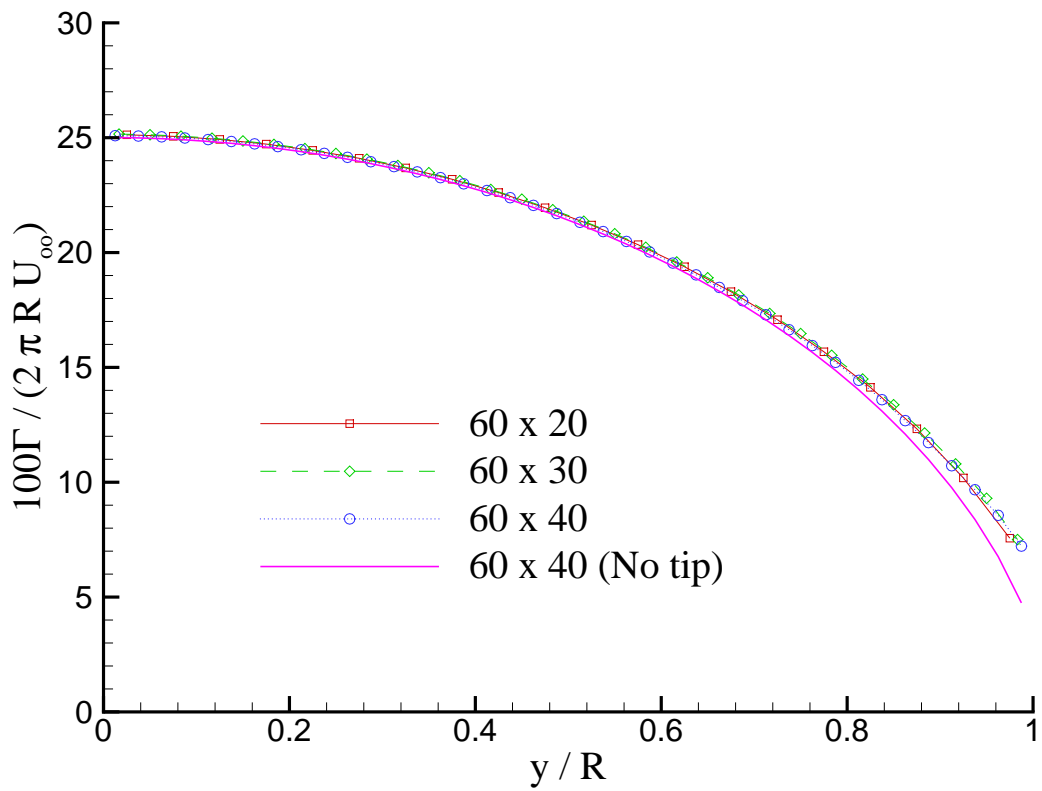
Figure 2.14: Convergence of circulation distribution with number of panels on hydrofoil with and without tip vortex core: AR=3.0, $t_{max}/C = 0.15$, and α=10°.
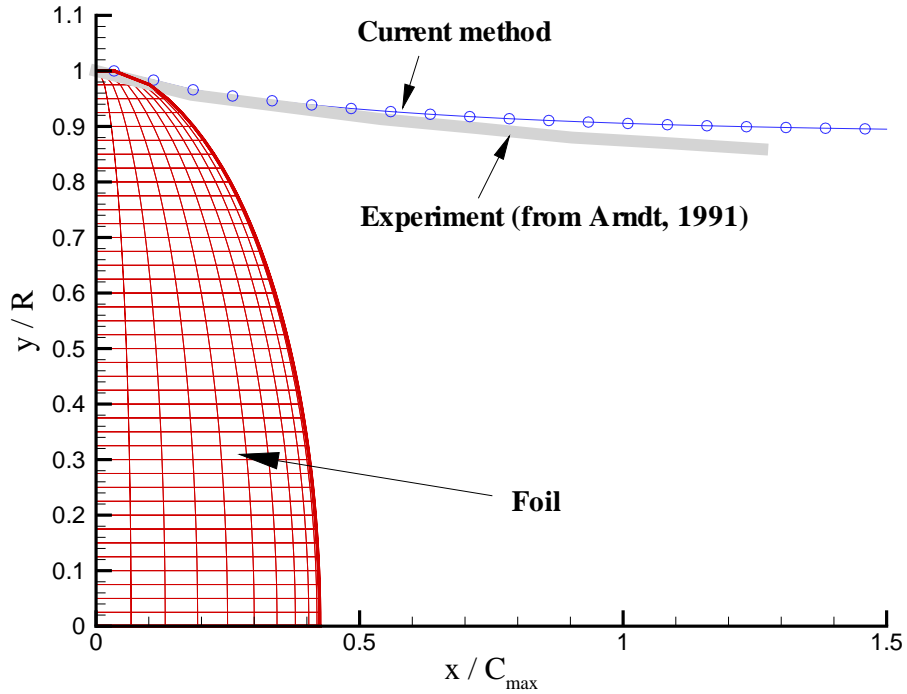
Figure 2.15: Comparison of the tip vortex cavity trajectory with that of experiment: AR=3.0, $t_{max}/C = 0.15$, and α=10°.

measured in the experiment.

- Rectangular hydrofoil

Next, a rectangular hydrofoil with $AR = 8$, $t_{max}/C = 0.01$ is considered to validate the method by comparing with other numerical methods. The foil is subject to uniform inflow with angle of attack, $\alpha = 10^o$. The rectangular hydrofoil, and the initial and the converged wake geometries are shown in Fig. 2.16. The converged wake geometry shows roll-up and contraction near the wake tip region.

(a) Initial geometry
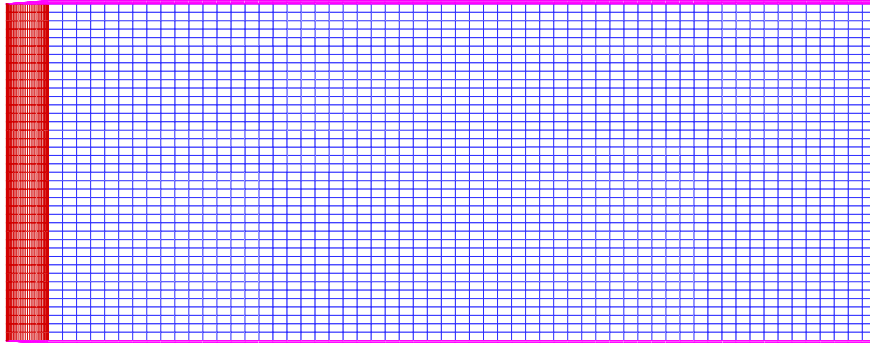
(b) Converged geometry
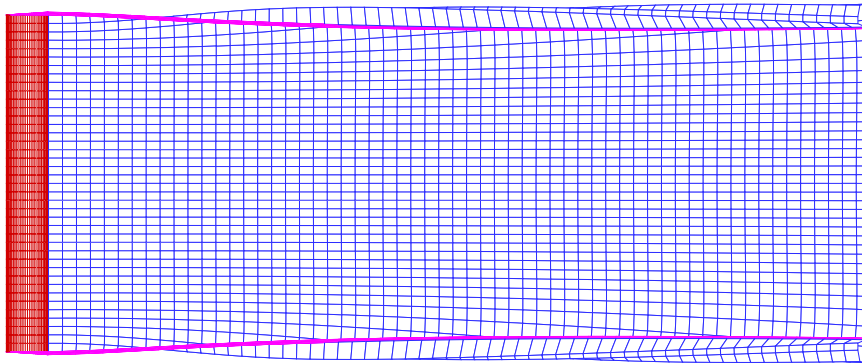
Figure 2.16: Rectangular hydrofoil, and (a) the initial wake and (b) the converged wake: t_{max}/C=0.01, AR=8.0, and 60×20 panels on hydrofoil.

The aligned wake cross sections predicted by the present method are compared with those obtained from other numerical methods which used a high order panel method. [Suciu and Morino 1977] predicted wake geometry using a geometric high order panel method, which used constant dipole distributions, and quadrilateral hyperboloidal panels on the foil and wake surfaces. On the other hand, [Pyo 1995; Pyo and Kinnas 1997] used a constant source and dipole distribution on the foil surface, and bi-quadratic strength dipole distribution on the wake surface. They also used quadrilateral hyperboloidal elements on the foil and wake surfaces. The wake cross section geometries are compared with those predicted by high order BEM at two different downstream locations, as shown in Fig. 2.17. The downstream locations where the wake geometries are computed, are at 4 and 9 times chord length downstream from the foil trailing edge. As expected, Pyo and Kinnas method produces more concentrated roll-up motion than the other methods, since his method uses cosine spacing to concentrate more panels near wake end and bi-quadratic dipole distribution for the velocity calculation. The wake cross section shapes near roll-up region predicted by all three methods show discrepancies in roll-up shapes and its sizes at both locations. However, the rest of the wake sheet geometries and the locations of the tip vortex cores predicted by present method compare well with those computed by high order methods.

The effect of inflow angle of attack on the wake cross section shapes are presented in Fig. 2.18. The predicted wake cross sections are compared with those computed by [Suciu and Morino 1977] for $\alpha = 5^o$, 10°, and 15°. The wake section shapes are computed at 9 times chord length downstream behind foil trailing edge.

43
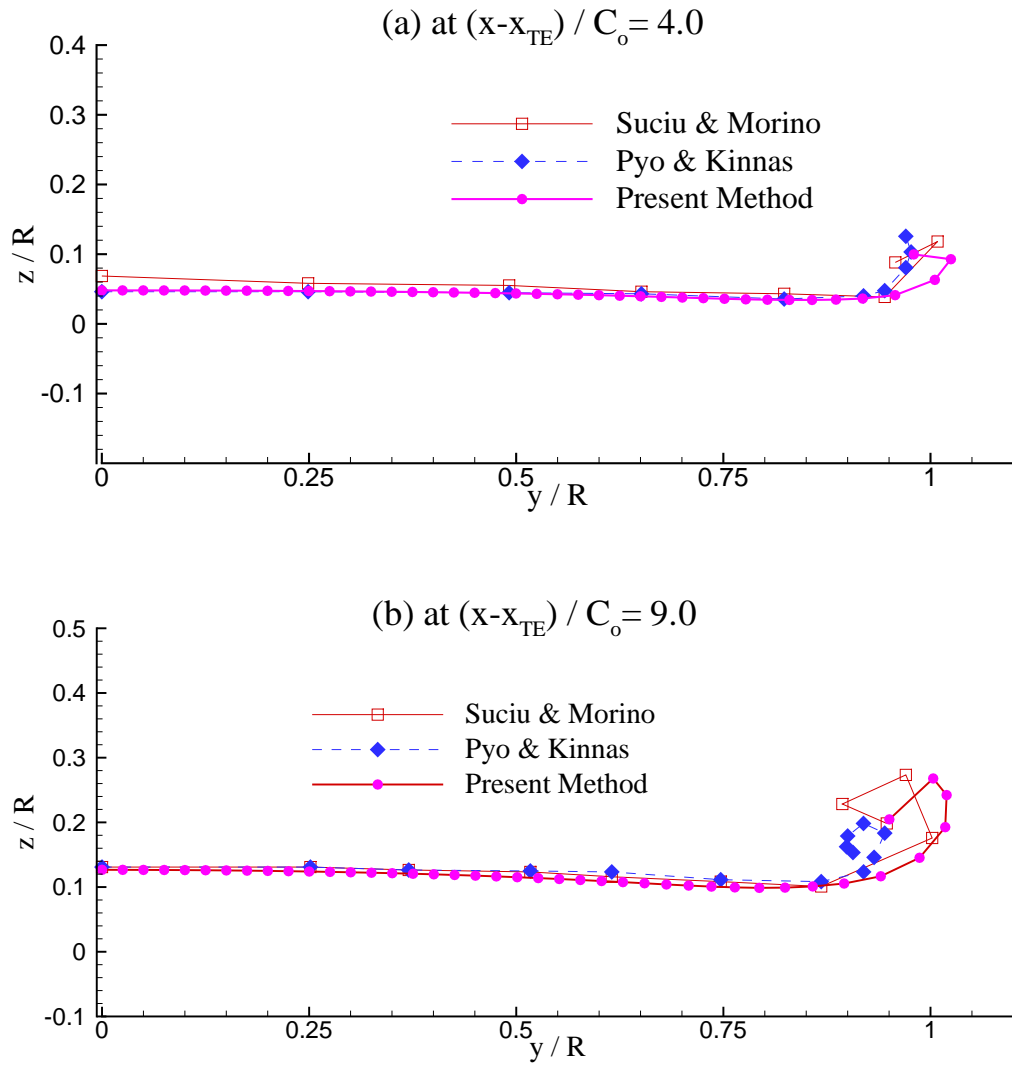
Figure 2.17: Comparison of the predicted wake cross section with those obtained from high order BEMs at (a) $(x - x_{TE})/C_o = 4$, and (b) $(x - x_{TE})/C_o = 9$: $t_{max}/C = 0.01$, AR=8.0, $\alpha = 10^o$, and 60×20 panels on hydrofoil.

Even though the result for $\alpha = 15^o$ is unrealistic, since flow may separate at this high inflow angle, the comparison is performed to investigate the stability of the present method. The predicted wake geometries at each angle show good agreement with those of [Suciu and Morino 1977] except at the near roll-up region. However, the same locations of the tip vortex core are predicted from both methods.
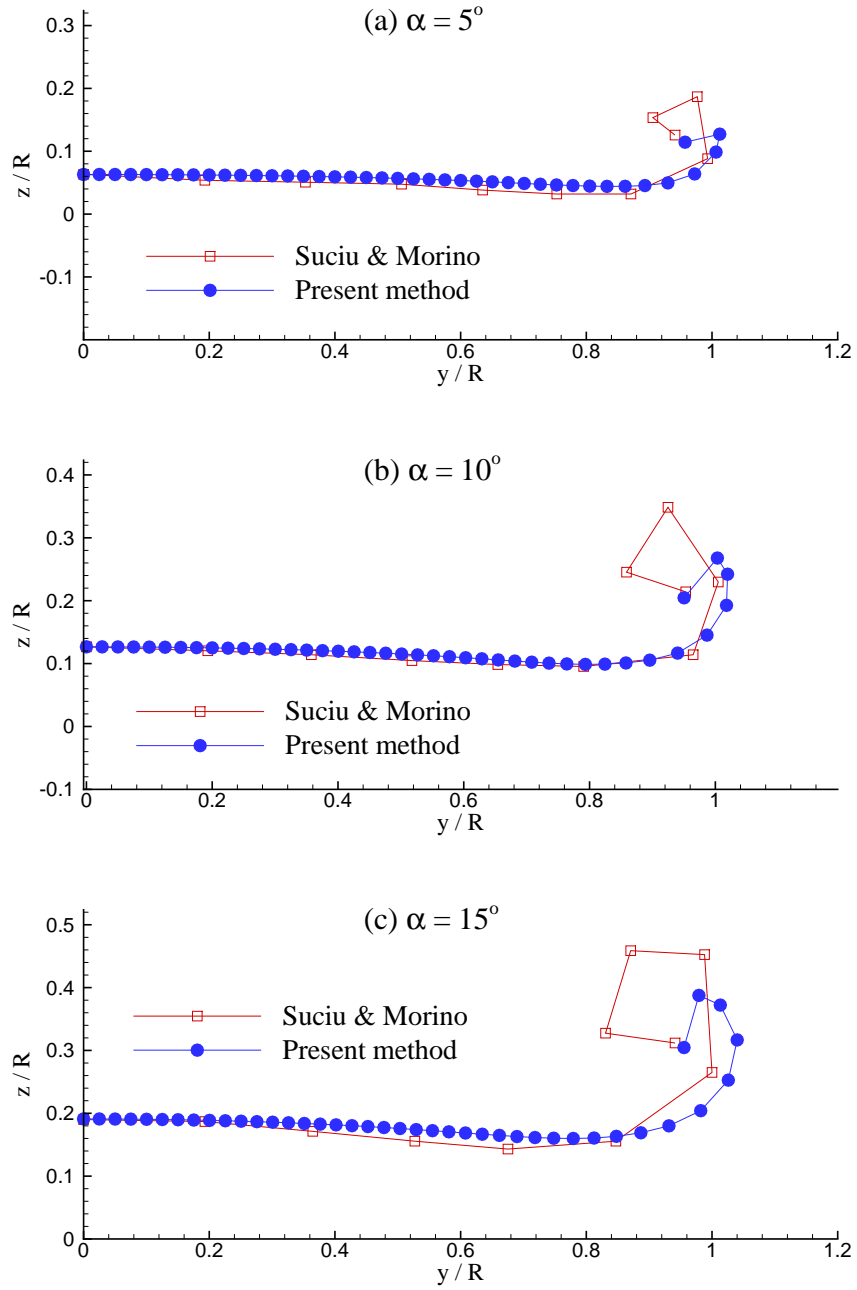
Figure 2.18: Comparison of the predicted wake cross sections with high order BEMs at $(x - x_{TE})/C_o = 9$ with varying inflow angles. (a) $\alpha = 5^o$ (b) $\alpha = 10^o$, and (c) $\alpha = 15^o$: $t_{max}/C = 0.01$, AR=8.0, and 60×40 panels on hydrofoil.

46

2.5 Propeller Problem

2.5.1 Definition

Consider a propeller subjected to a non-axisymmetric inflow $\vec{U}_w(x, r, \theta)$[3], which rotates at a constant angular velocity $\vec{\omega}$.

The modeled geometries of propeller blade, hub, bulb and tip vortex core, and trailing wake, and the coordinate systems are shown in Fig. 2.19. Notice that the conical bulb and the cylindrical tip vortex core are introduced at the blade and wake tip ends. The solution is determined in the (x, y, z) coordinate system, which is rotating with the propeller. Then, the total inflow velocity relative to the propeller is

$$\vec{U}_{in}(x, y, z, t) = \vec{U}_w(x, r, \theta - \omega t) + \vec{\omega} \times \vec{x}(x, y, z) \tag{2.23}$$

where $r = \sqrt{(y^2 + z^2)}$ and $\theta = \tan^{-1}(z/y)$.

2.5.2 Formulation

Based on potential flow assumptions (inviscid and irrotational), the potential ϕ_p at arbitrary point, p, on the body must satisfy the Green's third identity.

$$
\begin{aligned}
2\pi \phi_p(t) &= \iint_{S_B \cup S_T} \left[\phi_q(t) \frac{\partial}{\partial n_q(t)} \left(\frac{1}{R(p; q)} \right) - \frac{\partial \phi_q(t)}{\partial n_q(t)} \left(\frac{1}{R(p; q)} \right) \right] dS \\
&+ \iint_{S_w} \Delta \phi_w(r_q, \theta_q, t) \frac{\partial}{\partial n_q(t)} \left(\frac{1}{R(p; q)} \right) dS
\end{aligned}
\tag{2.24}
$$

where $R(p; q)$ is the distance between the field point p and the variable point q. $\vec{n}_q(t)$ is the unit normal vector to the surfaces of the propeller and the wake, and

---

[3]The inflow $\vec{U}_w(x, r, \theta)$ is assumed to be effective wake, *i.e.* it includes the interaction between the vorticity in the inflow and the propeller [Kinnas et al. 2000].
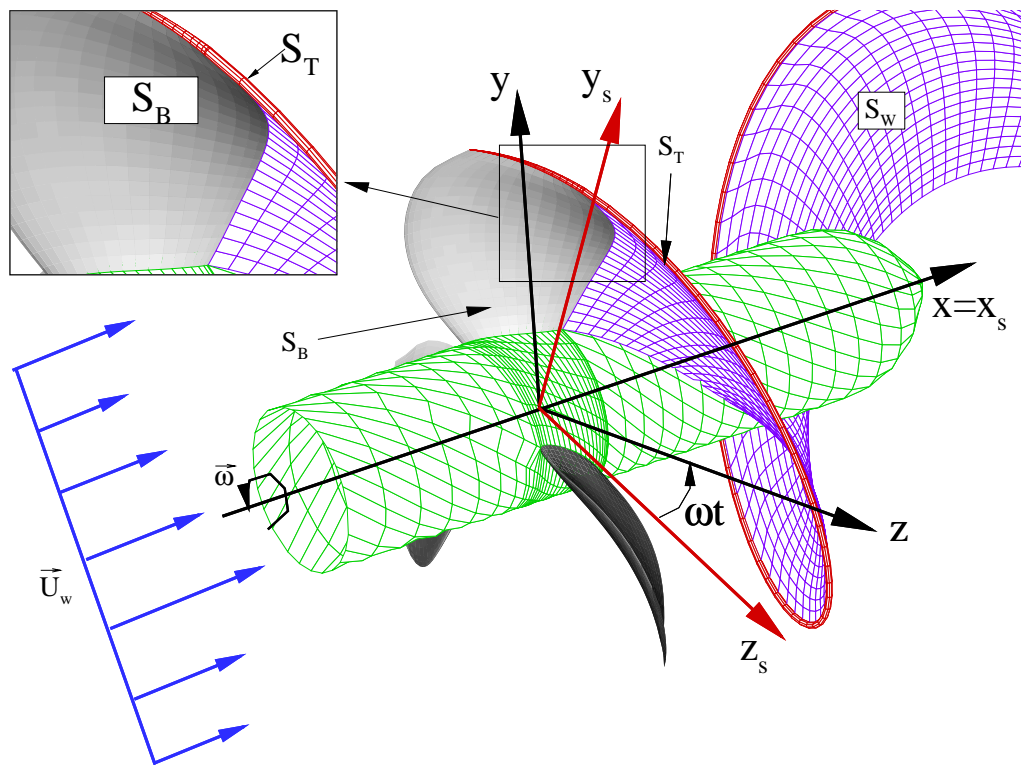
Figure 2.19: Propeller subjected to a general inflow. The propeller fixed (x, y, z) and ship fixed (x_s, y_s, z_s) coordinates are shown.

points into the fluid domain. $\Delta\phi_w$ is the potential jump across the wake surface S_w. Also, S_B and S_T denote fully wetted blade and hub, and tip vortex surfaces, respectively.

Equation (2.24) implies that the perturbation potential $\phi_p(t)$ at time t on the propeller surface can be expressed by distributing sources and dipoles over the blade and the hub, and only dipoles on the wake surface. The strength of the source distribution is known from the kinematic boundary condition on the body surface, which means that the flow should be tangent to the surface of blade, hub, and tip vortex.

$$\frac{\partial\phi}{\partial n} = -\vec{U}_{in} \cdot \vec{n} \tag{2.25}$$

2.5.3 Dipole Strength on Trailing Wake

The dipole strength of the trailing wake can be implicitly determined as a part of the solution for integral equation (Eqn. 2.24) by applying the Kutta condition, which requires the velocity to be finite at the trailing edge of the blade [Morino and Kuo 1974].

$$\Delta\phi_w = \phi^+ - \phi^- \tag{2.26}$$

where ϕ^+ and ϕ^- are the values of the potential at the suction side and the pressure side of the blade trailing edge, respectively.

In steady state ($t < 0$), the trailing wake strength is assumed to be invariant along the trailing wake sheet, as

$$\nabla\phi_w^s(r) = \phi^+(r, t < 0) - \phi^-(r, t < 0) \tag{2.27}$$

49

As shown in equation (2.27), the steady state is considered as $t < 0$, and the propeller is subject to the circumferentially averaged mean inflow.

In the unsteady state, however, the dipole strength, $\Delta\phi$, in the wake is convected along the assumed wake surface with angular speed ω in order to ensure that the pressure jump in the wake is equal to zero [Kinnas and Hsin 1992], i.e.,

$$
\begin{aligned}
\Delta\phi_w(r, \phi, t) &= \Delta\phi_w\left(r, t - \frac{\theta - \theta_T(r)}{\omega}\right); t \geq \frac{\theta - \theta_T(r)}{\omega} \\
\Delta\phi_w(r, \phi, t) &= \Delta\phi_w^s(r); t < \frac{\theta - \theta_T(r)}{\omega}
\end{aligned}
\tag{2.28}
$$

where r and θ are the cylindrical coordinates of the wake surface, and θ_T is the θ coordinate of the blade trailing edge at radius r. $\Delta\phi_w^s(r)$ is the steady flow potential jump in the wake when the propeller is subject to the circumferentially averaged inflow.

Since the dipole and source strengths on the blade and hub panels, and the dipole strengths on the wake panels are already known from the previous solution, the induced velocity on the trailing wake panels can be computed by using the Green's formula. Note that the dipole strengths on the wake surface along each strip are constant in steady flow, but those strengths are convected downstream with time in unsteady flow.

The induced velocity on the wake surface is given by

$$
\begin{aligned}
\vec{u}_{wi}(t) &= \frac{1}{4\pi}\int\int_{S_B(t)\cup S_T(t)}\left[\phi_q(t)\nabla\frac{\partial G(p;q)}{\partial n_q(t)} - \frac{\partial\phi_q(t)}{\partial n_q(t)}\nabla G(p;q)\right]dS \\
&+ \frac{1}{4\pi}\int\int_{S_W(t)}\Delta\phi_w(r_q, \theta_q, t)\nabla\frac{\partial G(p;q)}{\partial n_q(t)}dS
\end{aligned}
\tag{2.29}
$$

50

where $G(p; q) = 1/R(p; q)$ is the infinite domain Green's function.

The total velocity on the wake surface is determined by adding the total in-
flow velocities, $\vec{U}_{in}(x, y, z, t)$, and the induced velocities, $\vec{u}_{wi}(x, y, z, t)$, computed
from equation (2.29).

$$\vec{V}_w(x, y, z, t) = \vec{U}_{in}(x, y, z, t) + \vec{u}_{wi}(x, y, z, t) \tag{2.30}$$

2.5.4 Unsteady Wake Alignment

The following numerical method is implemented to compute the aligned
wake geometry which satisfies the force-free condition on the wake surface.

- *steady mode ($t < 0$)*

  1. Solve the steady Boundary Value Problem (BVP) with purely helical
     wake without any modeling of the contraction and the roll-up at the
     blade tip.

  2. Calculate the induced velocities on wake surface by directly applying
     Eqn. 2.29 at the displaced control points. The dipole strengths on the
     blade and the assumed tip vortex core surfaces are known from the BVP
     solution.

  3. Compute the mean velocity, $(\vec{V}_{Tip})$, at the center of the tip vortex core,
     and interpolate the total velocities at the panel edges to the control points
     on the wake surface.

  4. Find the new wake coordinates by aligning with the total local veloci-
     ties. The time step size, δt, of the shed vorticity is determined from the

51

angular increment of the discretized wake sheet.

$$\delta t = \frac{\delta\theta}{\omega} = \frac{\delta\theta}{2\pi n} \qquad (2.31)$$

where ω is the propeller rotational speed (radian per unit time). The new coordinates at $(n+1)^{th}$ strip are determined by the following equation.

$$
\begin{aligned}
x_{n+1} &= x_n + V_w^x \delta t \\
y_{n+1} &= y_n + V_w^y \delta t \qquad (2.32) \\
z_{n+1} &= z_n + V_w^z \delta t
\end{aligned}
$$

5. Solve the BVP again with the updated wake geometry, and align the wake geometry until the difference of the wake geometries between two consecutive iterations is within a given criterion.

6. Save the wake geometry, and dipole strengths on blade ($\phi(x, y, z, t < 0)$), and wake panels ($\Delta\phi(x, y, z, t < 0)$) for the unsteady wake alignment process. These steady results are the initial values for the unsteady problem, which is described below.

- *unsteady aligning mode ($t \geq 0$)*

  1. Set the initial wake geometries of key and other blades, which are assumed to be the same as those aligned in the steady mode.

  2. Solve the unsteady BVP for the potentials on key blade and tip vortex core with updated wake geometries. In unsteady analysis, the BVP is solved only for the potential of key blade and the tip vortex cavity. The

influence of the other blades on the key blade is accounted for in a progressive manner by using the solution from the previous time step where the key blade was in the position of that blade.

3. Compute the induced velocities at the control point on the key blade wake.

4. Update the key blade wake geometry by using the same method which is explained in (4) of steady mode.

5. Solve the BVP again with the aligned wake of key blade, and determine the dipole strengths of key blade and its wake panels.

6. Save $\phi(t)$, $\Delta\phi(t)$, and the aligned key wake geometry.

7. Move to the next time step $(t+1)$. Update the wake geometries, $\phi(t+1)$, and $\Delta\phi(t+1)$ of the other blades from the previously saved data.

8. Repeat unsteady mode steps from (2) to (7) until the key wake geometry is converged.

- *fully unsteady mode:* this mode does not perform wake alignment, but uses the aligned wake as predicted in the previous mode.

  1. Update wake geometries of key and other blades corresponding to the time step t from the results of unsteady aligning mode run.

  2. Update the $\phi(t)$, and $\Delta\phi(t)$ of other blades and wakes at the corresponding time step.

3. Repeat solving BVP by updating $\phi(t)$, and $\Delta\phi(t)$ until the last revolution.

In order to obtain the converged wake geometry and the forces, the unsteady aligned mode is repeated up to 2 revolutions, and the fully unsteady mode is solved at least up to 4 revolutions.

2.5.5 Numerical Results

The current wake alignment method is applied to determine the trailing wake sheets of marine propellers, in which the wake sheet is determined in fully unsteady manner.

DTMB N4119 propeller

DTMB N4119 propeller is a simple three bladed propeller. The blade has no skew, and the blade section has a NACA 66 modified thickness form and a=0.8 mean camber line distribution. Since inflow is considered to be uniform, the wake is aligned only in steady wetted state, and the design advance ratio, J_s, is equal to 0.833.

Initially, the trailing wake sheet is assumed to be a spiral helix which sheds from the blade trailing edge with the given pitch angles at each radius of propeller blade. The hub effect is not included in this calculation. The aligned trailing wake sheet is given in Fig. 2.20, which shows roll-up and contraction of the vortex core as it sheds downstream from blade trailing edge. Since the flow is uniform, the wake geometries of the three blades are identical and equal to those of steady results.
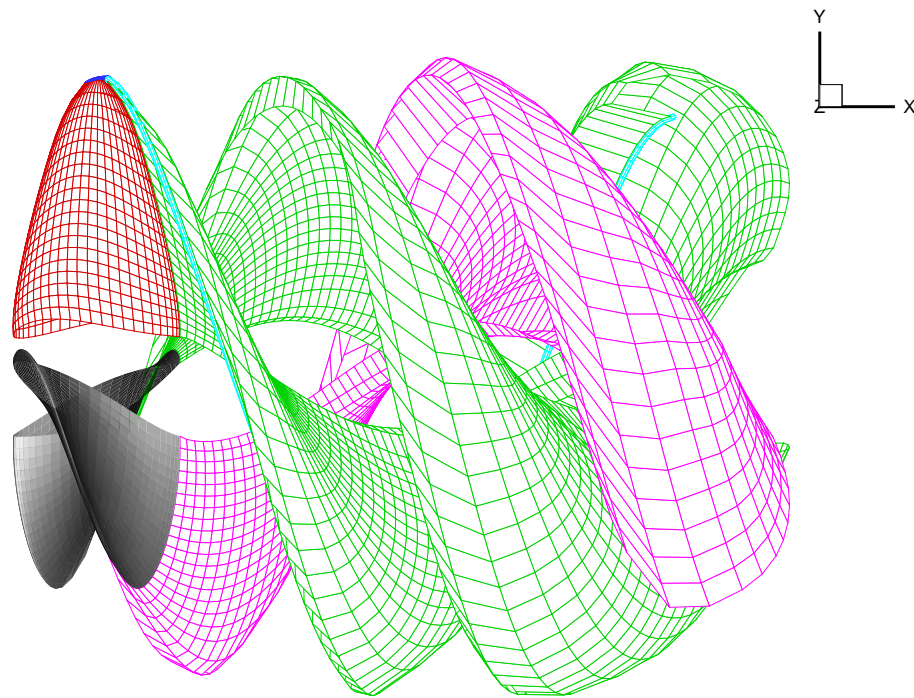
Figure 2.20: The aligned wake geometry of DTMB N4119 propeller at $J_s = 0.833$.

In Fig. 2.21, the comparison of the predicted tip vortex trajectory with those measured and computed using other numerical method is shown. The tip vortex trajectory marked as a high order BEM has been computed by [Pyo 1995; Pyo and Kinnas 1997] using FLAG (FLow Adapted Grid) method. The predicted trajectory compared well with that measured in the experiment [Jessup 1989], and with that predicted by the high order BEM.
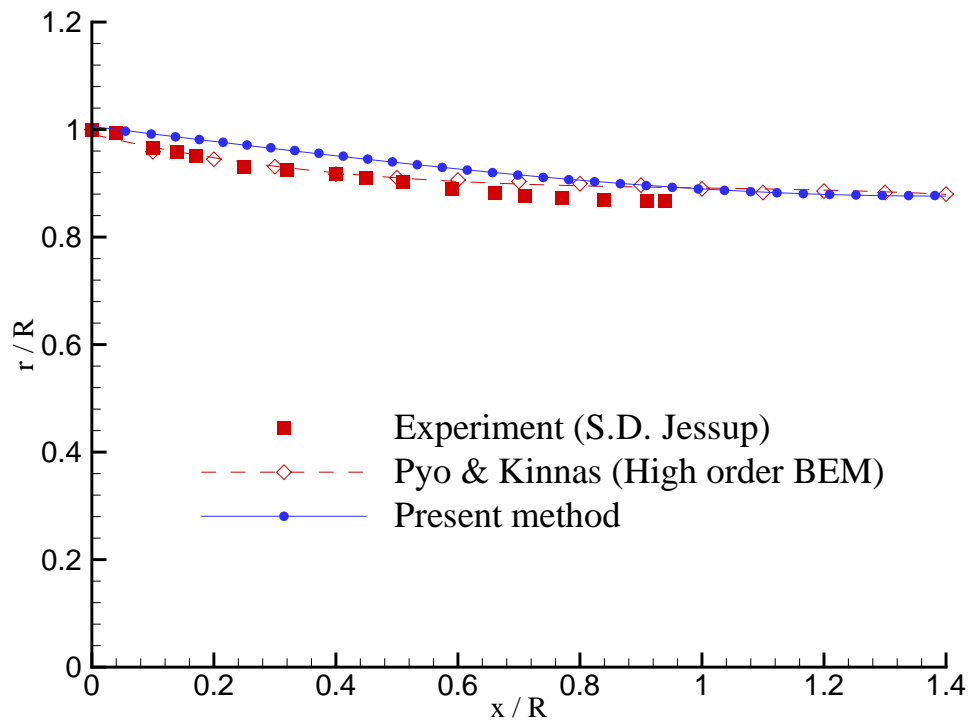
Figure 2.21: Comparison of tip vortex core trajectories with experiment and high order method for DTMB N4119 propeller at $J_s = 0.833$.

DTMB N4661 propeller

The wake alignment algorithm is applied to generate the unsteady wake geometries of DTMB N4661 propeller. DTMB N4661 is a five bladed propeller with a high skew distribution. [Boswell et al. 1984] performed experiments used DTMB N4661 propeller to analyze the propeller forces and moments under inclined inflow conditions. Also, [Kinnas and Pyo 1999] numerically investigated the effects of inflow inclinations by using the vortex lattice method, in which the trailing wake sheet was inclined by the inflow angle.

To investigate the performance of the numerical scheme in the case of un-steady wake alignment, an inclination angle $\alpha = 10^o$ is considered. The axial velocity component for this case is equal to $\cos 10^o$ at the zero-th harmonic, the first cosine harmonic of the radial velocity component is equal to $\sin 10^o$, and the first sine harmonic of the tangential velocity component is equal to $-\sin 10^o$. The numerical calculation is performed at $J_s = 1.0$ and $F_n = 4.0$.

The aligned wake geometries at several angles of the key blade position are shown in Fig. 2.22. At each angular position, the trailing wake moves upward due to the inclined inflow and rolls up near the tip region. The projected views of the aligned wakes are shown in Fig. 2.23, which clearly demonstrate the inclination of the wake sheet. It is interesting to note that the calculated wake inclination angle $(= 6.7^o)$ is different from that of the inflow inclination angle $(= 10^o)$

The convergence of the unsteady thrust and torque with number of iterations (or revolutions) is shown in Fig. 2.24. In this method, the problem is solved only
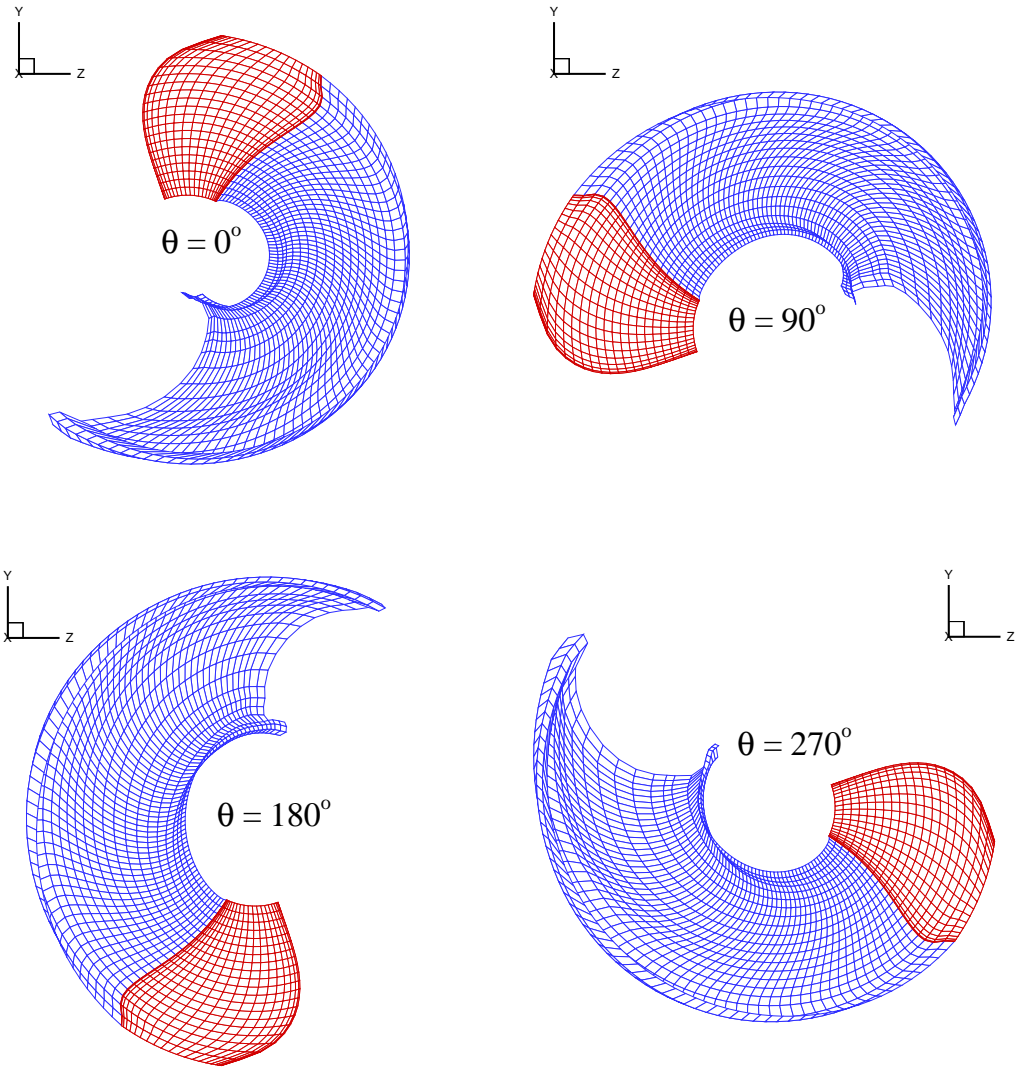
Figure 2.22: The key blade and aligned wake geometries for DTMB N4661 propeller: $J_s = 1.0$, $F_n = 4$ and $\alpha = 10^o$.
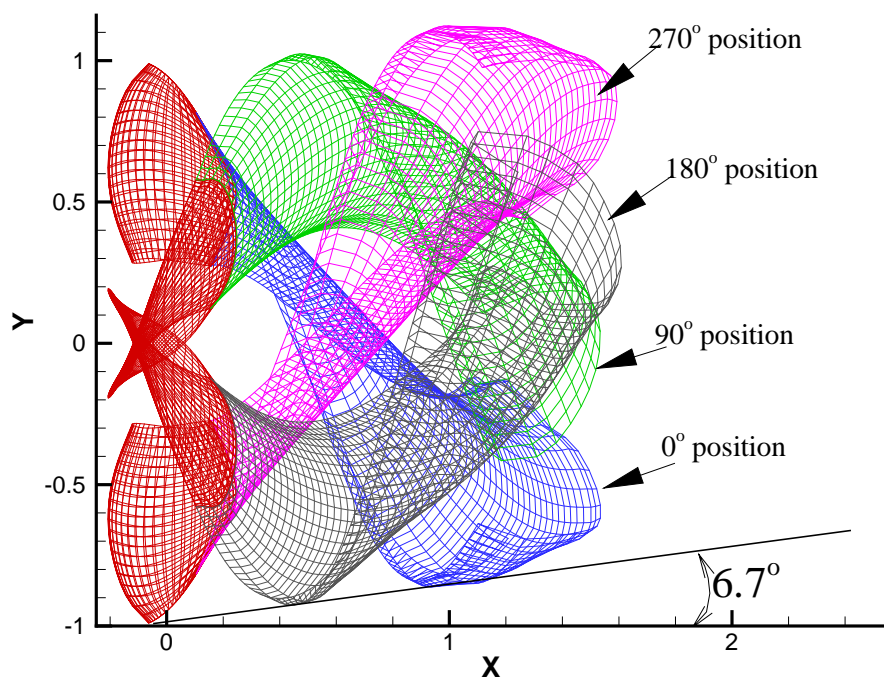
Figure 2.23: The projected view of aligned wake geometries for DTMB N4661 propeller: $J_s = 1.0$, $F_n = 4$ and $\alpha = 10^o$.

for the key blade (or main blade), and the effects of the other blades on the key blade are considered in a progressive manner. Therefore, the BVP is solved for several revolutions until the converged unsteady forces are achieved. The steady forces which are computed for the circumferentially averaged mean inflow are also shown. In other words, the steady result includes the effect of the axial component of the inflow, but the radial and the tangential components are excluded. The thrust and torque coefficients are defined as follows:

$$
\begin{aligned}
\text{Thrust Coefficient } (K_T) &= \frac{T}{\rho n^2 D^4} \\
\text{Torque Coefficient } (K_Q) &= \frac{Q}{\rho n^2 D^5}
\end{aligned}
\tag{2.33}
$$

where T and Q represent the propeller thrust and torque, respectively. As expected, an inclined inflow results in sinusoidal thrust and torque distributions with blade angle. The effect of unsteady term, $\frac{\partial \phi}{\partial t}$, in Bernoulli's equation is not activated until the third revolution to avoid the instability of results, and that is why the K_T and K_Q curves show a shift at the third revolution.

In order to clarify the dependence of the present method on the computational parameters, the convergence of unsteady fully wetted thrust and torque coefficients are examined with number of panels and time step size. The convergence of forces with increasing number of panels is shown in Fig. 2.25. Even in the case of 40×20 panels, the predicted K_T and K_Q agree well with those of the finest grid (60×40).

The convergence of the unsteady wetted forces with varying time step size is shown in Fig. 2.26. The blade angle increment, $\Delta\theta$, shown in figure is directly

60

related to the time increment as follows:

$$\Delta\theta = \omega\Delta t \qquad (2.34)$$

The predicted forces converge with decreasing time step size.

In Figs. 2.27 and 2.28, the first harmonic amplitudes of the forces acting on one blade of the DTMB N4661 propeller for inclination angles $\alpha = 10^o$ and $\alpha = 20^o$, are shown, respectively. The measured forces by [Boswell et al. 1984] are shown with those predicted by the current method and the vortex lattice method (MPUF-3A) [Kinnas and Pyo 1999]. The forces predicted by both vortex lattice method and the current method agree well with those measured in the experiment. For the inclination angle $\alpha = 10^o$ and higher advance ratio, MPUF-3A predicts more accurately the axial force and tangential moment than the current method. However, the tangential force and axial moment predicted by the present method compare much better with the experimental measurements than those predicted by MPUF-3A. Notice that for lower J's the present method predicts all forces and moments more accurately. As the inclined angle increases from 10° to 20°, the remarkable agreement of the current method with the experiment is evident for the all force components. This implies that the fully unsteady wake alignment is necessary to predict accurately forces and moments when the propeller is operating in non-axisymmetric and inclined inflow.

DTMB N4148 propeller

Finally, the convergence of the method is studied for the DTMB N4148 propeller. The geometry of DTMB N4148 propeller and the aligned wake geometry is
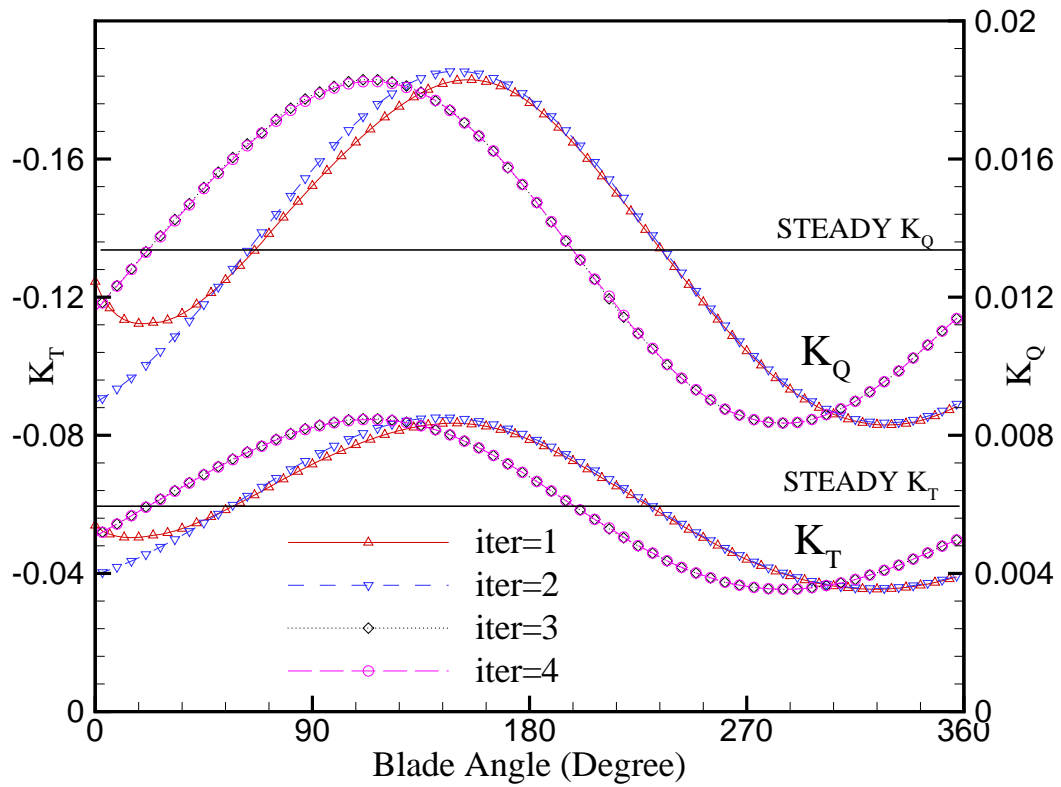
Figure 2.24: Convergence of unsteady fully wetted thrust and torque coefficients with number of propeller revolutions for DTMB N4661: $J_s = 1.0$, $F_n = 4$, $\alpha = 10^o$, and 60×20 panels.
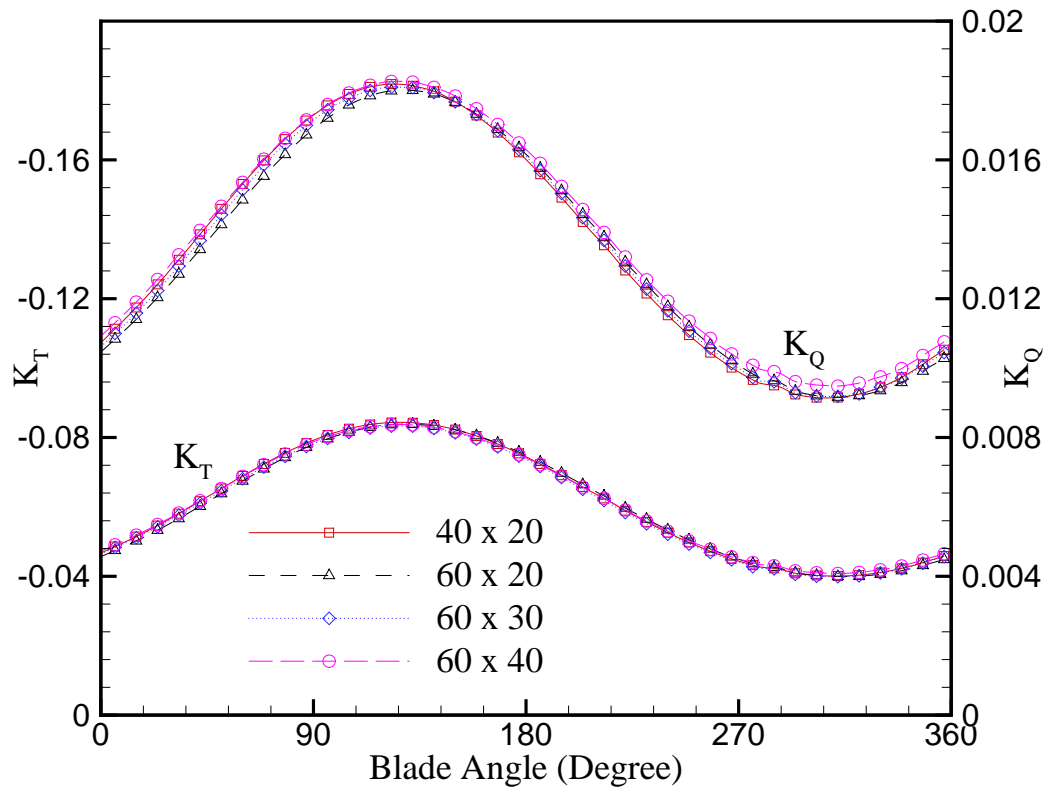
Figure 2.25: Convergence of unsteady fully wetted thrust and torque coefficients with number of panels for DTMB N4661: $J_s = 1.0$, $F_n = 4$, and $\alpha = 10^o$.
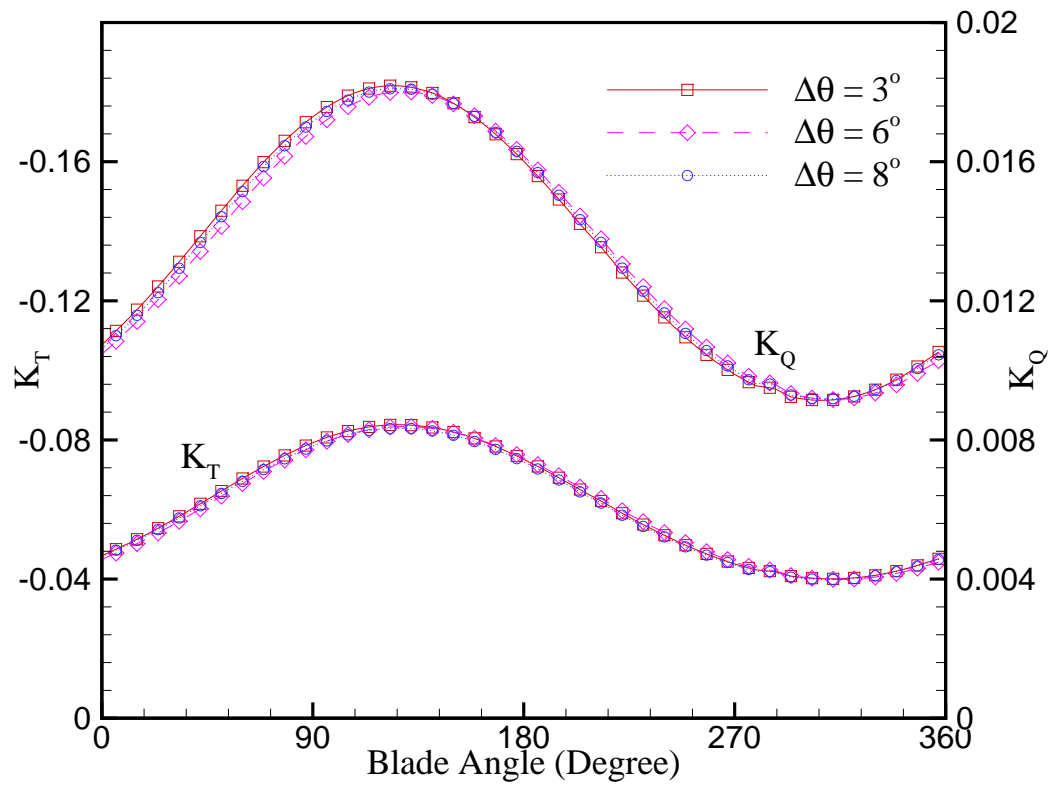
Figure 2.26: Convergence of unsteady fully wetted thrust and torque coefficients with time step sizes for DTMB N4661: $J_s = 1.0$, $F_n = 4$, $\alpha = 10^o$, and 60×20 panels.

First Harmonic Axial Force

First Harmonic Tangential Force

65
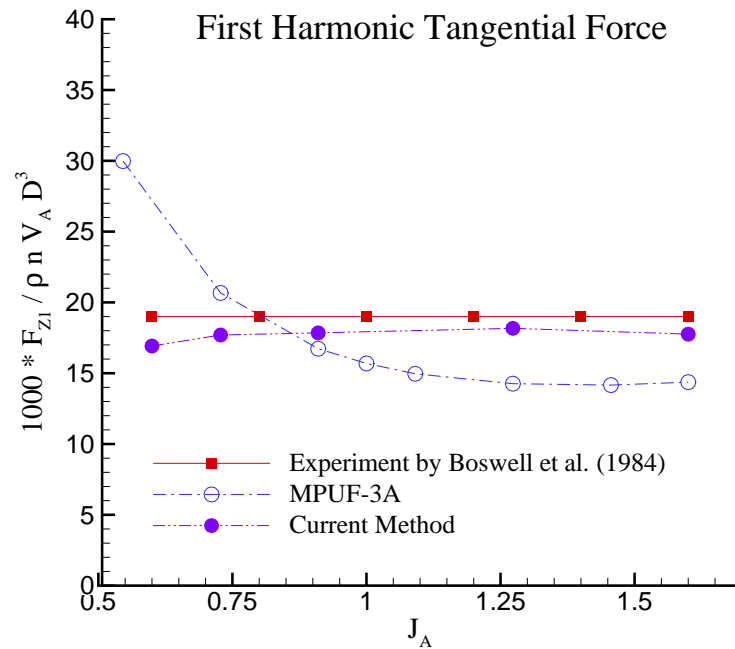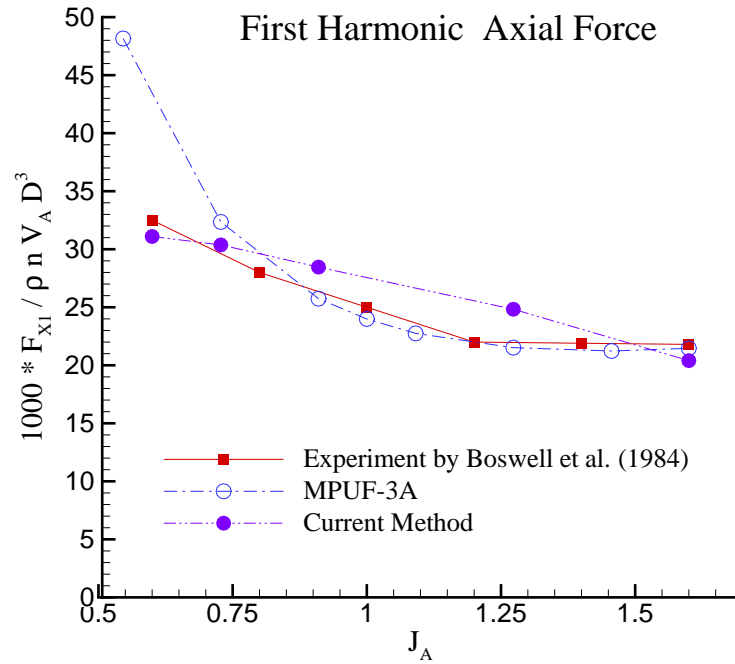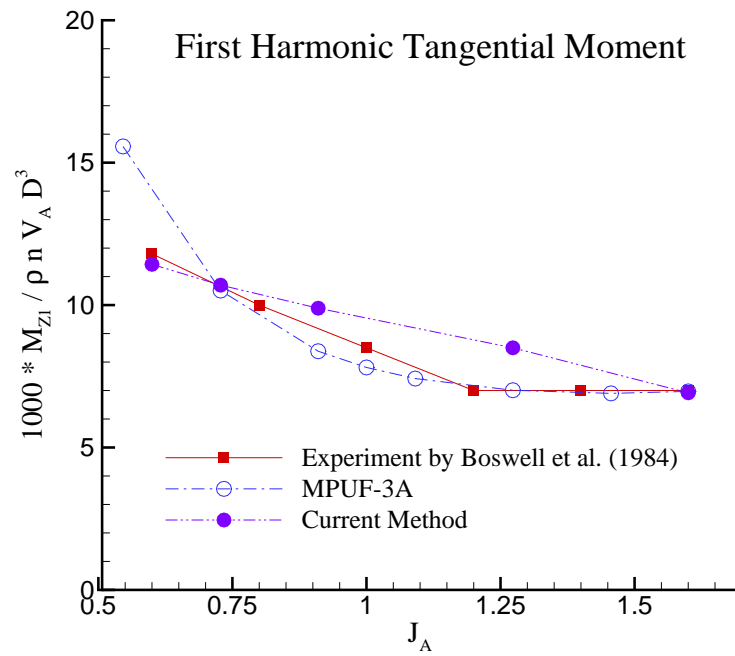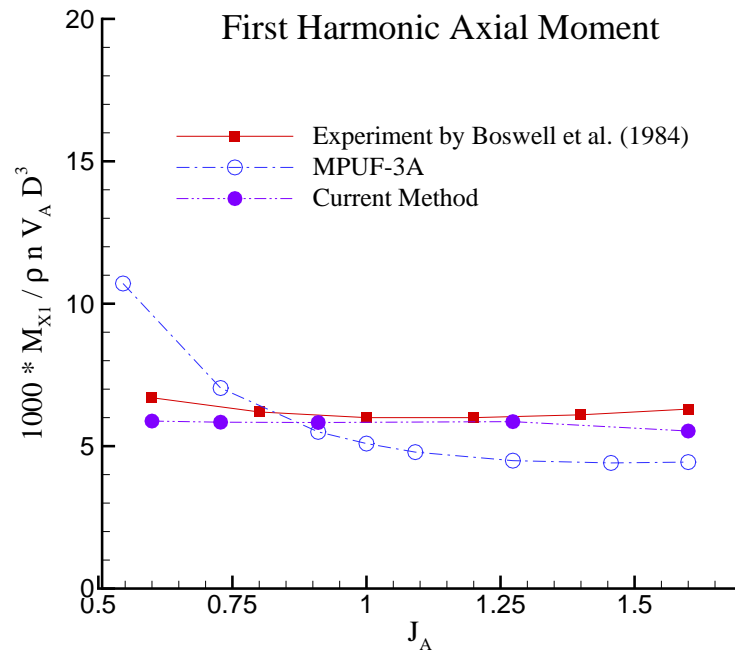
Figure 2.27: The first harmonic of the forces and moments acting on one blade for DTMB N4661: $J_s = 1.0$, $F_n = 4$, $\alpha = 10^o$, and 60×20 panels.

66

First Harmonic Axial Force

First Harmonic Tangential Force
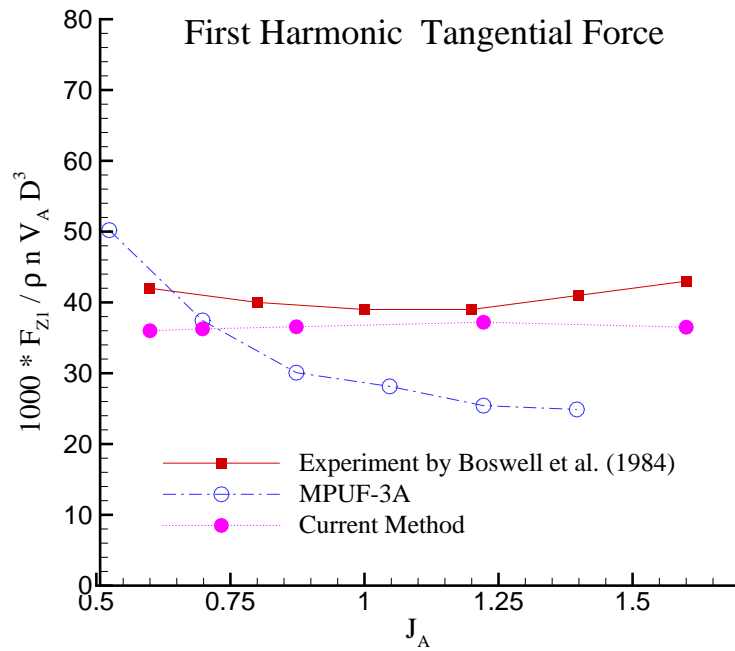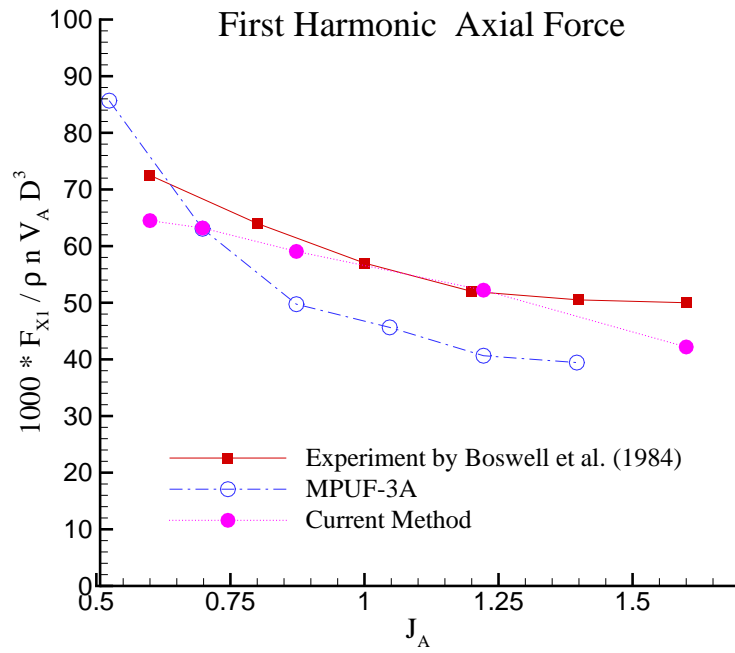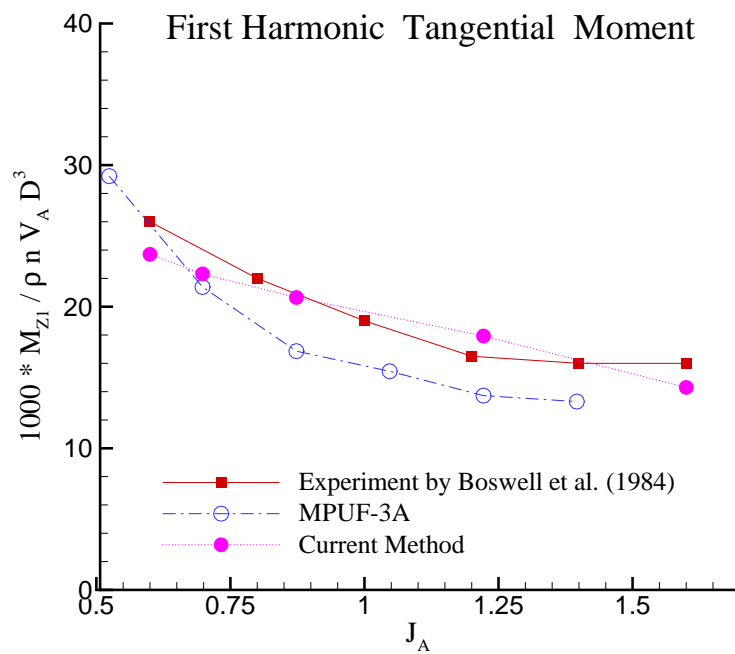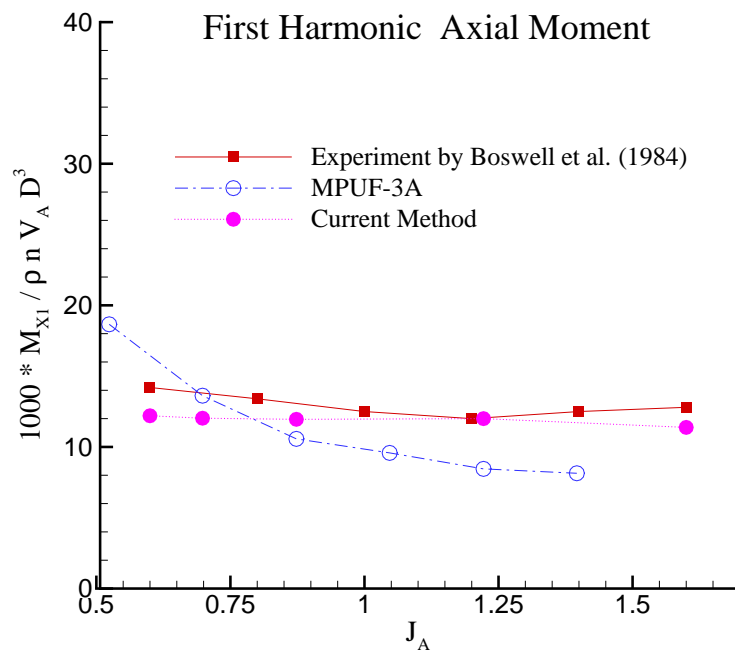
Figure 2.28: The first harmonic of the forces and moments acting on one blade for DTMB N4661: $J_s = 1.0$, $F_n = 4$, $\alpha = 20^o$, and 60×20 panels.
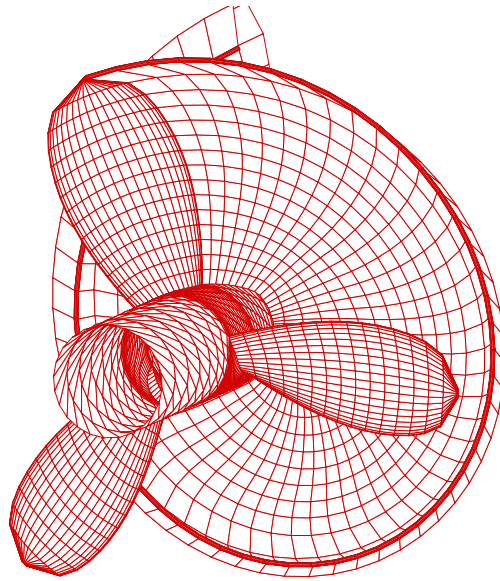
Figure 2.29: Propeller geometry, and its aligned wake geometry for DTMB N4148 propeller.

shown in Fig. 2.29. Figure 2.30 shows a non-axisymmetric inflow wake used for the analysis of the DTMB N4148 propeller. It is a conventional three bladed propeller. The non-axisymmetric inflow (or *effective wake*) which corresponds to the wake in [Mishima et al. 1995] with the effects of the tunnel walls and vortical inflow/propeller interactions is taken into account by using WAKEFF-3D. The tested condition inside the tunnel is $F_n = 9.519$ and $J_s = 0.9087$. [Choi and Kinnas 1998].

Figure 2.31 shows the aligned wake geometries corresponding to the angles of key blade positions. The wake geometries are depicted at the four key blade positions : 0°, 90°, 180°, and 270°. Since the inflow wake is non-axisymmetric, the predicted wake geometries are different from each others.
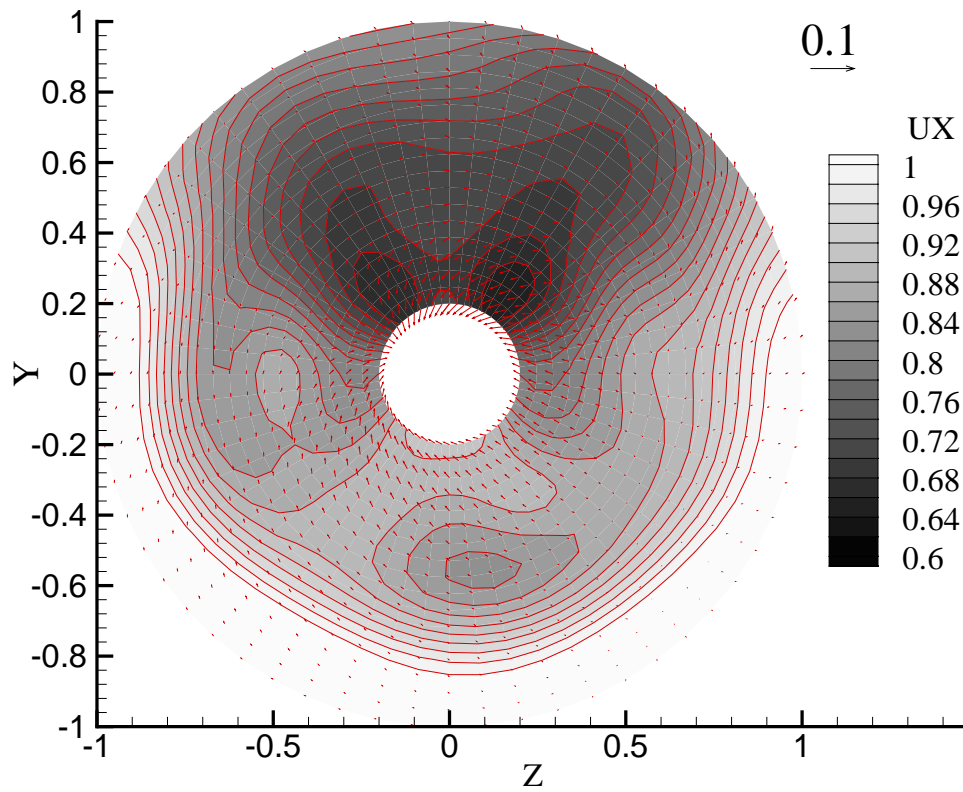
Figure 2.30: Non-axisymmetric inflow wake for DTMB N4148 propeller.

(a) θ = 0°   (b) θ = 90°
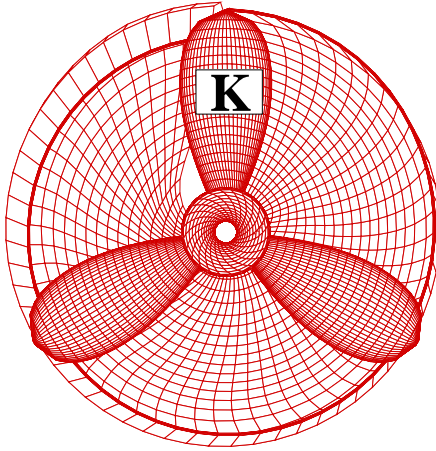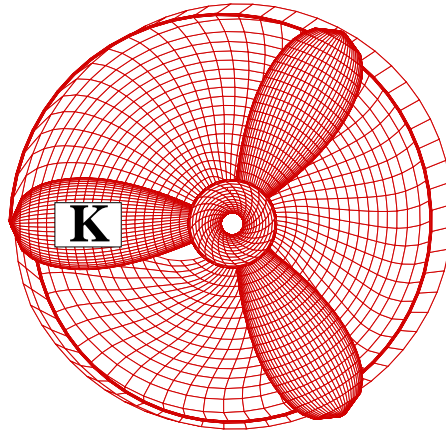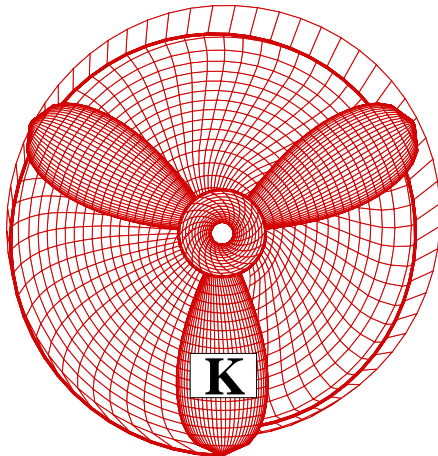
(c) θ = 180°   (d) θ = 270°
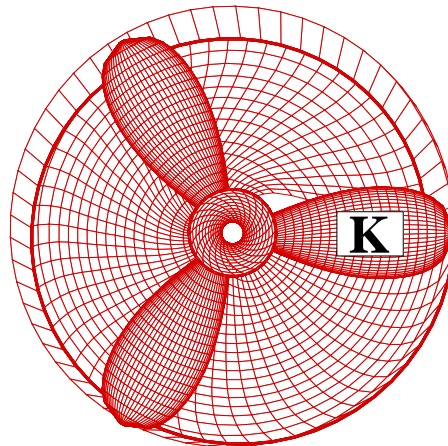
Figure 2.31: The aligned wake geometries at each key blade position for DTMB N4148 propeller. (a) $\theta = 0^o$, (b) $\theta = 90^o$, (c) $\theta = 180^o$, (d)$\theta = 270^o$: $F_n = 9.519$ and $J_s = 0.9087$. K signifies the key blade.
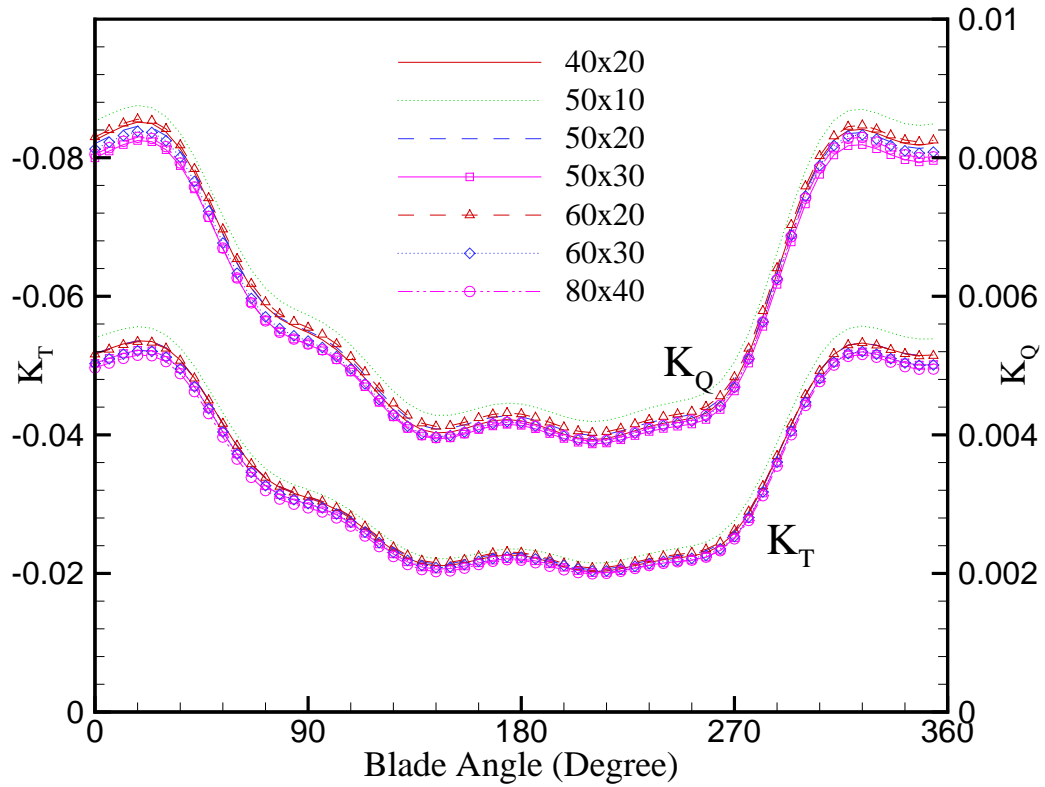
Figure 2.32: Convergence of unsteady fully wetted thrust and torque coefficients (per blade) with number of panels for DTMB N4148 propeller: $J_s = 0.9087$ and $F_n = 9.159$. *Fully unsteady wake alignment*

The dependence of the unsteady fully wetted blade forces on the panel discretization is shown in Fig. 2.32. The predicted blade forces are more sensitive to the number of panels in the spanwise direction than those in the chordwise direction. As shown in figure, the result of 40×20 panels shows better prediction than that of 50×10 panels.

The convergence of unsteady fully wetted forces with time step sizes are shown in Fig. 2.33. The predicted forces are compared for three time step sizes :

72
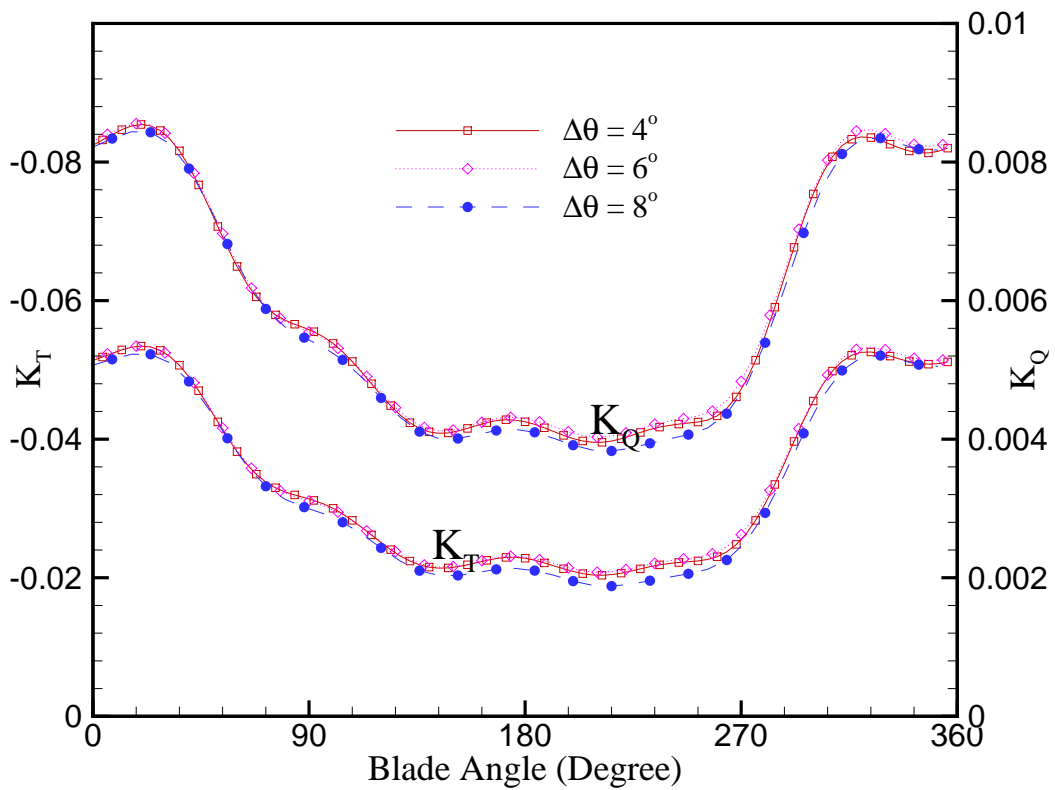
Figure 2.33: Convergence of unsteady fully wetted thrust and torque coefficients (per blade) with time step sizes for DTMB N4148 propeller: $J_s = 0.9087$ and $F_n = 9.159$. *Fully unsteady wake alignment*

4°, 6°, and 8°. As shown in the figure, the results are not much dependent on time step size.

2.6   Summary

A low order boundary element method has been applied to predict the vortex motion of elliptically loaded lifting line, and the geometries of trailing wakes of 3-D hydrofoils and marine propellers in steady and unsteady flow. Details of the formu-

73

lation and numerical treatment for the alignment of the vortex sheet were presented. The numerical results obtained from the present method were compared with those from experiments. The dependence of the results from the present method on the numerical parameters, such as number of panels, time step size and number of iterations, were studied to a great extent.

In order to avoid the instability in evaluating the induced velocities on vortex (wake) sheet, the modeling of finite core tip vortex with circular cross section shape was introduced at the tip of wake sheet. In addition, the induced velocities on the wake sheet were evaluated at slightly deviated points instead of the actual control points on the panels.

The induced velocities on the wake surface were computed directly from the differentiated Green's formula. Also, the velocities around the tip vortex core were evaluated by numerically differentiating the given potentials around the tip vortex core. The new wake surface and the trajectory of the tip vortex core were determined by satisfying the force-free condition on the wake sheet. Numerical validation studies have been performed for the following three problems :

- Elliptically loaded lifting line problem

The method was applied to create the roll-up of an elliptically loaded lifting line. The convergence with number of panels was studied, and the effects of the tip vortex radius and δ were also investigated. The method appeared to converge quickly with number of panels. The results showed that a small value of δ and tip vortex radius were required to create more stable and complete vortex turns. The

74

comparison with Krasny's results was also presented. The general shapes of vortex sheets and rolls-up compared well with each other, however, the present method produced more turns than those of Krasny's due to the use of smaller smoothing value, δ.

- 3-D hydrofoil problem

Next, the method was applied to predict the trailing wake shape of 3-D hydrofoils: one elliptic and one rectangular hydrofoil.

In the case of the elliptic hydrofoil, the convergence of trailing wake geometries with number of panels, and number of iterations were investigated. The trajectory of the tip vortex core was compared with that measured in an experiment. The method produced very quick convergences with number of panels and iterations. The comparison of vortex trajectory showed good agreement with that of the experiment.

In the case of rectangular hydrofoil, the predicted wake sheets were compared with those obtained from high order BEM. Some discrepancies were shown in the roll-up shapes obtained from the present method and the high order methods. However, the rest of the wake shape and the location of tip core predicted by present method agree well with those from the high order methods.

- 3-D propeller problem

Finally, the tip vortex trajectory of DTMB N4119 propeller subjected to uniform inflow was compared with those obtained in experiment and from high

order BEM. DTMB N4661 propeller subjected to an inclined inflow was used to predict the fully unsteady wake geometries The convergence of propeller thrust and torque were studied with number of panels, iterations and time step size. The predicted thrust and torque were found to converge very well. Also, the blade force harmonics predicted by the present method were compared with those obtained from the experiment and lifting surface method. The present method predicted more accurate force harmonics than the lifting surface method, specially at low J's and high angles of inclinations. The force convergence with number of panels and time step size were studied for DTMB N4148 propeller, in non-axisymmetric inflow. The clear unsteadiness was shown in the predicted wake geometries with varying location of key blade.

Since the calculating influence coefficients and solving matrix are repeated at each iteration steps and each time steps for the unsteady wake alignment, it requires a lot of CPU times and computer memory. Example of required CPU times for DTMB N4148 propeller in steady and unsteady analysis is shown in Table 2.1.

Blade Grid	Tip Vortex Grid	Steady	Unsteady
40x10	60x10	10.5 min.	3.0 hours
60x20	60x10	29.0 min.	11.0 hours
80x40	60x10	170.0 min.	47.0 hours

Table 2.1: Approximate CPU time required on a COMPAQ DS20E with 2-833 MHz Processor (approximately 3-times as fast as an 1-GHz Pentium PC) for wake alignment for DTMB N4148 propeller subjected to non-axisymmetric inflow.: J_s=0.9087, F_n=9.159, $\Delta\theta = 6^o$, 6 revolutions for unsteady analysis.

76

Chapter 3

Blade Sheet and Developed Tip Vortex Cavitation

3.1 Previous Research

In this section previous research on the modeling of cavitating flows on hydrofoils and marine propellers is reviewed.

3.1.1 Partially or Super-cavitating Hydrofoils

- Linearized Cavity Theory

A linearized cavity theory for the analysis of 2-D supercavitating hydrofoils was introduced by Tuline at zero cavitation number [Tulin 1953], and at non-zero cavitation number [Tulin 1955]. Linear theory was also applied to the partially cavitating hydrofoils by [Acosta 1955; Geurst and Timman 1956]. In linear theory, the cavity and foil thickness were assumed to be thin relative to the foil chord length. The dynamic boundary condition requiring a constant total velocity on the cavity surface was simplified by satisfying the condition that the horizontal perturbation velocity was constant. The dynamic and kinematic boundary conditions were applied on the projection of the hydrofoil surface on the free stream axis.

Contrary to the experimental evidence, however, linear theory predicts the increasing cavity extent and volume with increasing foil thickness at the same flow

77

conditions. The breakdown of linear theory near a round leading edge was recently accounted by introducing a nonlinear *leading edge correction* by [Kinnas 1991].

- Vortex Lattice Methods (VLM)

[Widnall 1966] first employed a numerical pressure doublet and source lifting surface technique for the analysis of supercavitating three dimensional hydrofoils in unsteady flow. [Jiang and Leehey 1977] applied a discrete vortex and source lattice lifting surface method, and introduced an iterative scheme to determine the cavity planform by imposing a uniform pressure condition on the cavity along the chordwise as well as the spanwise direction. The partially cavitating [Kinnas 1984] and supercavitating [Kinnas 1985a] hydrofoil problems were numerically solved by using the source and vorticity distribution. Later, this method was extended to include non-linear leading edge corrections in the case of the partially cavitating [Kinnas 1985b], and in the case of the supercavitating hydrofoils [Fine and Kinnas 1993b] with arbitrary detachment on both sides of the hydrofoil.

- Boundary Element Method (BEM)

The velocity based BEM, or the potential based BEM have been applied on partially and super-cavitating hydrofoils.

The velocity based BEM was used by [Pellone and Rowe 1981] for 2-D and 3-D super cavitating hydrofoils, by [Uhlman 1987, 1989] for 2-D partially and super cavitating hydrofoils. [Lemonnier and Rowe 1988] applied the velocity based BEM

for partially cavitating 2-D hydrofoils, and [Achkinnadze and Krasilnikov 2001] for partially cavitating 3-D hydrofoils.

The potential based BEM for the prediction of nonlinear partial and super-cavity on 2-D and 3-D hydrofoils was developed by [Kinnas and Fine 1990, 1993; Fine and Kinnas 1993b]. Their method was extended by [Kinnas et al. 1994] to predict the viscous flow around cavitating hydrofoils by coupling inviscid BEM with boundary layer solver [Esposito and Salvatore 2000; Salvatore and Esposito 2001]. Recently, the free surface effect on 2-D and 3-D cavitating hydrofoils moving with constant speed under the free surface was presented by [Bal et al. 2001].

A similar cavity prediction method was developed and applied for 2-D partially and super cavitating hydrofoils by [Lee et al. 1992] , and for 3-D steady and unsteady cavitating hydrofoils by [Kim et al. 1994]. Also, the potential based BEM was applied for the heave and sinusoidal gust motion of a cavitating hydrofoil under a free surface by [Kim and Lee 1993] for 2-D cavitating hydrofoils, and by [Ando and Nakatake 2001] for 3-D hydrofoils.

3.1.2   Blade Sheet Cavitation on Propellers

- Vortex Lattice Method (VLM)

A VLM using the linearized cavity theory was developed to analyze 3-D unsteady sheet cavitation of marine propellers subjected to non-uniform inflows by [Lee 1979, 1981; Breslin et al. 1982]. However, the linear theory predicts longer cavity extent as the blade thickness increases, and that is contrary to the non-linear

79

theory [Uhlman 1987] as well as the short cavity theory [Tulin and Hsu 1980]. The method of [Lee 1979; Breslin et al. 1982] (with the corresponding code called PUF-3), was then modified to take into account the non-linear blade thickness effect [Kerwin et al. 1986] by introducing the *leading edge correction* [Kinnas 1985b, 1991] (the revised code was renamed to PUF-3A). In [Kinnas and Fine 1989], PUF-3A was extended to predict unsteady partial sheet cavitation with prescribed mid-chord and/or face cavity detachment. Their method was extended to treat supercavitating propellers subjected to steady flow by [Kudo and Kinnas 1995]. The search algorithm for cavity detachment in the case of back mid-chord cavitation was added by [Kinnas et al. 1999] (the revised code was renamed MPUF-3A). The hub effects using the image method [Kinnas and Coney 1992], the effect of the nonlinear thickness-loading coupling [Kinnas 1992], a B-spline representation of the blade geometry [Mishima and Kinnas 1996], and the wake alignment in uniform and inclined inflow [Kinnas and Pyo 1997, 1999; Lee and Kinnas 2001b] have been also incorporated in MPUF-3A.

- Boundary Element Method (BEM)

Since the BEM discretizes the exact blade surface instead of the mean camber surface, the BEM inherently includes the effect of thickness-loading coupling. As a result, the BEM predicts more accurately the pressures and cavity flow details at the propeller leading edge, trailing edge, and tip, where the linear cavity theory breakdowns in the VLM. The BEM uses more panels near the blade leading and

80

trailing edges to observe the flow details, and eventually requires more CPU time and computer memory.

BEM has been applied extensively for the analysis of propeller performance and has been very successful in steady and unsteady non-cavitating conditions. [Hess and Valarezo 1985] adopted the velocity based BEM to compute the steady flow field around a propeller. [Lee 1987; Kerwin et al. 1987] used the perturbation potential based BEM for the analysis of propeller in steady flow. The unsteady performance of marine propeller has been solved by [Hsin 1989; Kinnas and Hsin 1992], in which the hyperboloidal geometry panel was used for more accurate expressions of the influence coefficients in the case of highly skewed propellers.

Non-linear potential based BEM was first applied for the analysis of the cavitating propeller subjected to non-axisymmetric inflows by [Kinnas and Fine 1992; Fine and Kinnas 1993a]. The method was initially developed to predict propeller back cavitation with prescribed cavity detachment location, and the corresponding code was named PROPCAV. [Kim and Lee 1996] developed a similar BEM to predict the unsteady cavitating propeller performance. PROPCAV was extended to predict face and/or back cavitation with searched cavity detachment by [Kinnas et al. 1997; Mueller and Kinnas 1997; Mueller 1998; Mueller and Kinnas 1999], and to treat the mixed partial and supercavity patterns on both face and back sides of the blade simultaneously by [Young and Kinnas 1999b, 2001a]. Recently, PROP-CAV was further extended to treat supercavitating propellers with finite thickness trailing edge as well as surface piercing propellers by [Young and Kinnas 2001b; Young 2002; Young and Kinnas 2002],

3.1.3 Tip Vortex Cavitation

Most research on tip vortex cavitation was initially focused on the development of correlations of cavitation inception between model and prototype. More recently there have been attempts to determine cavitation inception based on Reynolds Averaged Navier-Stokes method. A more recent work [Hsiao and Chahine 2002] determines bubble entrainment in a propeller tip vortex and its effect on cavitation inception.

The prediction of tip vortex cavitation on vortex systems trailing from lifting surfaces was first studied by [McCormick 1954, 1962] using a semi-empirical formulation. He assumed that the boundary layer thickness, δ, developed over the lower surface of the wing at the tip of the trailing edge and the thickness of the starting vortex sheet (or vortex core radius, a) are the same. In addition, he proposed a power law relation, $\delta \propto Re^{-n}$, between the boundary layer thickness, δ, and the local Reynolds number, Re[1]. He obtained a value of $n = 0.35$ from experimental data, and later it was turned out to be $n = 0.4$. A value of $n = 0.4$ appeared reasonable for a transitional boundary layer [Arndt and Dugue 1992; Naubes and Arndt 1997], since that value is 0.5 for the laminar, and 0.2 for the turbulent boundary layer over flat plate [Schlichting 1979]. Although McCormick's empirical formula has shown disagreement with experimental results, his suggestion that vortex core radius is proportional to the boundary layer thickness, has been widely used, and

---

[1]According to the definition in [McCormick 1954, 1962], $Re = VC_m/\nu$ is a local Reynolds number based on mid span chord, where V is the incoming flow velocity, ν is the kinematic viscosity, and C_m is the mid span chord of the foil.

led to the relation for a turbulent boundary layer $\delta \propto Re^{-0.2}$ [Billet and Holl 1981; Fruman et al. 1992, 1995; Astolfi et al. 1999].

The minimum pressure, $-C_{P_{min}}$, at the cavity core has to vary as $(\Gamma/a)^2$, and the vortex strength Γ depends on the lift coefficient (C_l) of foil. From the relation between minimum pressure, cavity core radius, and vortex strength, the scaling relation has been predicted as

$$C_{P_{min}} \propto -KC_l^2 Re^m \qquad (3.1)$$

where K is the positive constant depending on the foil section geometry. [McCormick 1962; Platzer and Souders 1980] proposed $m = 0.36$, and later that value was corrected as $m = 0.4$ for the three-dimensional hydrofoil with elliptic loading by [Billet and Holl 1981; Fruman et al. 1992, 1995; Astolfi et al. 1999]. In [Hsu 1991], the correlation law with $m = 0.64$ was applied for marine propellers, which are based on typical propeller series.

The influences of air and nuclei content on tip vortex cavitation inception were investigated for elliptic hydrofoils by [Arndt et al. 1991; Arndt and Keller 1992]. They observed that tip vortex cavity trajectory is independent of the physical parameters such as angle of attack, Reynolds number, cavitation number and dissolved gas content [Arndt et al. 1991]. [Gowing et al. 1995; Briançon-Marjolet and Merle 1996] also investigated the effects of oxygen and nuclei content on tip vortex cavitation.

[Szantyr 1994] tried to model tip vortex cavitation based on the Rankine vortex model, assuming that the vorticity is concentrated inside a vortex core. In

his model, the flow field outside the vortex core is irrotational, and the core itself rotates as a rigid body which is modeled by the source distribution. He estimated the diameter of a cavitating tip vortex by using the following formula,

$$D_{TV} = \left(\frac{2}{\sigma}\right)^{1/2} \frac{\Gamma}{\pi U_\infty} \tag{3.2}$$

where Γ is the vortex strength of the trailing wake.

[Rule and Bliss 1998] developed a numerical model of a fully developed trailing vortex with a viscous core. [Kinnas et al. 1998; Lee and Kinnas 2001a] developed a potential based panel method to predict the shape of a tip vortex cavity far downstream in the case of the simplified horseshoe problem, and obtained a constant pressure on the cavity surface which is equal to the corresponding cavitation number.

3.2   2-D Tip Vortex Cavity

A 2-D tip vortex cavity problem is first considered to study the numerical characteristics of the method.

3.2.1   Problem Definition

Consider a simplified 2-D vortex system of two vortices of equal and opposite sign which are distance R apart, as shown in Fig. 3.1. The vortex on the right is allowed to cavitate and its original shape is considered to be a circle of radius $r_o{}^2$.

---

[2]In reality, the vortex on the left would cavitate too. However, its effect on the tip vortex cavity is expected not to be that different from that of a non-cavitating vortex. Thus, for simplicity we consider that the vortex on the left is not cavitating.
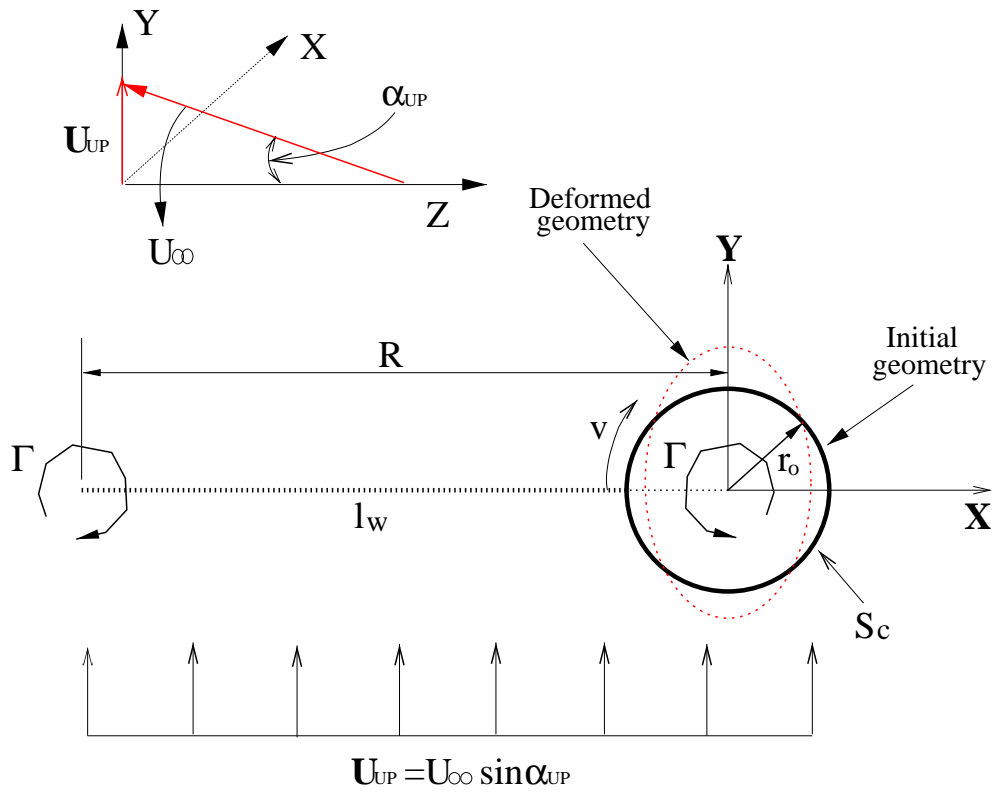
Figure 3.1: Modeling of 2-D tip vortex cavity.

A circulation with strength, Γ, is located at the center of tip vortex cavity, as well as at the end of vortex line. If that vortex system is released, it would move downward due to the downwash induced by the two rotating vortices. In order to fixed the movement of the vortex system, an upward velocity corresponding to the downwash is applied to the vortex system. The magnitude of upward velocity is given by

$$U_{up} = \frac{\Gamma}{2\pi R} = U_\infty \sin\alpha_{up} \tag{3.3}$$

where the values of R and U_∞ (U_∞ is considered to be along the axis of the vortex, i.e. normal to the paper) are taken equal 1 in this problem.

3.2.2 Formulation

By the definition of this problem, the vorticity is concentrated at the core of the tip vortex cavity, and the resulting flow outside of the vortex system is considered as irrotational, inviscid and incompressible. In this case, the total flow velocity, $\vec{q}_t$, can be written in terms of the perturbation potential, $\phi(x, y)$, as follows:

$$\vec{q}_t = \vec{q}_{in}(x, y) + \nabla\phi(x, y) \tag{3.4}$$

where

$$\vec{q}_{in}(x, y) = (0, U_{up}) = (0, U_\infty \sin\alpha_{up}) \tag{3.5}$$

The perturbation potential, $\phi(x, y)$ satisfies the Laplace equation in the fluid domain.

$$\nabla^2\phi(x, y) = 0 \tag{3.6}$$

86

Thus, the perturbation potential on the boundary S_c of the vortex system is represented by Green's third identity.

$$\pi\phi_p = \int_{S_c} \left[\phi_q \frac{\partial \ln r(p;q)}{\partial n_q} - \frac{\partial \phi_q}{\partial n_q} \ln r(p;q) \right] dl + \int_{C_w} \Gamma_q \frac{\partial \ln r(p;q)}{\partial n_q} dl \qquad (3.7)$$

where $r(p;q)$ is the distance between p and q. p and q represent the control point and the variable point on the boundary, respectively. $\vec{n}$ is the unit normal vector which points into the fluid domain on the cavity surface.

Equation 3.7 can be solved via two different methods:

- Direct method : the potential, ϕ, is first evaluated on the assumed cavity surface, and then the cavity shape is determined using the normal derivative of the potential, $\frac{\partial \phi}{\partial n}$ (obtained from inverting Green's formula).

- Jacobian method : the normal derivative of potential is assumed to be known, and the cavity shape is determined using a Newton-Raphson scheme.

3.2.3 Direct Method

In the direct method, the potential on the tip vortex cavity surface is evaluated from the dynamic boundary condition, and the shape is adjusted using the kinematic boundary condition. The boundary conditions which have to be satisfied on the vortex system are as follows:

- Dynamic boundary condition on cavity surface : The pressure inside or on the tip vortex cavity surface is constant and equal to the cavitating pressure, P_c.

87

$$P = P_c \tag{3.8}$$

The relation between cavitation number and the total velocity on the tip vortex cavity is given by applying Bernoulli's equation. Bernoulli's equation can be expressed as follows,

$$\frac{P_o}{\rho} + \frac{U_{up}^2}{2} = \frac{P}{\rho} + \frac{|\vec{q}_t|}{2} \tag{3.9}$$

and the pressure coefficient is derived as follows :

$$-C_P = \frac{P_o - P}{\frac{\rho}{2} U_\infty^2} = \left(\frac{|\vec{q}_t|}{U_\infty}\right)^2 - \left(\frac{U_{up}}{U_\infty}\right)^2 \tag{3.10}$$

The cavitation number, σ,

$$\sigma = \frac{P_o - P_c}{1/2\rho U_\infty^2} \tag{3.11}$$

and the magnitude of the total tangential velocity on the cavity, $|\vec{q}_t|$, is found to be constant:

$$|\vec{q}_t| = U_\infty \sqrt{\sigma + \sin^2 \alpha} \tag{3.12}$$

Also, the total velocity on the tip vortex cavity surface can be expressed in terms of the total tangential velocity on tip vortex surface.

$$|\vec{q}_t| = \frac{\partial \phi}{\partial v} + \frac{\partial \Phi_{in}}{\partial v} \tag{3.13}$$

Then, the perturbation velocity, $\frac{\partial \phi}{\partial v}$, is given by combining Eqns. 3.12 and 3.13.

$$\frac{\partial \phi}{\partial v} = -\frac{\partial \Phi_{in}}{\partial v} + U_\infty \sqrt{\sigma + \sin \alpha_{up}^2} \tag{3.14}$$

The perturbation potential on the tip vortex cavity is determined by integrating Eqn. 3.14 along the circumference of the tip vortex cavity.

$$\begin{aligned} \phi(x, y) &= \phi_o + U_\infty y \sin \alpha_{up} + U_\infty \sqrt{\sigma + \sin \alpha_{up}^2} \int_0^v dv &\tag{3.15}\\ &= \phi_o + U_\infty y \sin \alpha_{up} + U_\infty \sqrt{\sigma + \sin \alpha_{up}^2}\, v &\tag{3.16} \end{aligned}$$

88

Since the solution of Laplace equation for the velocity potential is uniquely determined up to an additive constant [Newman 1977], the constant ϕ_o can be a arbitrary value, and $\phi_o = 0$ is used in this method. Finally, the potential on tip vortex cavity surface is defined as follows:

$$\phi(x, y) = U_\infty \left[y \sin \alpha_{up} + v \sqrt{\sigma + \sin^2 \alpha_{up}} \right] \tag{3.17}$$

- Kinematic boundary condition on cavity surface : the substantial derivative of the cavity surface vanishes.

$$\frac{D}{Dt} [n - h(v)] = \left(\frac{\partial}{\partial t} + \vec{q}_t \cdot \nabla \right) [n - h(v)] \tag{3.18}$$

where n is the coordinate normal to the cavity surface, and $h(v)$ is the increment of cavity thickness normal to the previous cavity surface at point v. The gradient ∇ in the local coordinate (v, n) is defined as follows:

$$\nabla = \vec{v} \frac{\partial}{\partial v} + \vec{n} \frac{\partial}{\partial n} \tag{3.19}$$

By substituting Eqn. 3.19 into Eqn. 3.18, the kinematic boundary condition renders the following partial differential equation for the increment of cavity height, h:

$$\frac{\partial h}{\partial v} |\vec{q}_t| = \frac{\partial \Phi}{\partial n} = \frac{\partial \phi}{\partial n} + \vec{q}_{in} \cdot \vec{n} \tag{3.20}$$

- Numerical Implementation

The potential on the tip vortex cavity surface is known as in Eqn. 3.15. Thus, Eqn. 3.7 is solved for the unknown, $\frac{\partial \phi}{\partial n}$, until the kinematic boundary condition is

89

satisfied on the tip vortex cavity surface. The initial radius of tip vortex cavity, r_o is given from the dynamic boundary condition:

$$\frac{\Gamma}{2\pi r_o} = U_\infty \sqrt{\sigma + \sin^2 \alpha_{up}} \tag{3.21}$$

After the BVP is solved, the initial cavity shape is adjusted using Eqn. 3.20. In order to find the increment of tip vortex cavity height at the panel nodal points, the central difference scheme is applied at the control point (CP) using the values of $\frac{\partial \Phi}{\partial n}$ and q_t, as shown in Fig. 3.2. The equation for the cavity height increment is given by

$$h_{i+1} - h_i = \left(\frac{\partial \Phi}{\partial n}\right)_i \frac{\Delta v_i}{|\vec{q_t}|} \tag{3.22}$$

with the periodic condition

$$h_1 = h_{MC+1}. \tag{3.23}$$

where MC is the total number of panels on the tip vortex cavity.

3.2.4   Jacobian Method

The shape of 2-D tip vortex cavity can be also determined by using the Jacobian method. In this method, the tip vortex cavity shape is assumed to be known, i.e., $\frac{\partial \phi}{\partial n}$ is known, and ϕ is obtained as a solution of Eqn. 3.7. The boundary conditions for this method are as follows:

- Dynamic boundary condition : the pressure on the cavity surface is constant and equal to the cavity pressure.

$$P = P_c \tag{3.24}$$

90
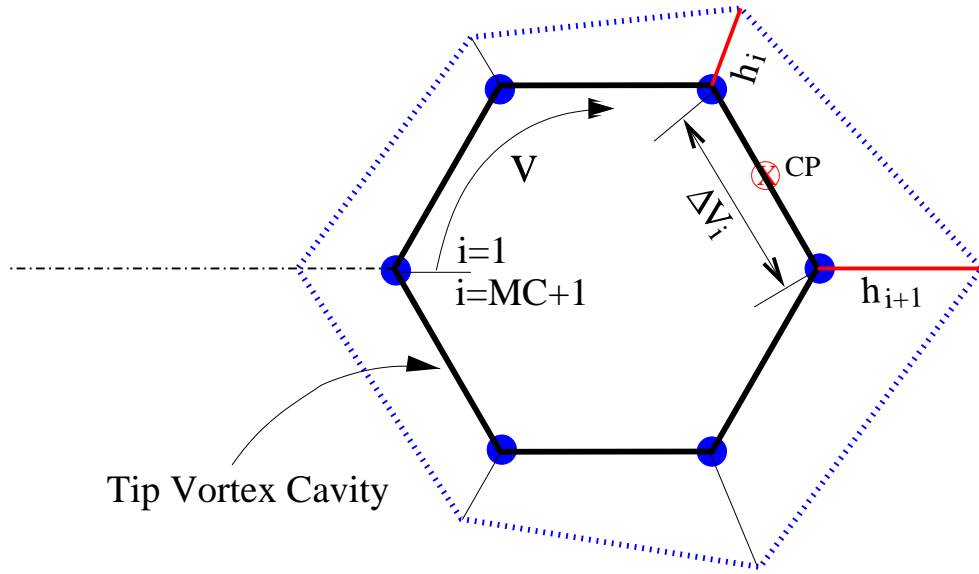
Figure 3.2: Definition of the increment of cavity height, h, and the paneling of tip vortex cavity.

or

$$-C_p = \sigma \tag{3.25}$$

- Kinematic boundary condition : The fluid flow is tangent to the cavity surface.

$$\frac{\partial \phi}{\partial n} = -\vec{q}_{in} \cdot \vec{n} \tag{3.26}$$

- Numerical Implementation

Since the integral equation is solved for the assumed tip vortex cavity, tip vortex cavity shape is determined from the solution potential (more precisely, the computed pressure). A Newton-Raphson technique is applied to determine the cavity heights at each control point based on the following equation.

$$\delta p(h; \sigma) = 0 \tag{3.27}$$

91

where $\delta p = -C_p - \sigma$. Equation 3.27 is solved for the circumferential grid by applying a MC-dimensional (if the circumferential number of panel is MC) Newton-Raphson scheme. The updated cavity heights for the $(k+1)^{th}$ iteration are given as follows:

$$[h]^{k+1} = [h]^k - [J]^{-1}[\delta p]^k \tag{3.28}$$

where

$$\begin{aligned} [h]^T &= [h_1, h_2, ..., h_{MC}] \\ [\delta p]^T &= [\delta p_1, \delta p_2, ..., \delta p_{MC}] \end{aligned} \tag{3.29}$$

and $[J]$ is the Jacobian, which is defined as

$$J_{ij} = \frac{\partial \delta p_i}{\partial h_j}, \qquad 1 \leq i, j \leq MC \tag{3.30}$$

A two point finite difference scheme is used to evaluate the Jacobian. Also, in order to accelerate the Newton-Raphson scheme, the off-diagonal terms of the Jacobian are ignored in solving Eqn. 3.28. Thus, this method requires only a single solution of the system of equations for each Newton-Raphson iteration.

3.2.5 Numerical Results

Figure 3.3 shows the initial and the converged tip vortex cavity shapes predicted by using the direct method. $\Gamma = 0.2193 \ (m^2/sec)$, $\sigma = 0.1$, and the corresponding upward velocity $U_{up} = U_\infty \sin 2^o \ (m/sec)$ are used. The initial radius of the tip vortex cavity is $r_o = 0.11R \ (m)$. The tip vortex cavity shape converges to the elliptic shape from the initial circle, and the shape changes very little due to

92
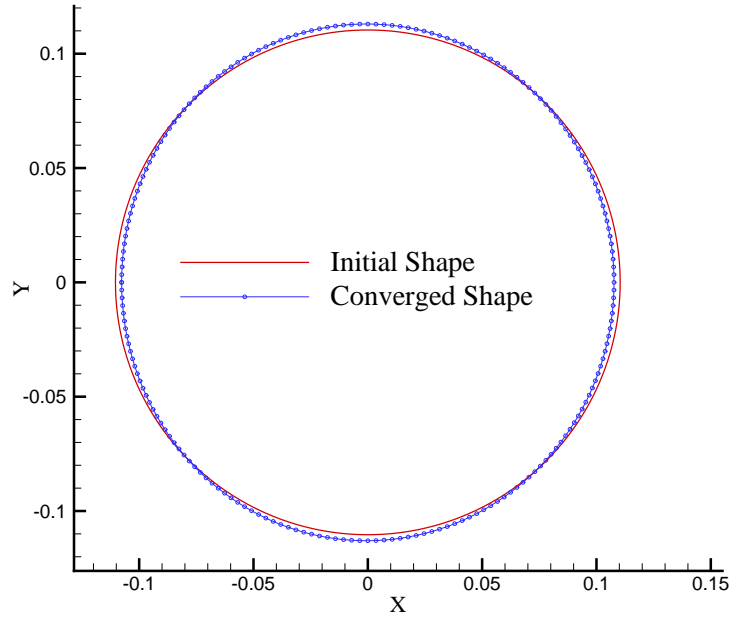
Figure 3.3: Comparison of the initial and the converged tip vortex cavity cross section (Direct method): $\Gamma = 0.2193 \ (m^2/sec)$, $\sigma = 0.1$, and $\alpha_{up} = 2^o$.

the lightly loaded circulation. The pressure on the initial and the converged cavity surfaces are shown in Fig. 3.4. While the pressure is varying around the tip circumference in the case of the initial shape, the converged pressure, $-C_p$, is constant and equal to the cavitation number $\sigma = 0.1$.

Figure 3.5 shows the predicted converged tip vortex cavity shape with varying number of circumferential panels in the case of $\Gamma = 0.4383 \ (m^2/sec)$, $\sigma = 0.1$, the upward velocity $U_{up} = U_\infty \sin 4^o \ (m/sec)$, and the initial tip radius $r = 0.215R \ (m)$. The direct method is used to predict the tip vortex cavity shape. The cavity shape converges quickly with number of circumferential panels, and the converged shape deformed more than the case of $\Gamma = 0.2193 \ (m^2/sec)$ due to
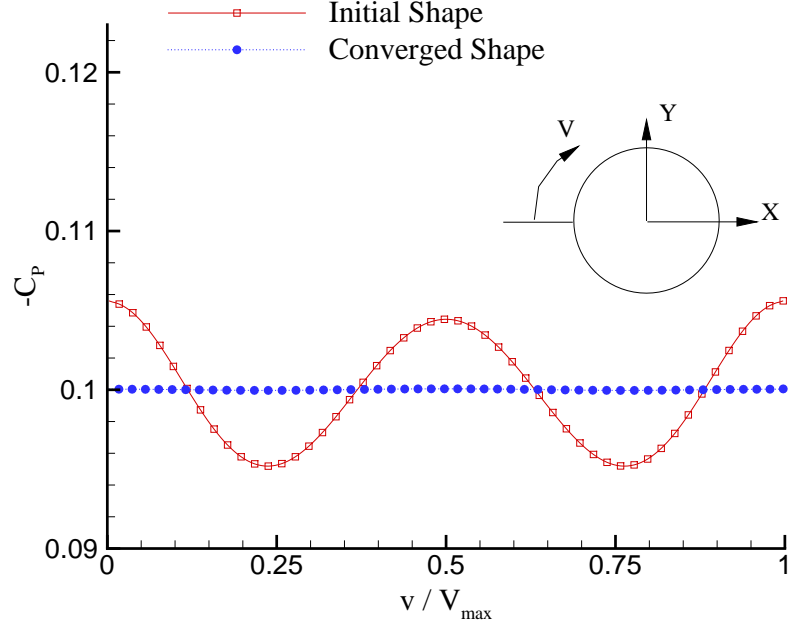
Figure 3.4: Pressure distribution along the tip vortex cavity circumference for the initial and the converged shape (Direct method): $\Gamma = 0.2193 \ (m^2/sec)$, $\sigma = 0.1$ and $\alpha_{up} = 2^o$.

the stronger vortex strength.

Although the tip vortex cavity shape converges very quickly, as shown in Fig. 3.5, the pressure on the cavity surface shows very slow convergence with number of panels, as shown in Fig. 3.6. Compared with fine grids, the pressures of the coarse grids ($MC = 10$, and 20) show relatively bigger error. The pressure error obtained for the converged cavity shape is depicted in Fig. 3.7 as a function of number of panels. The error is defined as

$$||error|| = \frac{\sum_{m=0}^{m=MC}((-C_p)_m - \sigma)^2}{MC} \tag{3.31}$$

94
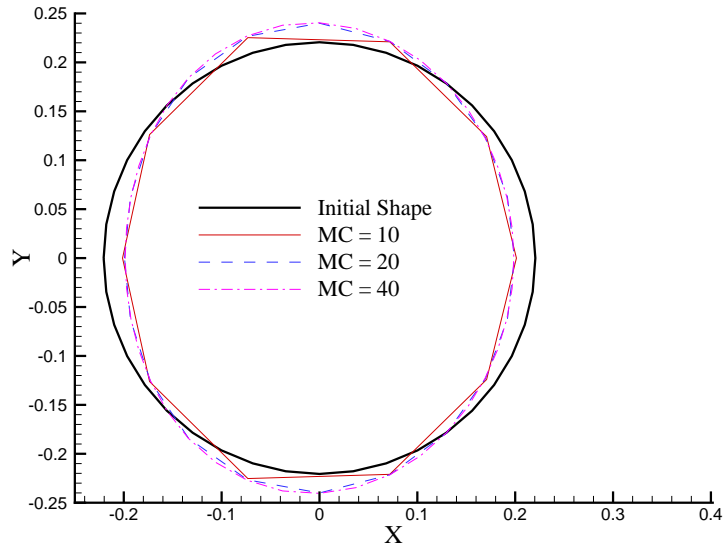
Figure 3.5: Convergence of tip vortex cross-section shape with number of panels on tip vortex cavity (Direct method): Γ=0.4383(m^2/sec), σ=0.1 and α_{up}=4°.

With increasing the number of panels, the plot of $\log\|error\|$ versus $\log(MC)$ produces a straight line until $MC = 80$. For the large number of panels, however, the rate of error change drastically decreases, and becomes almost "zero". Therefore, the accuracy of pressure on the predicted cavity surface can not be improved by increasing number of panels, if the number of panels is more than 80.

Figure 3.8 shows the comparison of the predicted tip vortex cavity shapes using the direct and Jacobian methods. The conditions are $\Gamma = 0.4383\ (m^2/sec)$, $\sigma = 0.1$ and $\alpha_{up} = 4^o$, and the total number of panels on tip vortex cavity surface is 160. As shown in figure, the predicted cavity shapes by both methods agree well to each other. However, the pressures computed from two methods show some discrepancies, as shown in Fig. 3.9. The convergence criteria of both methods are
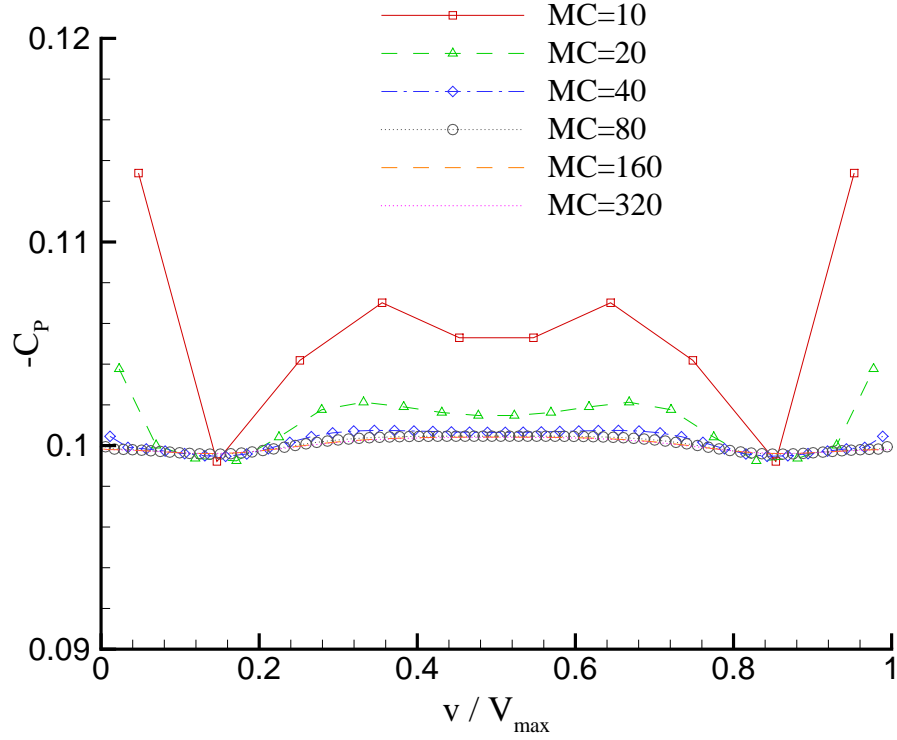
Figure 3.6: Convergence of pressure distribution with number of panels on the tip vortex cavity (Direct method): $\Gamma = 0.4383\ (m^2/sec)$, $\sigma = 0.1$ and $\alpha_{up} = 4^o$.

as follows:

$$max\left\{\frac{h_{new} - h_{old}}{h_{old}}\right\} < \epsilon \tag{3.32}$$

where $\epsilon = 10^{-6}$. Since the tip vortex cavity radius is small, the small difference in the tip vortex cavity shape can produce big differences in the pressure distributions.

96
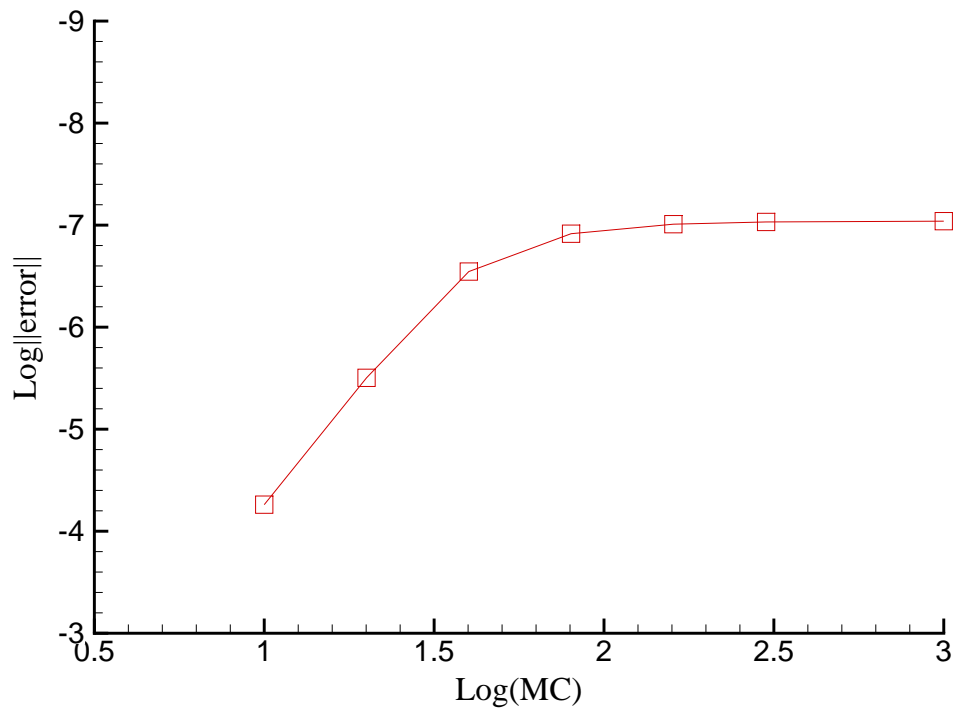
Figure 3.7: Log-log plots of errors as a function of number of panels on tip vortex cavity (Jacobian method): $\Gamma = 0.4383 \ (m^2/sec)$, $\sigma = 0.1$ and $\alpha_{up} = 4^o$.
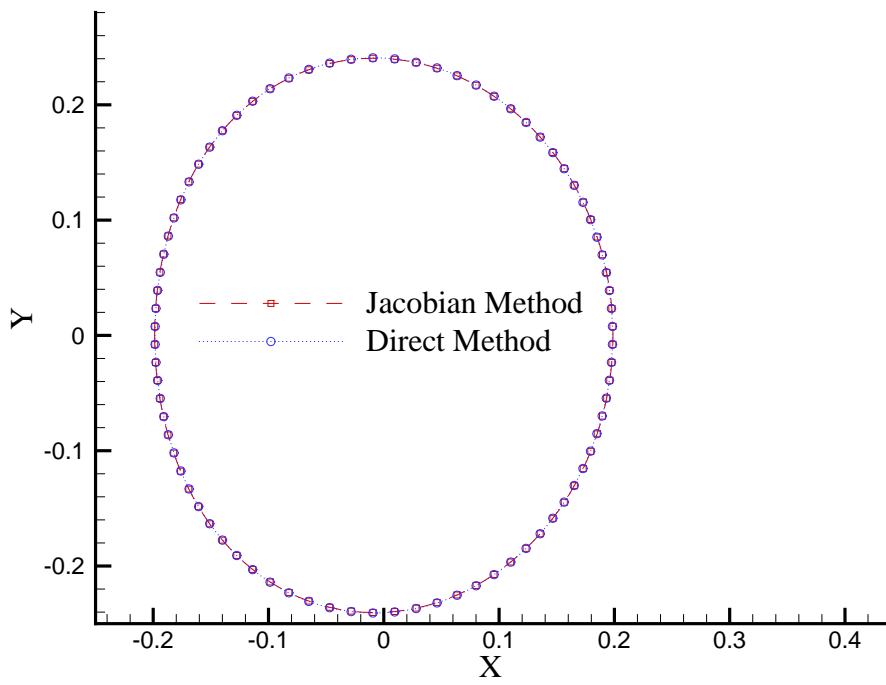
Figure 3.8: Comparison of tip vortex cavity shapes predicted by direct and Jacobian methods with $MC = 160$: $\Gamma = 0.4383 \ (m^2/sec)$, $\sigma = 0.1$ and $\alpha_{up} = 4^o$.
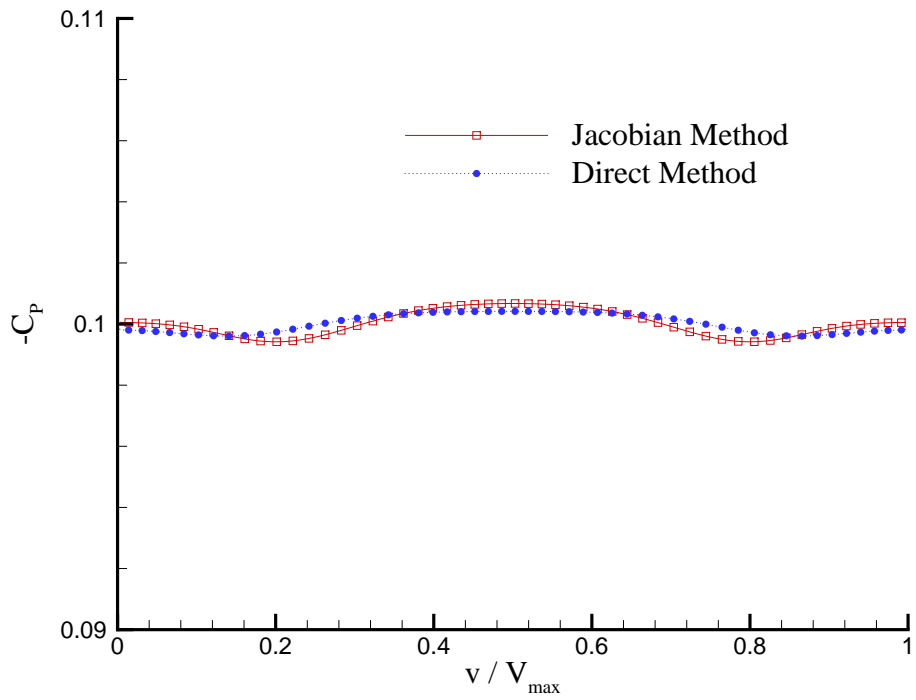
Figure 3.9: Comparison of pressures on the predicted tip vortex cavity by direct and Jacobian methods: $MC = 160$, Γ=0.4383(m^2/sec), σ=0.1 and α_{up}=4°.

99

3.3   3-D Hydrofoil Problem

A 3-D boundary element technique which is applied to determine the details of developed tip vortex cavity, is addressed in this section. Even though sheet cavity (partial or super cavity) is important, and often appears together with tip vortex cavity on hydrofoil, only a numerical scheme for determining the shape of tip vortex cavity is given in this section. Details of numerical implementation for the partial or/and super cavity shapes are given in Section 3.4.

3.3.1   Formulation

The coordinates system which is used to formulate hydrofoil and tip vortex cavity is the same as shown in Fig. 2.9. The tip vortex cavity is initially assumed to be a solid circular cylinder, and to be attached to the end of the foil tip. Consequently, the applied Green's formula is derived (same as Eqn. 2.15);

$$
\begin{aligned}
2\pi \phi_p \;=\;& \iint_{S_H \cup S_T} \left[\phi_q \frac{\partial G(p;q)}{\partial n_q} - \frac{\partial \phi_q}{\partial n_q} G(p;q) \right] dS \\
+\;& \iint_{S_w} \Delta \phi_w(y_q) \frac{\partial G(p;q)}{\partial n_q} dS
\end{aligned}
\tag{3.33}
$$

The perturbation potentials on the foil and the tip vortex cavity surfaces are determined by applying the boundary conditions.

3.3.2   Boundary Conditions

- Kinematic Boundary Condition (KBC) on wetted body surface : the fluid flow is tangent to the wetted body surfaces.

$$
\frac{\partial \phi}{\partial n} = \vec{U}_\infty \cdot \vec{n}
\tag{3.34}
$$

100

where

$$\vec{U}_\infty = (U_\infty \cos \alpha, 0, U_\infty \sin \alpha) \tag{3.35}$$

- Dynamic Boundary Condition (DBC) on cavity surface : The pressure on tip vortex cavity surface is equal to the cavity pressure. For a given cavitation number, σ,

$$\sigma = \frac{P_o - P_c}{\frac{1}{2}\rho U_\infty^2} \tag{3.36}$$

the pressure coefficient on the exact tip vortex cavity surface has to satisfy the following relation.

$$\begin{aligned} -C_p &= -\frac{P - P_o}{\frac{1}{2}\rho U_\infty^2} \\ &= \sigma \end{aligned} \tag{3.37}$$

- Kutta condition : the flow velocity is finite at the foil trailing edge.

$$|\nabla \phi| \quad < \quad \infty \qquad \text{at the foil trailing edge} \tag{3.38}$$

3.3.3 Solution Method

In order to solve the Green's formula given by Eqn. 3.33, either dipole (ϕ) or source ($\frac{\partial \phi}{\partial n}$) strengths have to be prescribed on the foil and tip vortex cavity surface via the boundary conditions. Since the tip vortex cavity is assumed to be a solid body, the kinematic boundary condition can be applied on the tip vortex cavity surface. After the potential on the tip vortex cavity surface is evaluated by solving Eqn. 3.33, the exact tip vortex cavity shape is determined by satisfying the dynamic boundary condition. In order to compute the more accurate geometry of

the tip vortex cavity, the trailing wake sheet is first aligned before determining the tip vortex cavity shape, as described in Section 2.4. The tip vortex cavity radius is updated to accelerate the convergence of tip vortex cavity shape while aligning wake geometry as follows:

$$r_T = \frac{\Gamma}{2\pi U_\infty \sqrt{\sigma}} \tag{3.39}$$

The Jacobian method is used to determine the shape of the tip vortex cavity surface, as described in Section 3.4.6. The procedure of determining the shape of the tip vortex cavity is as follows:

- Solve Eqn. 3.33 for the perturbation potential on the foil and the tip vortex cavity surface.

- Align the trailing wake sheet until the wake shape is converged, as explained in Section 2.4.

- Compute the pressure on the tip vortex cavity, and set Jacobian matrix.

- Modify tip vortex cavity shape by applying Eqn. 3.28.

- Repeat solving Eqn. 3.33 and determining the tip vortex cavity shape, until the cavity shape change between two consecutive iterations is within a specified tolerance.

3.3.4 Numerical Results

- Elliptic hydrofoil

The method of predicting the tip vortex cavity shape is applied to an elliptic hydrofoil, and the dimension of hydrofoil is the same as that given in Section 2.4.2. An inflow angle of attack $\alpha = 7^o$, cavitation number of $\sigma = 1.15$ are used for the validation and convergence tests. Figure 3.10 shows a comparison of the predicted tip vortex cavity shape with that obtained from experiment. The photograph of the tip vortex cavity is taken from [Arndt et al. 1991]. Even if the quantitative comparison of tip vortex cavity radii between the predicted and observed are not performed, the predicted tip vortex cavity shape is qualitatively well compared with that of experiment.

The convergence of pressures with number of circumferential panels on the tip vortex cavity surface are shown in Fig. 3.11. The depicted pressures are computed at downstream location of $x/R = 2.43$. The pressure corresponding to the initial geometry is also depicted. The predicted pressures converges quickly with number of panels, even though they still vary somewhat along the circumference.

Fig. 3.12 shows the convergence of averaged tip vortex cavity radius with number of circumferential panels on tip vortex cavity. The averaged tip vortex cavity radii at each strip are computed as follows:

$$(r_T)_{mean} = \frac{v_{max}}{2\pi} \tag{3.40}$$

where v_{max} is the arclength of the tip vortex circumference. The predicted tip vortex cavity radii agree well with each other except for the case of 10 panels.

Figure 3.13 shows the geometry of elliptic hydrofoil and its aligned trailing wake for an inflow angle of attack of $\alpha = 10^o$, and the cavitation number $\sigma = 1.0$.

103
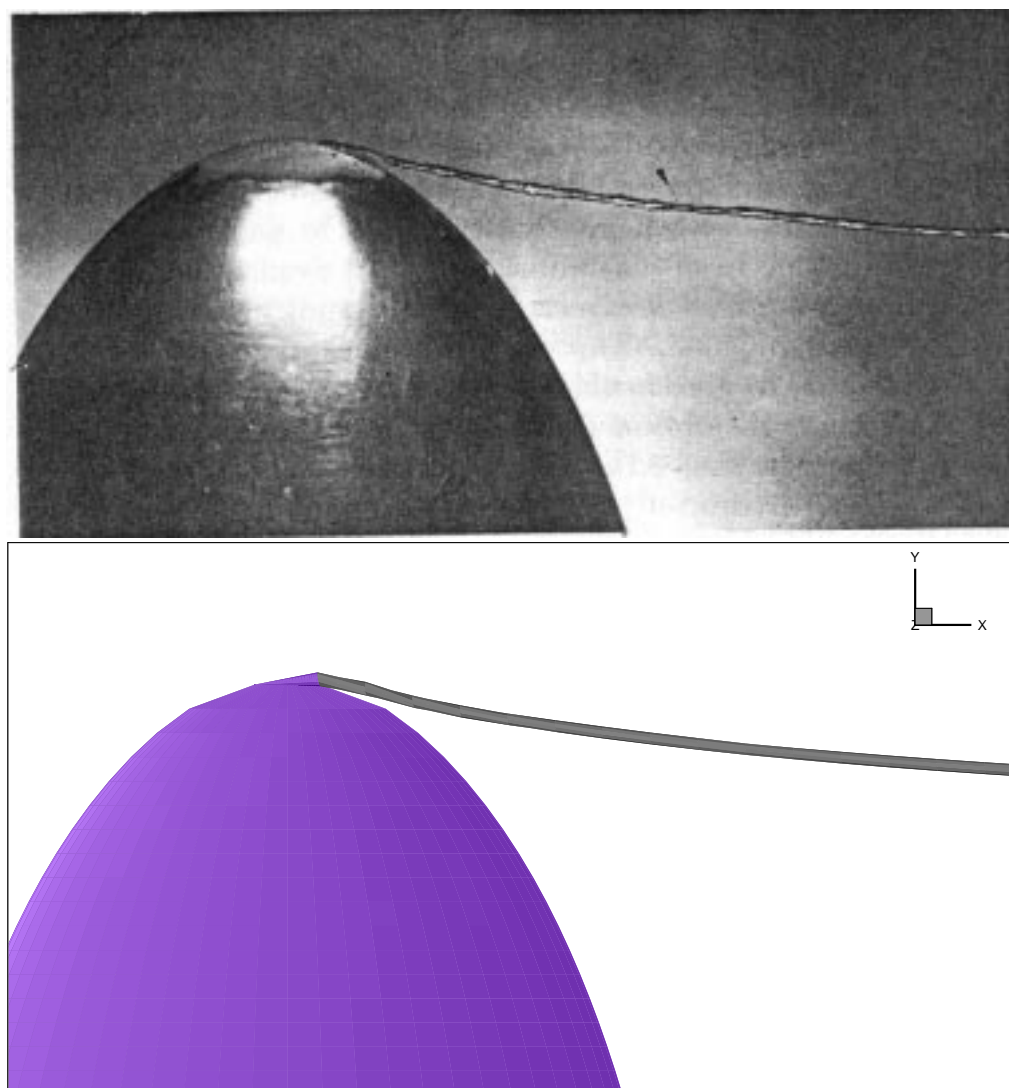
Figure 3.10: Comparison of the measured (top) [Arndt et al. 1991] and predicted (bottom) tip vortex cavity shapes: $AR = 3.0$, $t_{max}/C = 0.15$, $\sigma = 1.15$ and $\alpha = 7^o$.
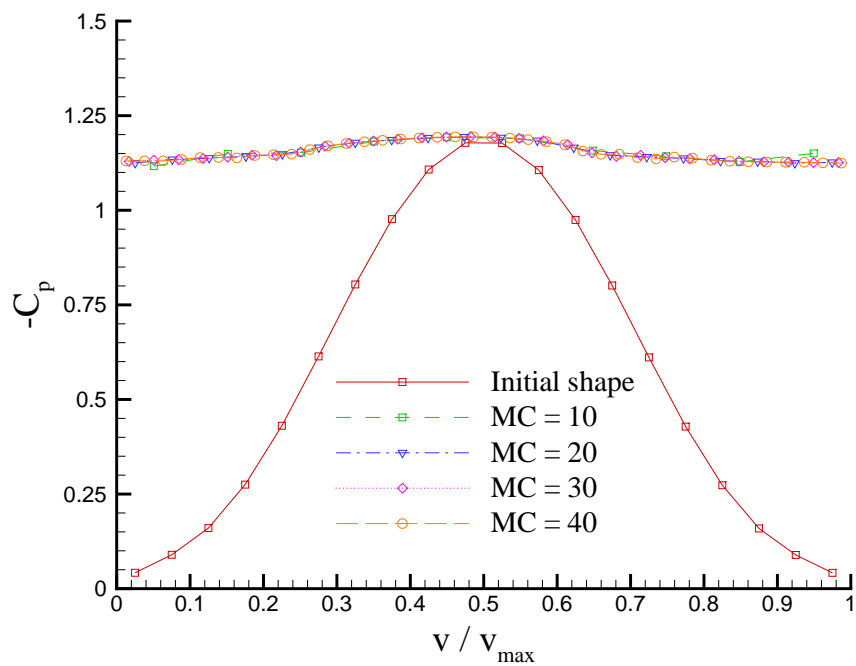
Figure 3.11: Convergence of pressure distributions on tip vortex cavity surface with number of circumferential panels at downstream location $x/R = 2.83$: $AR = 3.0$, $t_{max}/C = 0.15$, $\sigma = 1.15$ and $\alpha = 7^o$.
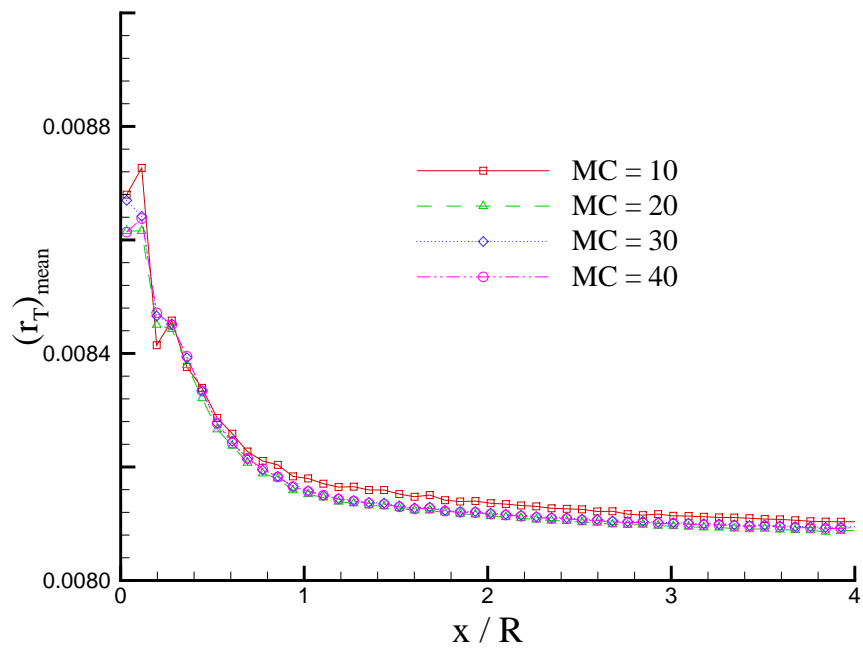
Figure 3.12: Convergences of tip vortex cavity radii with number of circumferential panels on tip vortex cavity surface: $AR = 3.0$, $t_{max}/C = 0.15$, $\sigma = 1.15$ and $\alpha = 7^o$.
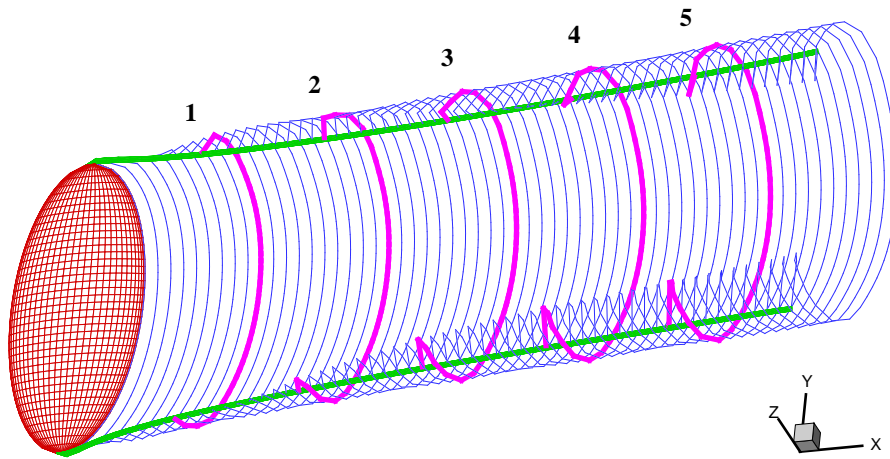
Figure 3.13: The converged wake geometries and an elliptic hydrofoil: $AR = 3.0$, $t_{max}/C = 0.15$, and $\alpha = 10^o$.

The predicted pressures along the circumferential direction on the tip vortex cavity surface are depicted in Fig. 3.14. The pressures are evaluated at the 5 downstream locations, as shown in Fig. 3.13 : $x/R = 1.17, \ 2.06, \ 2.84, \ 3.67$ and 4.51. Note the pressure difference between the initial and the converged cavity shapes. The pressure distributions on the converged tip vortex cavity are close to the cavitation number compared with those of the initial shape. As shown in 2-D vortex cavity problem, even though the tip vortex cavity shape is converged, the predicted pressure distributions are still varying along the circumferential direction. Since the velocities are evaluated by using central difference of potentials along the small radius of tip vortex core, the small change of the geometry produces the large change in velocity. In addition, the prediction of accurate tip vortex cavity shape in 3-D problem is more difficult than 2-D problem, since not as many panels as in the 2-D problem can be used, due to the limitation of computer memory.

Figure 3.15 shows the comparison of tip vortex cavity shapes in the case of $\alpha = 10^{o}$ and $\sigma = 0.2$. The initial cavity radius, $r_T = 0.036R$ is used, which is the same as that of the aligned wake. As shown in Fig. 3.16, the wake alignment helps the pressure distribution on tip vortex cavity to be close to the cavitation number. This is also consistent with the requirement of force-free wake.

The convergence of the tip vortex cavity shapes with number of circumferential panels is shown in Fig. 3.17. The depicted tip vortex cavity shapes are chosen at the location of $x/R = 2.41$. The tip vortex cavity shape shows very quick convergence with number of panels in this case.
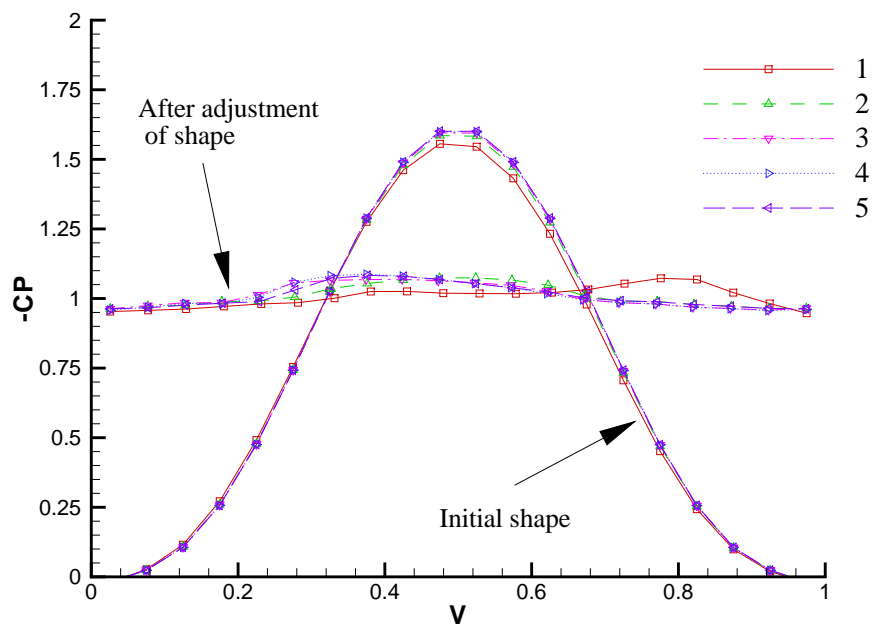
Figure 3.14: Pressure distributions on tip vortex cavity surface at the 5 locations downstream of the initial and the converged tip vortex cavity: $AR = 3.0$, $t_{max}/C = 0.15$, $\sigma = 1.0$ and $\alpha = 10^o$.

Solid line : Initial shape
Dashed line : After alignment
Dotted line : After adjustment of shape
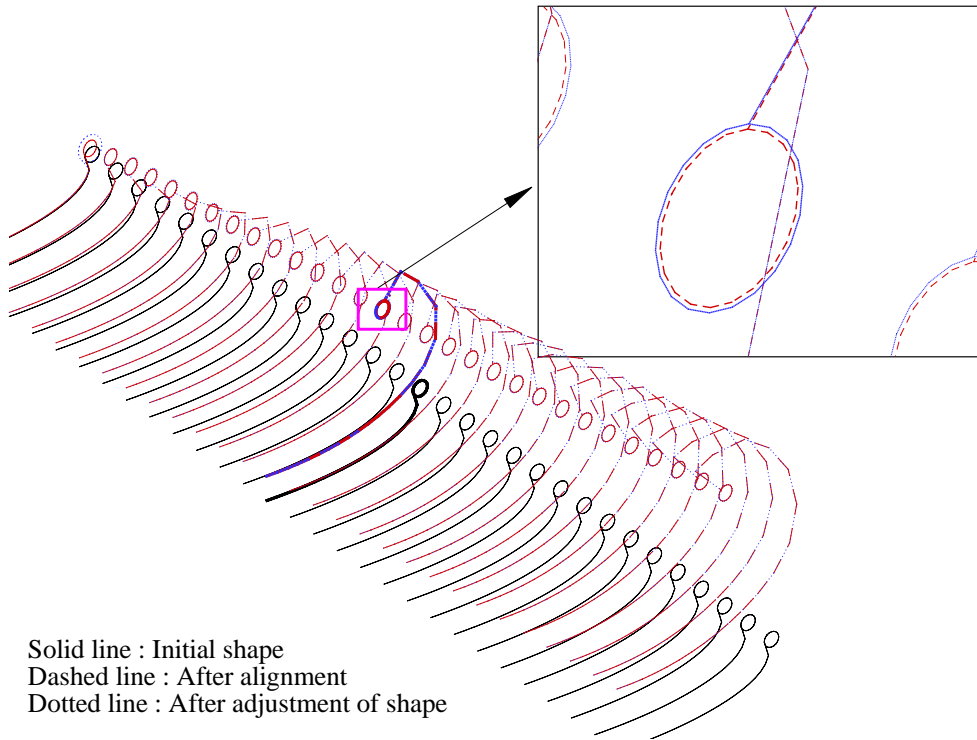
Figure 3.15: Comparison of tip vortex cavity shapes, the initial shape, after wake alignment and after adjustment of cavity shape: $AR = 3.0$, $t_{max}/C = 0.15$, $\sigma = 0.2$ and $\alpha = 10^o$.
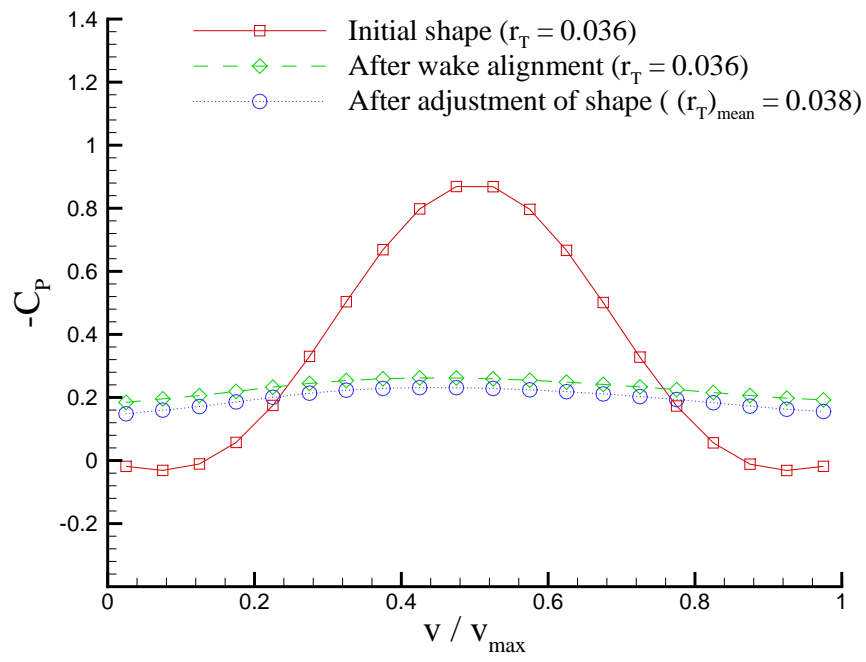
Figure 3.16: Comparison of pressure distribution on the initial shape, after wake alignment and after adjustment of cavity shape at $x/R = 2.41$: $AR = 3.0$, $t_{max}/C = 0.15$, $\sigma = 0.2$ and $\alpha = 10^o$.
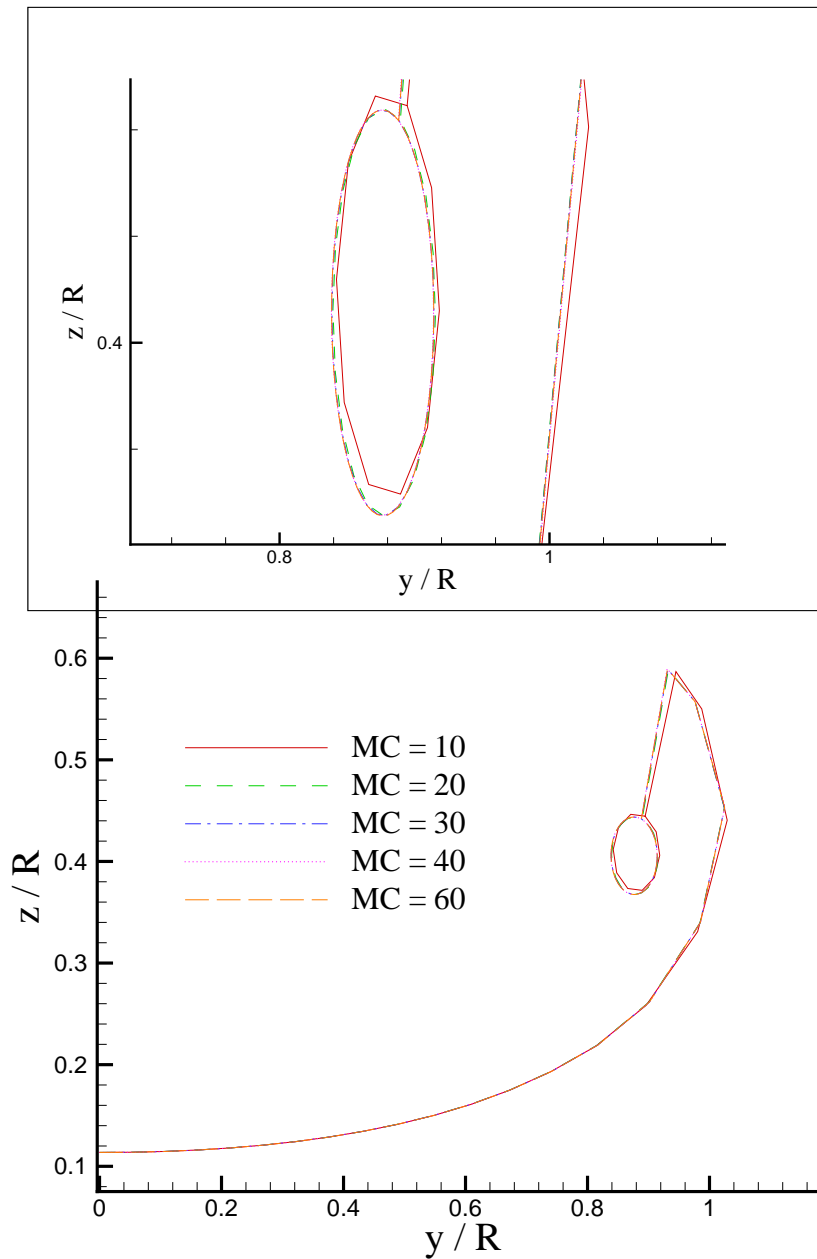
Figure 3.17: Convergence of tip vortex cavity shapes with number of panels in circumferential direction at $x/R = 2.41$: $AR = 3.0$, $t_{max}/C = 0.15$, $\sigma = 0.2$ and $\alpha = 10^o$.

3.4 Blade Sheet and Developed Tip Vortex Cavity on Propeller

In this section, the complete description of blade sheet and developed tip vortex cavity problem on marine propeller is provided. In order to model the blade sheet and developed tip vortex cavity on the marine propeller, Green's formula is applied on the physical problem and the boundary integral equation is derived. Also, the three dimensional nonlinear boundary conditions are applied to solve the derived boundary integral equation. Details of BEM applied on cavitating marine propeller are described in [Fine 1992a; Young 2002].

3.4.1 Assumptions

The propeller is rotating with a constant angular velocity in an unbounded domain, and is subject to non-uniform inflow. The inflow is considered as an *effective wake*, which includes the effects of the ship hull and the vorticity due to the propeller. The effective wake is assumed to be known, and provided by coupling of a lifting surface method and the unsteady Euler solver [Choi and Kinnas 2000, 2001].

Both partial and super cavities are allowed on face or/and back sides of propeller blades. The detachment line of the cavity leading edge is also assumed to be at arbitrary location on blade surface, and is determined to be satisfy the dynamic boundary condition. The pressure on cavity surface is assumed to be constant and be equal to the cavity pressure. Fluid behavior inside blade sheet and tip vortex cavity surface is not considered. The inception stage of tip vortex cavity is excluded in this work, therefore, tip vortex cavity is assumed to be fully developed and attached to

the tip of the blade. The vorticity of tip vortex cavity is assumed to be concentrated inside a tip vortex core. The flow outside the cavity is assumed to be irrotational and incompressible, and the fluid to be inviscid.

3.4.2 Formulation

As shown in Fig. 3.18, the cavitating propeller is subject to the non-uniform inflow, $\vec{U}_w(x_s, r_s, \theta_S)$, which is defined in the ship fixed coordinate system, (x_s, y_s, z_s). The propeller rotates with a constant angular velocity, $\vec{\omega}$, and is right handed looking from downstream. The solution is determined in the propeller fixed coordinates, which is represented as (x, y, z) in Fig. 3.18. The total inflow velocity relative to the propeller is

$$\vec{U}_{in}(x, y, z, t) = \vec{U}_w(x, r, \theta - \omega t) + \vec{\omega} \times \vec{x}(x, y, z) \tag{3.41}$$

where $r = \sqrt{(y^2 + z^2)}$, $\vec{x} = (x, y, z)$, and $\theta = \tan^{-1}(z/y)$. Since the fluid is assumed to be inviscid, and the flow to be irrotational and incompressible, the fluid domain can be represented by using the time-dependent perturbation potential, $\phi(x, y, z, t)$, defined as follows:

$$\vec{q}(x, y, z, t) = \vec{U}_{in}(x, y, z, t) + \nabla \phi(x, y, z, t) \tag{3.42}$$

where $\vec{q}(x, y, z, t)$ is the time-dependent total flow velocity.

The perturbation potential $\phi(x, y, z, t)$ defined in Eqn. 3.42 has to satisfy Laplace's equation, $\nabla^2 \phi = 0$. Thus, the potential ϕ at arbitrary point, p, on the wetted and the cavity surfaces must satisfy the Green's third identity:

114

$$
\begin{aligned}
2\pi \phi_p(\vec{x}, t) &= \iint_{S_{WS}(t) \cup S_T(t) \cup S_C(t)} \left[\phi_q(\vec{x}, t) \frac{\partial G(p; q)}{\partial n_q(t)} - \frac{\partial \phi_q(\vec{x}, t)}{\partial n_q(t)} G(p; q) \right] dS \\
&+ \iint_{S_w} \Delta \phi_w(r_q, \theta_q, t) \frac{\partial G(p; q)}{\partial n_q(t)} dS \qquad\qquad (3.43)
\end{aligned}
$$

where $G(p; q) = 1/R(p; q)$ is the infinite domain Green's function, and $R(p; q)$ is the distance between the field point p and the variable point q. $\vec{n}_q(t)$ is the unit normal vector to the surfaces of the propeller, hub, the cavity and the wake, and points into the fluid domain. $\Delta \phi_w$ is the potential jump across the wake surface S_w. S_{WS} represents fully wetted blade and hub surfaces. S_T and S_C denote tip vortex cavity and blade sheet cavity surfaces, respectively.

The Green's formula derived in Eqn. 3.43 implies that the potentials on the fluid domain can be represented by dipole and source distribution as follows:

- The potential on propeller blade, blade sheet and tip vortex cavity surfaces, $S_{WS}(t) \cup S_C(t) \cup S_T(t)$, is expressed as a linear superposition of the induced potentials by a continuous dipole and source distribution.

- The potential on the wake surface, $S_w(t)$ is expressed by a continuous dipole distribution.

The exact solution of Eqn. 3.43 can be uniquely determined when the boundary conditions are applied on the exact body and cavity boundaries.

115
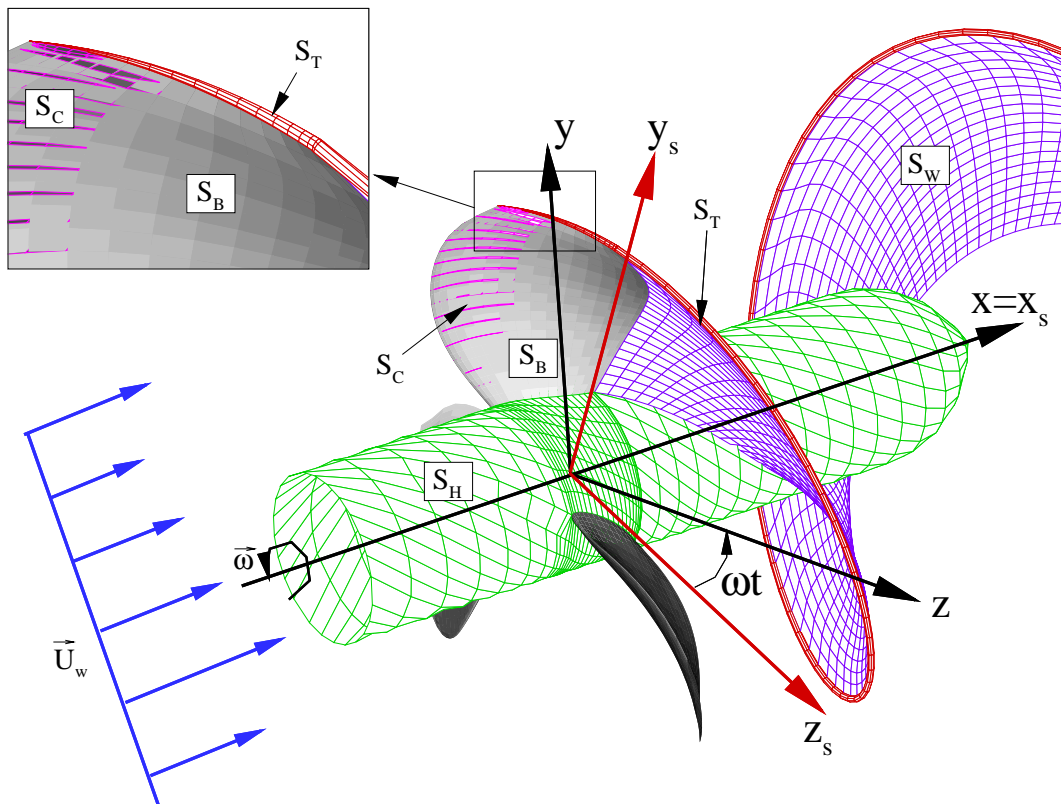
Figure 3.18: Propeller, hub, developed tip vortex cavity, and trailing wake geometries.

116

3.4.3 Boundary Conditions

- The fluid flow is tangent to the propeller blades, hub and exact cavity surfaces.

$$\frac{\partial \phi(x, y, z, t)}{\partial n} = -\vec{U}_{in}(x, y, z, t) \cdot \vec{n} \qquad (3.44)$$

- The blade sheet cavity has to be closed at the cavity trailing edge, i.e., the cavity thickness, δ should be zero at cavity end.

$$\delta(x, y, z, t) = 0 \qquad (3.45)$$

- Kutta condition : The velocity at the propeller trailing edge is finite.

$$|\nabla \phi| < \infty \qquad (3.46)$$

- The Dynamic Boundary Condition (DBC) on cavity surface : The pressure inside or on the cavity surface is constant and equal to the cavitating pressure P_c. The dynamic boundary condition is obtained from the unsteady Bernoulli's equation defined in the propeller fixed coordinates system as follows:

$$\frac{P_o}{\rho} + \frac{1}{2}|\vec{U}_w|^2 = \frac{\partial \phi}{\partial t} + \frac{P_c}{\rho} + \frac{1}{2}|\vec{q}_t|^2 - \frac{1}{2}\omega^2 r^2 + g y_d \qquad (3.47)$$

where ρ is the fluid density, r is the distance from the axis of rotation and $\vec{q}_t$ is the total velocity on the cavity surface. P_o is the pressure far upstream on the shaft axis. Also, g is the gravitational constant and y_d is the vertical distance from the axis of rotation. y_d is defined to be negative in the gravitational direction. By defining the cavitation number, σ_n,

$$\sigma_n = \frac{P_o - P_c}{\frac{1}{2}\rho n^2 D^2} \qquad (3.48)$$

117

and applying to the Bernoulli's equation of Eqn. 3.47, the magnitude of the total velocity on the cavity surface is derived as follows:

$$|\vec{q_t}| = \sqrt{n^2 D^2 \sigma_n + |\vec{U}_w|^2 + \omega^2 r^2 + 2g y_d - 2\frac{\partial \phi}{\partial t}} \qquad (3.49)$$

where $n = \frac{\omega}{2\pi}$ is the propeller revolution per unit time, and D is the propeller diameter.

- The Kinematic Boundary Condition (KBC) on blade sheet cavity surface: The normal velocities of the fluid and of the boundary must be equal. Consider a local coordinates system, (s, v, n), which is a non-orthogonal curvilinear coordinate as shown in Fig. 3.19. The cavity height of any points on the blade surface is defined by a function $n = h(s, v, t)$. Therefore, the exact kinematic boundary condition can be derived by requiring that the substantial derivative of a function $n - h$ vanishes on the cavity surface. The KBC implies that on $n = h$,

$$\frac{D}{Dt}(n - h) = \frac{\partial}{\partial t}(n - h) + \vec{q_t}(x, y, z, t) \cdot \nabla(n - h) = 0 \qquad (3.50)$$

The solution of Eqn. 3.43 can be uniquely determined by applying the above boundary conditions on the exact body boundaries. However, the difficulty in solving the above Green's formula is that it may not be solved directly by applying the boundary conditions since the exact cavity surface is unknown. Therefore, the solution of Green's formula has to be determined in an iterative manner, until the boundary conditions are satisfied on the updated cavity surface. In [Fine 1992a],

118

he proposed a iterative method to determine the exact shape of blade sheet cavity. The Green's formula was solved to satisfy the dynamic boundary condition on an approximated cavity surface, and the cavity surface was updated by using the kinematic boundary condition. He considered that the solution to be converged when the cavity surfaces do not change between two consecutive iterations. In the present work, two different methods are used to determine the blade sheet cavity surface and the developed tip vortex cavity shape, respectively. Both methods are summarized below, and are described in more detail in the following sections.

- Blade sheet cavity:

  - The potentials on the cavity surfaces are evaluated using the dynamic boundary condition.

  - The cavity shape is determined using the kinematic boundary condition (Eqn. 3.50) after boundary value problem is solved.

- Developed tip vortex cavity:

  - The initial shape of the tip vortex cavity is assumed to be a solid cylinder with a circular cross section.

  - The cavity shape is adjusted to satisfy the dynamic boundary condition using a two point Newton-Raphson scheme.

3.4.4 Determination of Potential on the Blade Sheet Cavity Surface

In order to solve Green's formula (Eqn. 3.43), either the source or the dipole strength has to be prescribed on each boundary. Since the position of the exact sheet
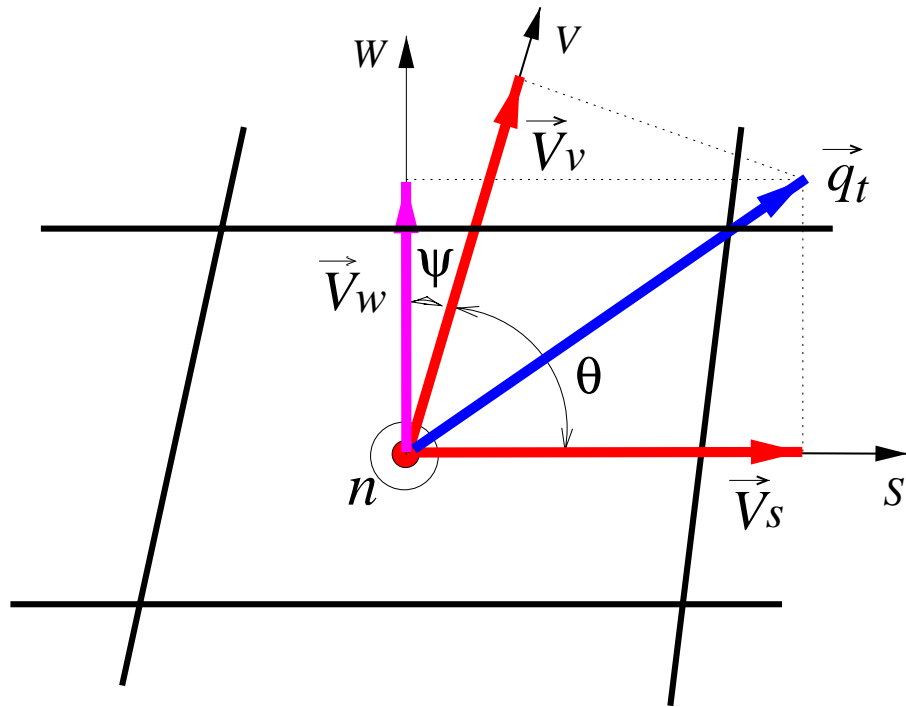
Figure 3.19: The definition of the total and local velocities on the local coordinates system, (s, v, n).

cavity surface is unknown, the source strength ($\frac{\partial \phi}{\partial n}$) in Eqn. 3.43 cannot be specified on cavity surface. Therefore, the perturbation potential which represents the dipole strength in Eqn. 3.43 has to be prescribed on the cavity surface to solve the system of equation. The potentials of the partial and super cavities are determined as follows:

- On the partial cavity surface

In addition to the expression for the magnitude of total velocity derived in Eqn. 3.49, the total velocity vector can be defined at each panel using the local

coordinates as shown in Fig. 3.19.

$$\vec{q}_t = \frac{\left(\frac{\partial \phi}{\partial s} + U_s\right)\left[\vec{s} - (\vec{s} \cdot \vec{v})\vec{v}\right] + \left(\frac{\partial \phi}{\partial v} + U_v\right)\left[\vec{v} - (\vec{s} \cdot \vec{v})\vec{s}\right]}{||\vec{s} \times \vec{v}||^2} + \left(\frac{\partial \phi}{\partial n} + U_n\right)\vec{n} \quad (3.51)$$

with $\vec{s}$ and $\vec{v}$ being the unit vectors corresponding to the coordinates s (chordwise) and v (spanwise), respectively, and with $\vec{n}$ being the unit normal vector to the cavity. Also, U_s, U_v and U_n are the inflow velocities, and V_s, V_v and V_n are the total velocities of (s, v, n) directions.

$$V_s = \frac{\partial \phi}{\partial s} + U_s = \frac{\partial \phi}{\partial s} + \vec{U}_{in} \cdot \vec{s}$$
$$V_v = \frac{\partial \phi}{\partial v} + U_v = \frac{\partial \phi}{\partial v} + \vec{U}_{in} \cdot \vec{v} \quad (3.52)$$
$$V_n = \frac{\partial \phi}{\partial n} + U_n = \frac{\partial \phi}{\partial n} + \vec{U}_{in} \cdot \vec{n}$$

By calculating the magnitude of total velocity from Eqn. 3.51 and combining with Eqn. 3.49, the quadratic equation is obtained in terms of the unknowns velocities, $\frac{\partial \phi}{\partial s}$ and $\frac{\partial \phi}{\partial v}$

$$\left(\frac{\partial \phi}{\partial s} + U_s\right)^2 - 2\left(\frac{\partial \phi}{\partial s} + U_s\right)\left(\frac{\partial \phi}{\partial v} + U_v\right)\cos\theta + \left(\frac{\partial \phi}{\partial v} + U_v\right)^2$$
$$- \sin^2\theta\left(n^2 D^2 \sigma_n + |\vec{U}_w|^2 + \omega^2 r^2 - 2gy_d - 2\frac{\partial \phi}{\partial t}\right) = 0 \quad (3.53)$$

Note that the total normal velocity term of $\left(\frac{\partial \phi}{\partial n} + U_n\right)$ is eliminated from Eqn. 3.53. If s, v, and n are located on the correct cavity surface, the flow has to be tangent to the cavity surface to satisfy the kinematic boundary condition, and consequently the total normal velocity would vanish on cavity surface. Even though the prescribed cavity surface is not the converged, leaving the normal velocity term out of the dynamic condition has a small effect on the solution [Fine 1992a]. By assuming that

121

the perturbation velocity along the $s-$direction is always positive, i.e., the flow does not reverse its direction, the quadratic equation can be solved for the perturbation velocity $\frac{\partial \phi}{\partial s}$ in terms of the unknown derivatives $\frac{\partial \phi}{\partial v}$ and $\frac{\partial \phi}{\partial t}$.

$$
\begin{aligned}
\frac{\partial \phi}{\partial s} &= -U_s + \left(\frac{\partial \phi}{\partial v} + U_v\right)\cos\theta + \\
&+ \sin\theta\sqrt{n^2 D^2 \sigma_n + |\vec{U}_w|^2 + \omega^2 r^2 - 2gy_d - 2\frac{\partial \phi}{\partial t} - (\frac{\partial \phi}{\partial v} + U_v)^2}
\end{aligned}
\tag{3.54}
$$

where θ is the angle between s and v, which is defined as $\cos\theta = \vec{s} \cdot \vec{v}$. The potential on the cavity surface is obtained by integrating the Eqn. 3.54 with respect to the arbitrary point s over the cavity surface.

$$
\begin{aligned}
\phi(s,v,t) = \phi(0,v,t) + \int_0^s & \left[-U_s + (\frac{\partial \phi}{\partial v} + U_v)\cos\theta + \right. \\
& \left. + \sin\theta\sqrt{n^2 D^2 \sigma_n + |\vec{U}_w|^2 + \omega^2 r^2 - 2gy_d - 2\frac{\partial \phi}{\partial t} - (\frac{\partial \phi}{\partial v} + U_v)^2} \right] ds
\end{aligned}
\tag{3.55}
$$

The time derivative term $\frac{\partial \phi}{\partial t}$ and the cross flow term $\frac{\partial \phi}{\partial v}$ are unknowns in Eqn. 3.55, and are determined in an iterative manner. The potential $\phi(0,v,t)$ corresponds to the potential at the cavity leading edge, and are determined by using third order polynomial approximation in terms of the unknown potentials on the wetted surface. The integral term of Eqn. 3.55 is determined by trapezoidal quadrature.

- On the supercavity surface

    Consider the orthogonal coordinates system (s,u,n), shown in Fig. 3.20. By assuming that the normal velocity is relatively small on wake surface, the total velocity vector, $\vec{V}^+$, on the local wake surface can be expressed as follows:

$$
\vec{V}^+ = V_s^+ \vec{s} + V_u^+ \vec{u}
\tag{3.56}
$$

122
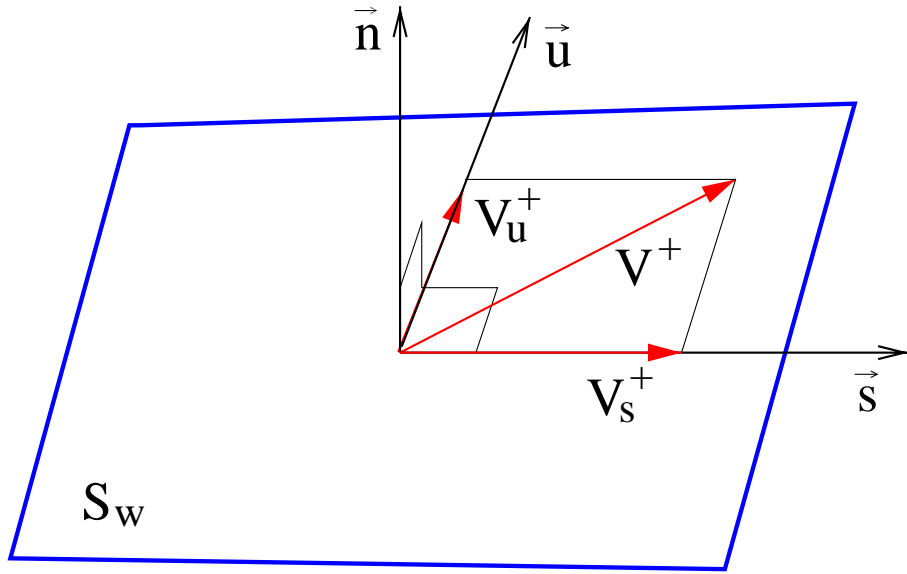
Figure 3.20: The definition of local velocities on the wake surface, (s, u, n).

where superscript $+$ represents the upper side of the wake sheet. Since the total velocity on local wake surface has to be equal to the total velocity of cavity on wake surface, the magnitude of the streamwise velocity is given by

$$V_s^+ = \sqrt{|\vec{q_t}|^2 - (V_u^+)^2} \tag{3.57}$$

By integrating Eqn. 3.57 with respect to s, and substituting Eqn. 3.49, the potential on the upper wake surface, ϕ^+ is determined:

$$
\begin{aligned}
\phi^+(s, u, t) &= \phi(s_o, v, t) + \int_{s_o}^{s} \Big[-U_s + \\
&+ \sqrt{n^2 D^2 \sigma_n + |\vec{U}_w|^2 + \omega^2 r^2 - 2gy_d - 2\frac{\partial \phi}{\partial t} - (V_u^+)^2} \Big] ds
\end{aligned}
\tag{3.58}
$$

where $s = s_o$ denotes the blade trailing edge. The cross flow term V_u^+ on the wake surface was found to be small, and neglecting that term from Eqn. 3.58 does not

123

affect the solution of Green formula. The integral of Eqn. 3.58 is also determined by using trapezoidal quadrature.

3.4.5 Determination of Blade Sheet Cavity Thickness

- Thickness of partial cavity

The cavity thickness of partial sheet cavity on the local coordinates is determined by substituting Eqn. 3.51 into Eqn. 3.50 [Fine 1992a].

$$\frac{\partial h}{\partial s}(V_s - V_v \cos\theta) + \frac{\partial h}{\partial v}(V_v - V_s \cos\theta) = \sin^2\theta(V_n - \frac{\partial h}{\partial t}) \tag{3.59}$$

The schematic diagram of velocities on the local coordinates, (V_s, V_v, V_n), which is defined in Eqn. 3.52 are shown in Fig. 3.19. The thickness of the partial cavity surface over the blade surface is determined by solving the partial differential equation (Eqn. 3.59). Once the system of equation is solved for the assumed cavity extents over the blade surface, the normal derivative of potential, $\frac{\partial\phi}{\partial n}$, becomes known value on the cavity surface. Since the normal derivative of total potential does not vanish on an assumed cavity surface, the cavity thickness can be updated by solving partial differential equation (Eqn. 3.59). The partial differential equation is solved using a two-point backward finite difference scheme, as shown in Fig. 3.21. The cavity thickness is accomplished by replacing the partial differential equation with a two-point backward difference formula along the $s-$ and $v-$ directions. The derivatives are defined at the control points and the cavity thickness is determined at the center

124
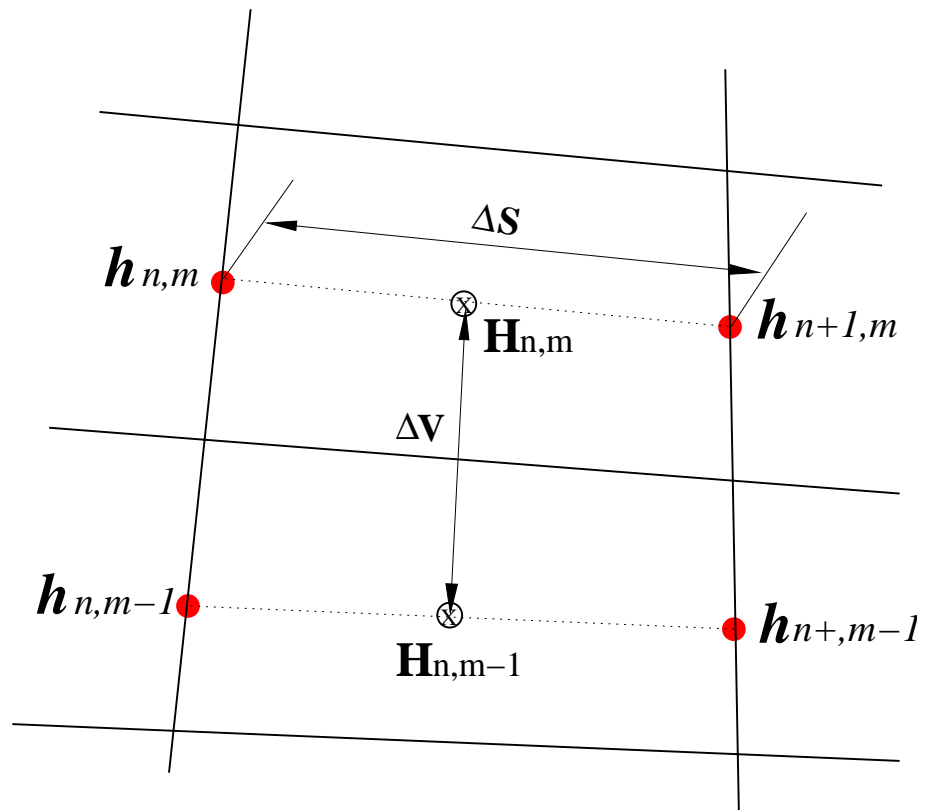
Figure 3.21: Numerical discretization for the cavity height calculation.

of the panel sides.

$$
\begin{aligned}
\frac{\partial h}{\partial s} &= \frac{h_{n+1,m} - h_{n,m}}{\Delta S} \\
\frac{\partial h}{\partial t} &= \frac{H_{n,m}^{t} - H_{n,m}^{t-1}}{\Delta t} \\
\frac{\partial h}{\partial v} &= \frac{H_{n,m} - H_{n,m-1}}{\Delta V}
\end{aligned}
\tag{3.60}
$$

with $H_{n,m} = \frac{h_{n,m} + h_{n-1,m}}{2}$, and the boundary condition that the cavity thickness at the cavity detachment location is equal to zero.

- Thickness of super cavity

The orthogonal coordinates, (s, u, n), is defined on wake surface, as shown in Fig. 3.20. Since the cross flow term on wake surface is very small compared to streamwise velocity, the cavity thickness on the wake surface can be derived from the kinematic boundary condition :

$$
q_w(t) - \frac{\partial h_w}{\partial t} = V_s^{+} \frac{\partial h_w}{\partial s}
\tag{3.61}
$$

where h_w is the cavity thickness of supercavity, and $q_w(t)$ is the wake source strength at time t. The wake source strength, q_w, is given by

$$
q_w(t) = \frac{\partial \phi_q^{+}}{\partial n_q}(t) - \frac{\partial \phi_q^{-}}{\partial n_q}(t)
\tag{3.62}
$$

where superscripts $+$ and $-$ represent the upper and lower surface of wake.

The total velocity (V_s^{+}) of cavity surface over wake sheet is determined to satisfy the dynamic boundary condition, and it is defined in Eqn. 3.47. Thus,

126
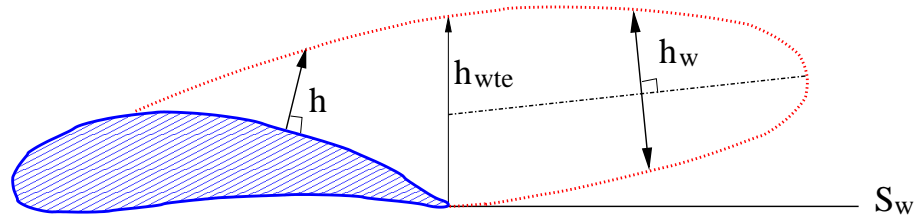
Figure 3.22: The definition of cavity thickness for the super cavity.

Eqn. 3.61 can be expressed as follows:

$$\frac{\partial h_w}{\partial s}\sqrt{n^2 D^2 \sigma_n + |\vec{U}_w|^2 + \omega^2 r^2 - 2gy_d - 2\frac{\partial \phi}{\partial t}} = q_w(t) - \frac{\partial h_w}{\partial t} \qquad (3.63)$$

Equation 3.63 also can be solved by using a two-point backward finite difference, and the unsteady term $\frac{\partial h_w}{\partial t}$ is updated from the previous values. The schematic for the cavity height on wake surface is shown in Fig. 3.22.

3.4.6 Determination of Tip Vortex Cavity Shape

In sections 3.2.3 and 3.2.4, two methods to determine the shape of tip vortex cavity, i.e., direct and Jacobian methods were described. In order to determine the tip vortex cavity shape using direct method, the potential on tip vortex cavity has to be evaluated from dynamic boundary condition. Since the cross flow velocity is small enough on the blade sheet cavity surface, that term can be neglected in Eqn. 3.55 and 3.58. However, both the tangential and streamwise velocities are important, and can not be neglected on tip vortex cavity surface. Therefore, the application of the direct method is not appropriate in 3-D tip vortex cavity problem due to the dominant effects of both tangential and streamwise velocities.

The Jacobian method is used to solve the 3-D tip vortex cavity shape prob-

127

lem. In this method, the shape of tip vortex cavity is assumed to be initially known, and the BVP is solved for the potentials on tip vortex cavity surface. The corrected tip vortex cavity shape is determined from the calculated pressure on tip vortex cavity to satisfy the dynamic boundary condition.

On the tip vortex cavity surface, the following equation has to be satisfied:

$$\delta p(h_t(s,v,t);\sigma_n) = -C_p - \sigma_n = 0 \tag{3.64}$$

where $h_t(s,v,t)$ is the increment of tip vortex cavity radius at the location (s,v) at time t (Fig. 3.23). The pressure coefficient, C_p, is defined as follows:

$$C_p = \frac{P - P_o}{\frac{\rho}{2}n^2 D^2} \tag{3.65}$$

P and P_o is the pressure on cavity surface and far upstream. Equation 3.64 implies that the pressure on the tip vortex cavity is equal to a given cavitation number. The tip vortex cavity shape which satisfy Eqn. 3.64 will be solved in an iterative manner.

To find the correct cavity shape, the system of equation with M unknowns (if the circumferential number of panel is M) has to be solved, i.e.,

$$\delta p_m(h_{t1}, h_{t2}, ..., h_{tM}) = 0, \quad \text{where } m = 1, 2, ..., M \tag{3.66}$$

where δp_m is the pressure difference on the tip vortex cavity at the mth circumferential node point. Equation 3.66 can be solved iteratively by applying an M-dimensional Newton-Raphson scheme. The updated cavity heights for the $(k+1)^{th}$ iteration are given as follows:

$$[h_t]^{k+1} = [h_t]^k - [J]^{-1}[\delta p]^k \tag{3.67}$$

128
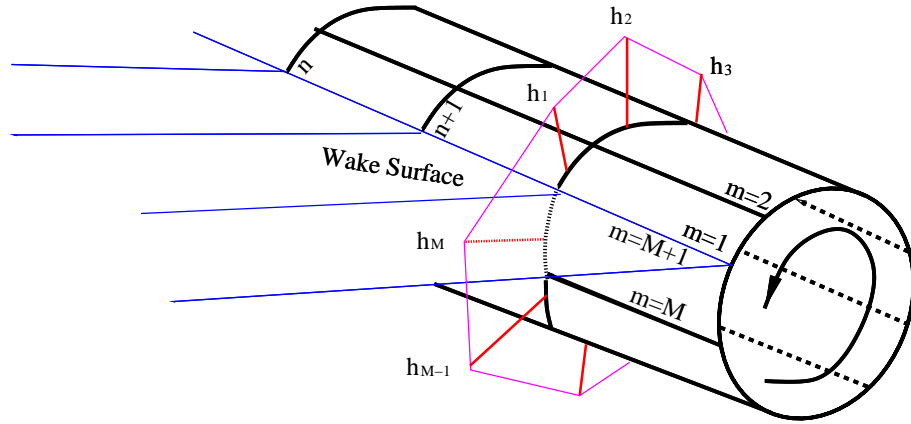
Figure 3.23: The definition of cavity height on tip vortex cavity surface.

where

$$
\begin{aligned}
[h_t]^T &= [h_{t1}, h_{t2}, ..., h_{tM}] \\
[\delta p]^T &= [\delta p_1, \delta p_2, ..., \delta p_M]
\end{aligned}
\tag{3.68}
$$

and $[J]$ is the Jacobian, which is defined as

$$
J_{ij} = \frac{\partial \delta p_i}{\partial h_j}, \qquad 1 \le i, j \le M
\tag{3.69}
$$

Each element of the Jacobian can be evaluated by using a two-point finite difference scheme. In order to accelerate the Newton-Raphson scheme, the off-diagonal terms of the Jacobian are ignored in solving Eqn. 3.67. Thus, this method requires only a single solution of the system of equations for each Newton-Raphson iteration.

3.4.7   Iterative Pressure Kutta (IPK) Condition

Details of the iterative pressure Kutta condition for the fully wetted propeller problems are described in [Kinnas and Hsin 1992]. However, they are summarized

129

here for completeness.

- Fully wetted problem

Consider the fully wetted propeller problem which does not include any forms of sheet cavities. Green's formula for the perturbation potential on the blades and wake surface is discretized as follows:

$$[A][\phi] = [RHS] - [\Gamma][W] \tag{3.70}$$

where $[A]$ is the matrix of the induced influence coefficients due to a constant dipole distribution, $[RHS]$ is the matrix for the induced potential by a constant source distribution and $[W]$ is the matrix for the influence coefficients at the blades field points due to the dipole of wake sheets.

Kutta condition implies that the velocity at the blade trailing edge is finite. We will satisfy Kutta condition by requiring that the pressure at the upper and lower control points of blade trailing edge be equal.

$$\Delta p_m = p_m^u - p_m^l = 0 \quad for \ m \ = \ 1, ..., M_R \tag{3.71}$$

where M_R is the total number of radial direction panels on the blade and superscript u and l mean upper(suction) side and lower(pressure) side of the blade, respectively.

Due to the nonlinear dependence of Δp on ϕ, an iterative method should be used to solve the system equation (Eqn. 3.70 and 3.71) with respect to the unknown

$[\phi]$ and $[\Gamma]$. In order to determine the circulation Γ_m at the strip m, the following Newton-Raphson scheme is used.

$$[\Gamma]^{(k+1)} = [\Gamma]^{(k)} - [J^{(k)}]^{-1}[\Delta p]^{(k)} \tag{3.72}$$

Eqn. 3.70 at the $k-$th iteration step becomes

$$[A][\phi]^{(k)} = [RHS] - [\Gamma]^{(k)}[W] \tag{3.73}$$

and the Jacobian matrix is defined as

$$J_{i,j}^{(k)} = \frac{\partial \Delta p_i^{(k)}}{\partial \Gamma_j^{(k)}} \tag{3.74}$$

The solution ϕ and Γ at the first iteration step ($k = 0$) are determined by applying the Morino's Kutta condition, i.e.

$$[A][\phi]^{(0)} = [RHS] - [\Gamma]^{(0)}[W] \tag{3.75}$$
$$\Gamma_m = \phi_m^u - \phi_m^l \ , \quad m = 1, ..., M_R$$

Because the Jacobian values of Eqn. 3.74 do not change rapidly, these values are kept same during the iteration.

The new Jacobian matrix is defined as follows:

$$J_{i,j}^{(k)} = J_{i,j} = \frac{\partial \Delta p_i}{\partial \Gamma_j} = \frac{\Delta p_i^\beta - \Delta p_i^0}{\Gamma_i^\beta - \Gamma_i^0} \tag{3.76}$$

131

where the superscript, 0, corresponds to the solution of Eqn. 3.75, and the superscript, β, corresponds to the solution at the $(1 + \beta)$ iteration step which is defined as follows;

$$\Gamma_j^\beta = (1 + \beta)\Gamma_j^0 \qquad (3.77)$$

where β is a small number. (Usually we use $\beta = 0.01$.)

The modified Newton-Raphson scheme with the Jacobian matrix equation (3.76) becomes

$$[\Gamma]^{(k+1)} = [\Gamma]^{(k)} - [J]^{-1}[\Delta p]^{(k)} \qquad (3.78)$$

The solution satisfying the pressure Kutta condition can be determined by iteratively solving the Eqns. 3.73 and 3.78. However, this method is too expensive for the unsteady problems since we have to solve simultaneous equation (Eqn. 3.73) not only for each time step but also for each iteration step.

We applied the technique of the base problems to avoid solving the Eqn. 3.73 at each time and iteration steps.

Because the matrix $[RHS]$ is identical in Eqns. 3.70 and 3.73 for each time step, we can obtain new equation by subtracting Eqn. 3.73 from Eqn. 3.70.

$$[A][[\phi]^{(k)} - [\phi]] = -[W][[\Gamma]^{(k)} - [\Gamma]] \qquad (3.79)$$

or

132

$$[A][\delta\phi] = -[W][\delta\Gamma] \qquad (3.80)$$

where

$$[\delta\phi] = [\phi]^{(k)} - [\phi] \;\; and \;\; [\delta\Gamma] = [\Gamma]^{(k)} - [\Gamma] \qquad (3.81)$$

Let's define *"base potentials"*, $[\Phi]^m$, which are the solutions to the base problems

$$[A][\Phi]^m = -[W][B]^m \;\;, \quad m \; = \; 1, ..., M_R \qquad (3.82)$$

where

$$[B]^m = [B_1 = 0, B_2 = 0, ..., B_m = 1, B_{m+1} = 0, ..., B_{M_R} = 0]^T \qquad (3.83)$$

The base potentials correspond to the potentials of the propeller blade when there is no inflow and the potential jumps are equal to zero in all wake panels except for the first panel in the wake at blade strip m, in which dipole distribution equal to "1" at the blade trailing edge and linearly becomes "0" at the panel right side. The important thing is that base potentials depend only on the discretization and that they are independence of the inflow as well as time step n. The solution of Eqn. 3.80 can be expressed by the linear superposition of base potentials.

$$[\delta\phi] = \sum_{m=1}^{M_R} \delta\Gamma_m [\Phi]^m \qquad (3.84)$$

By the definition of $[\delta\phi]$ and $[\delta\Gamma]$, the solution to the system equation is expressed as:

133

$$[\phi]^{(k)} = [\phi] + \sum_{m=1}^{M_R} (\Gamma_m^{(k)} - \Gamma_m)[\Phi]^m \qquad (3.85)$$

The base potential is determined by solving the Eqn. 3.82 before solving the unsteady problem. Then, the solution potential can be determined to satisfy the Kutta condition by iteratively solving the Eqns. 3.78 and 3.85 with solution of Eqn. 3.75.

- Cavity problem

In order to apply IPK condition on propeller problem, the system of equation has to be a same form as shown in Eqn. 3.70 so that the unknowns are only potentials. Since the potentials, ϕ, are unknown on wetted blade surface and the normal velocities, $\frac{\partial \phi}{\partial n}$, on the cavity surface, IPK condition cannot be directly applied on the cavity problem. In this work, the IPK was applied as a *post process* for the cavity problem. The process is given as follows:

1. Solve the cavity problem of Eqn. 2.24, and determine the correct cavity shape.

2. Set up $[A]$, $[RHS]$ and $[W]$ matrices as shown in Eqn. 3.70.

3. Evaluate the potentials on the correct cavity surface using Eqn. 3.55.

4. Solve base potentials of Eqn. 3.82.

5. Modify the potentials on cavity and blade surfaces using Eqn. 3.78 and 3.85.

- Application of IPK on cavitating propeller

134
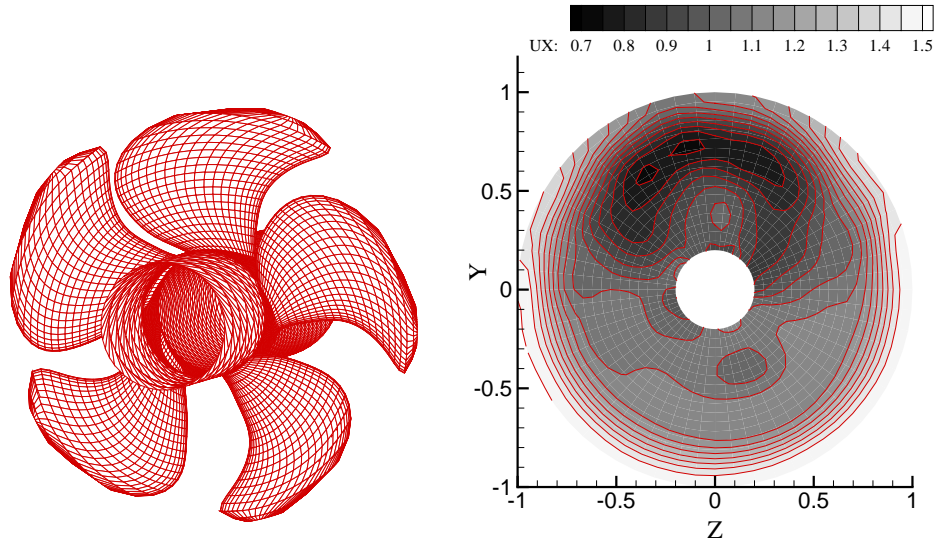
Figure 3.24: Geometry and inflow wake of DTMB P5168 propeller.

To validate the treatment of IPK condition on cavitating propeller, the predicted forces and pressures are compared with those obtained without IPK condition for DTMB P5168 propeller [Chesnakas and Jessup 1998]. The geometry and non-axisymmetric inflow wake of DTMB P5168 propeller is shown in Fig. 3.24. The test conditions are selected to generate partial cavitation on propeller blade, which values are $J_s = 1.0$ and $\sigma_n = 2.1$. Morino condition is applied in the case of without IPK, in which the potential jump at the blade trailing edge is given by

$$\Delta\phi = \phi^+ - \phi^- \tag{3.86}$$

where superscript $+$ and $-$ denote back and face sides of blade.

Comparisons of pressure distributions with and without IPK at key blade angle, $\theta = 0^o$, are shown in Fig. 3.25. The pressures are predicted along blade
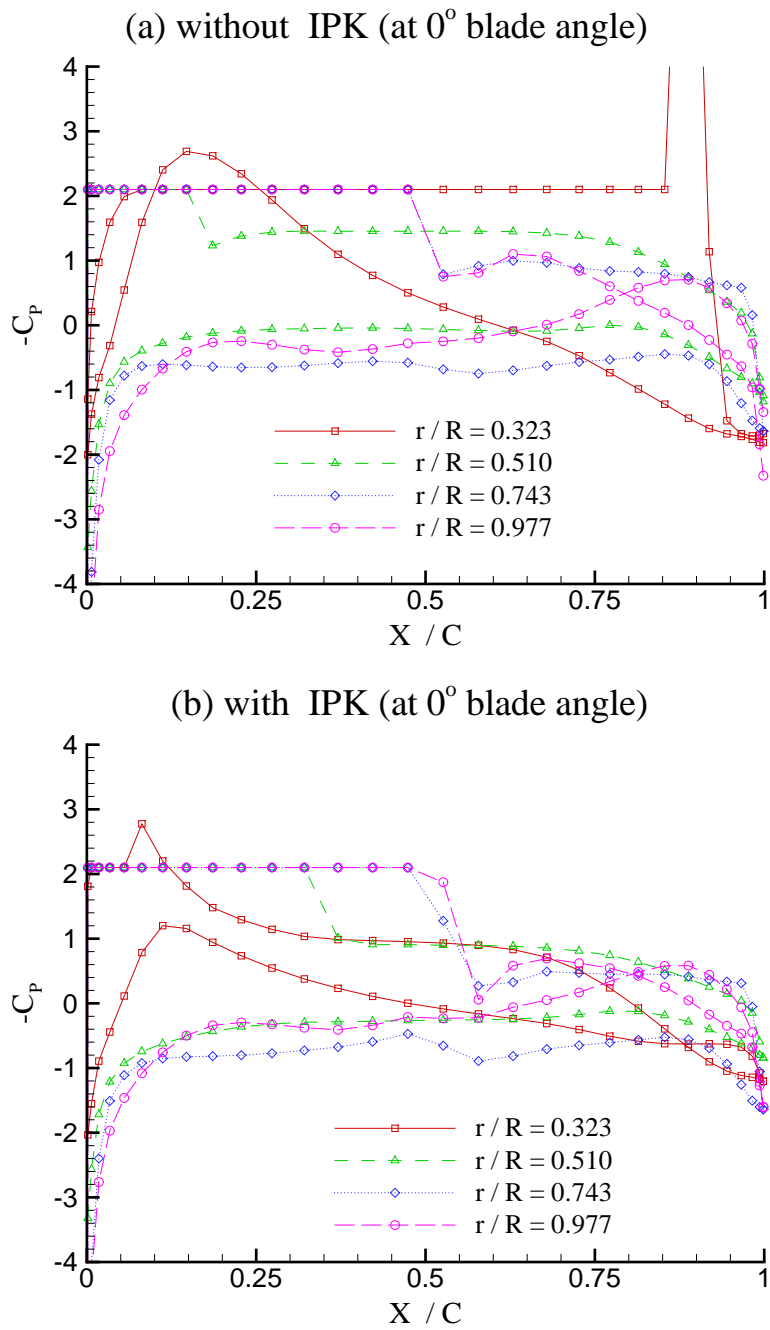
Figure 3.25: Comparisons of pressure distributions between (a) without IPK and (b) with IPK at 0° key blade angle for DTMB P5168 propeller: $J_s = 1.0$, and $\sigma_n = 2.1$.

chordwise direction at four non-dimensionalized radii, $r/R = 0.323, 0.51, 0.743$ and 0.977.

Without applying IPK, the predicted pressures at the trailing edge of face and back sides do not match each other. Especially, the pressures without IPK are over-predicted at $r/R = 0.323$ and result in supercavitation. The results of with IPK show good agreement of pressures at the trailing edge of blade face and back sides.

The unsteady cavitating forces predicted by using IPK and without IPK are shown in Fig. 3.26. The predicted thrust and torque coefficients show some discrepancy between both IPK conditions. The averaged differences of thrust and torque coefficients between these with and without IPK conditions are 4.4% and 5.0%, respectively.

3.4.8   Numerical Results

The sensitivity of the solution to the number of panels, time step size, and the number of propeller revolutions are presented in this section.

DTMB N4148 propeller

The method is applied to determine the blade sheet and developed tip vortex cavities on DTMB N4148 propeller. The geometry of DTMB N4148 propeller and the non-axisymmetric inflow are the same as those shown in Fig. 2.29. The flow conditions are given as follows: $J_s = 0.9087$, $F_n = 9.159$, and $\sigma_n = 2.576$. The effective wake used in this computation includes the effects of the tunnel walls and

137
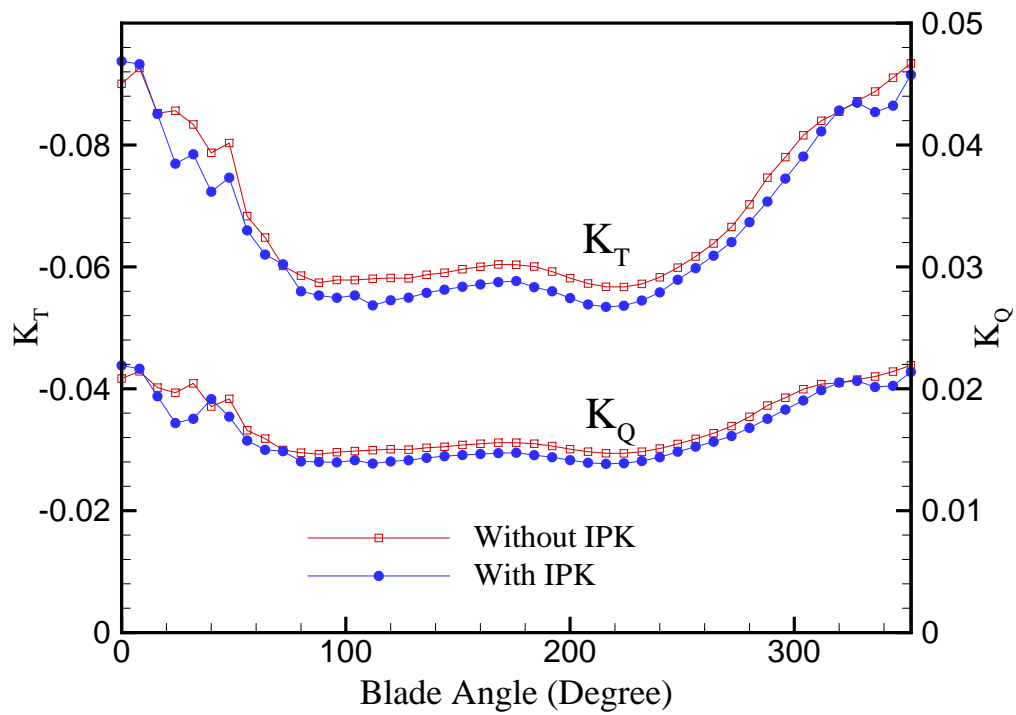
Figure 3.26: Comparisons of unsteady cavitating forces between with/without IPK for DTMB P5168 propeller: $J_s = 1.0$, and $\sigma_n = 2.1$.

vortical inflow/propeller interactions, which is taken into account using WAKEFF-3D [Choi and Kinnas 1998, 2000].

The predicted blade sheet and tip vortex cavities compared with these observed in the experiment and the computed by using MPUF-3A are shown in Fig. 3.27. MPUF-3A is using a vortex lattice method, in which the vortex and source lattices are placed on the mean camber surface. The observed blade angles are -30°, 6°, and 30°. As shown in the figure, the results of the present method agree relatively well with experimental observations rather than those of MPUF-3A. Even if the thickness-loading coupling [Kinnas 1992] is included in MPUF-3A, the details of flow near blade leading edge and tip cannot be captured using the vortex lattice method. Therefore, MPUF-3A predicts less blade sheet cavity than the present method. In addition, MPUF-3A is developed to predict only blade sheet cavity, and cannot capture tip vortex cavity. The comparison of the predicted tip vortex cavity shape (or radius) shows at least qualitative agreement to the observed, as shown in Fig. 3.27.

Figure 3.28 shows the convergence of unsteady cavitating forces per blade (thrust and torque coefficients) with number of panels on propeller blade. Except for the case of 40×20 panels, the predicted forces are not much sensitive to the mesh size.

The convergence of individual blade forces with time step size is shown in Fig. 3.29. The presented blade angle increments are 4°, 6° and 8°. The predicted blade forces are not very sensitive at least up to 8° blade angle increment. However, the larger time step size result in instabilities of the solution.
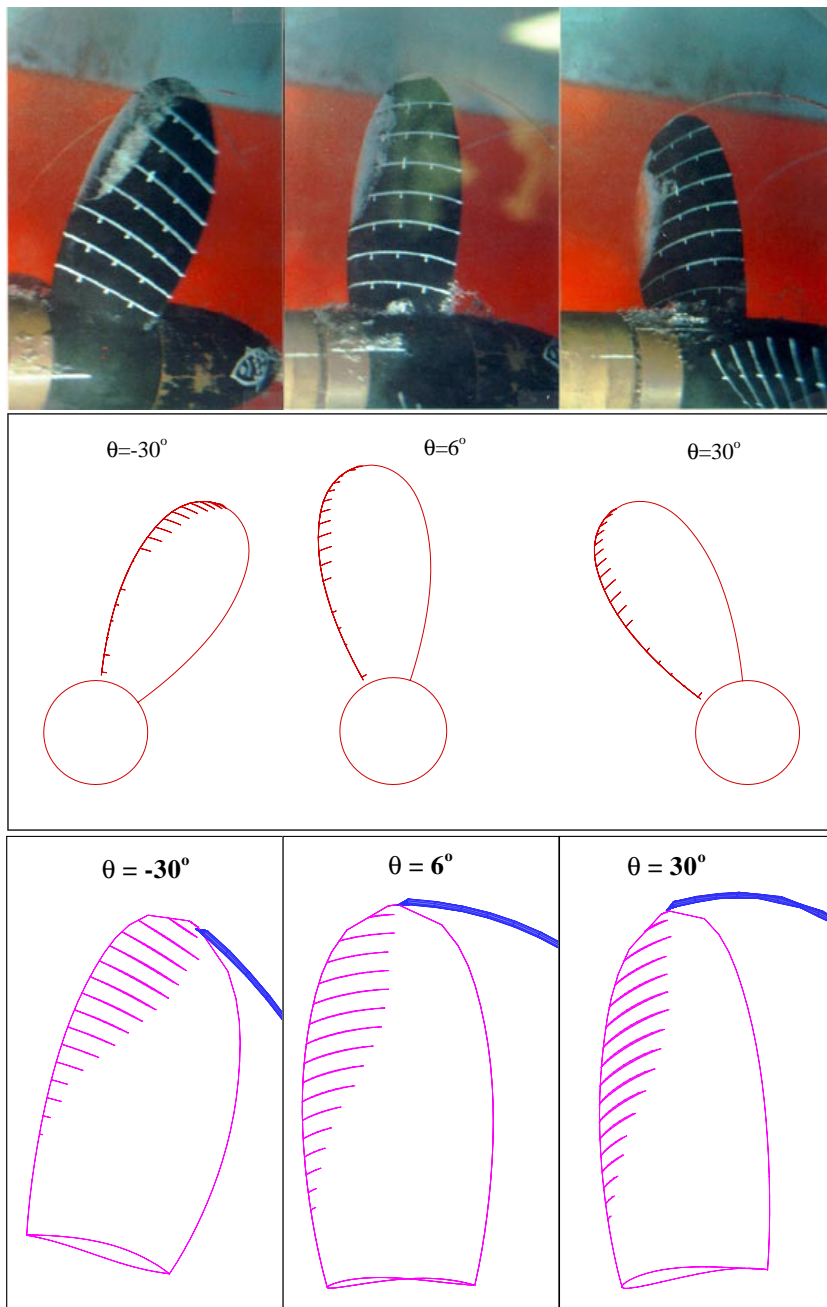
Figure 3.27: Comparison of blade sheet and tip vortex cavities predicted by present method (bottom) with the measured in the experiment (top) and the computed from MPUF-3A (middle) [Lee and Kinnas 2001b] for DTMB N4148 propeller: $J_s = 0.9087$, $F_n = 9.159$, and $\sigma_n = 2.576$.
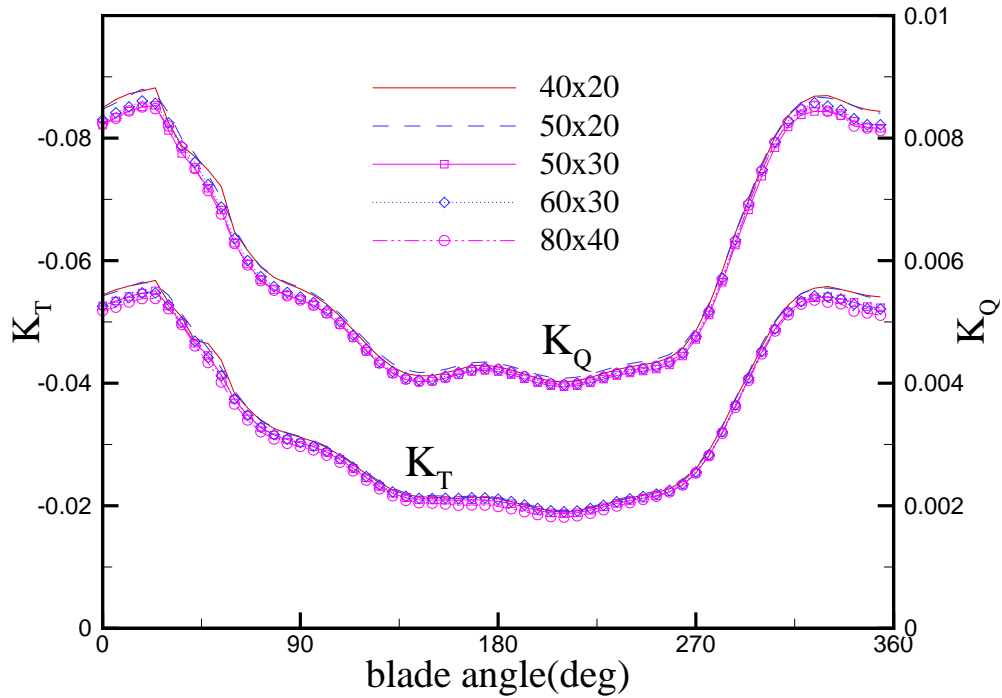
Figure 3.28: Convergence of unsteady cavitating forces per blade with number of panels for DTMB N4148 propeller: $J_s = 0.9087$, $F_n = 9.159$, and $\sigma_n = 2.576$.

Figures 3.30 and 3.31 show the dependence of cavity planforms on the panel discretization and time step size. As shown in the figures, the cavity planforms are not much sensitive to the number of panels and the time step size in this propeller case.

The convergence of propeller thrust coefficients with number of propeller rotations are shown in Fig. 3.32. With increasing revolutions, the predicted forces converge to that of the last (fifth) revolution. Since the unsteady term, $\frac{\partial \phi}{\partial t}$, is in-
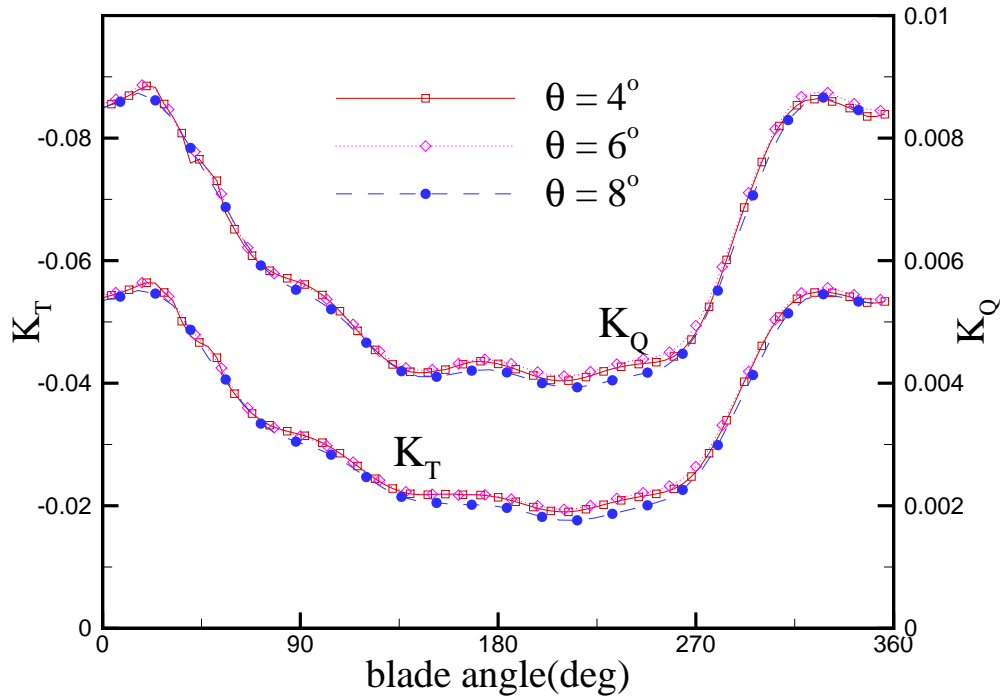
Figure 3.29: Convergence of unsteady cavitating forces per blade with time step sizes for DTMB N4148 propeller: $J_s = 0.9087$, $F_n = 9.159$, and $\sigma_n = 2.576$.

cluded after second revolution is completed, this results in the shown force shift between the second and the third revolution.

Figure 3.33 shows the convergence of cavity volume with number of revolutions. As shown in the figure, the predicted cavity volume shows very quick convergence as the number of propeller revolution increases.

The steady pressure distributions computed along the tip vortex cavity circumference are shown in Fig. 3.34. The axial location, x', is defined as $x' =$
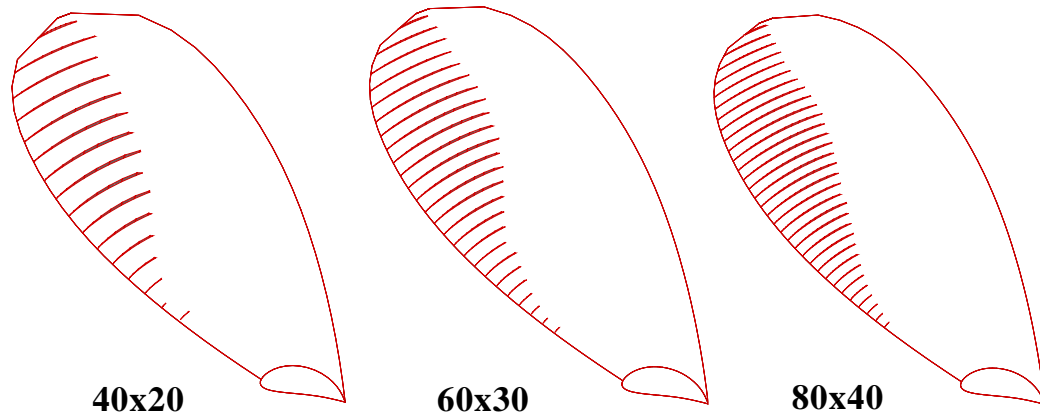
Figure 3.30: Convergence of blade sheet cavitation with number of panels at 30° blade angle for DTMB N4148 propeller: $J_s = 0.9087$, $F_n = 9.159$, and $\sigma_n = 2.576$.
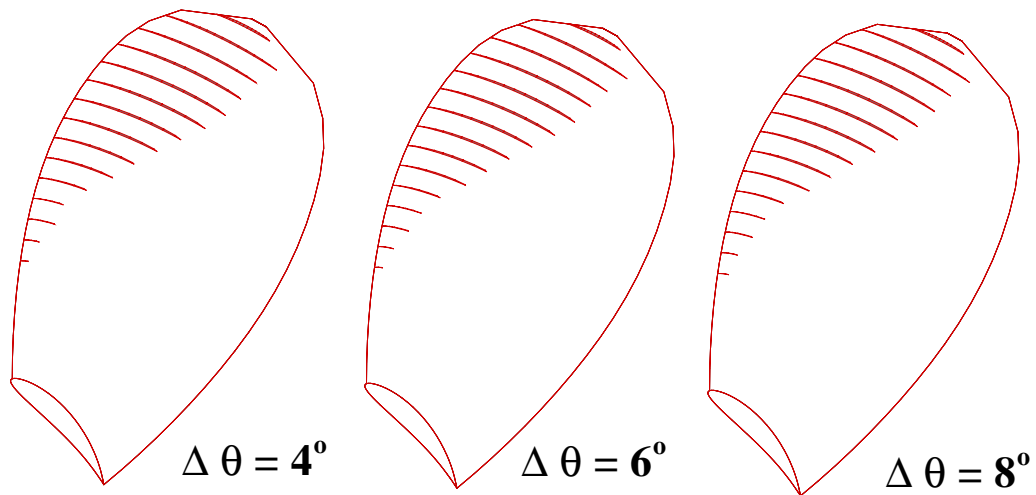
Figure 3.31: Convergence of blade sheet cavitation with time step sizes at 336° blade angle for DTMB N4148 propeller: $J_s = 0.9087$, $F_n = 9.159$, and $\sigma_n = 2.576$.
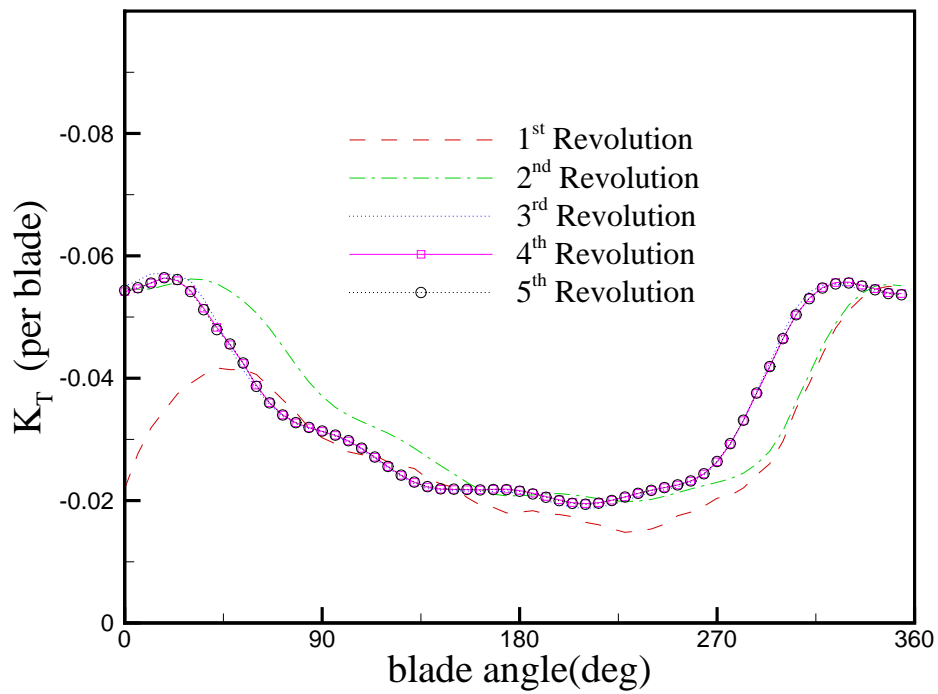
Figure 3.32: Convergence of unsteady cavitating forces per blade with number of propeller revolutions for DTMB N4148 propeller: $J_s = 0.9087$, $F_n = 9.159$, and $\sigma_n = 2.576$.
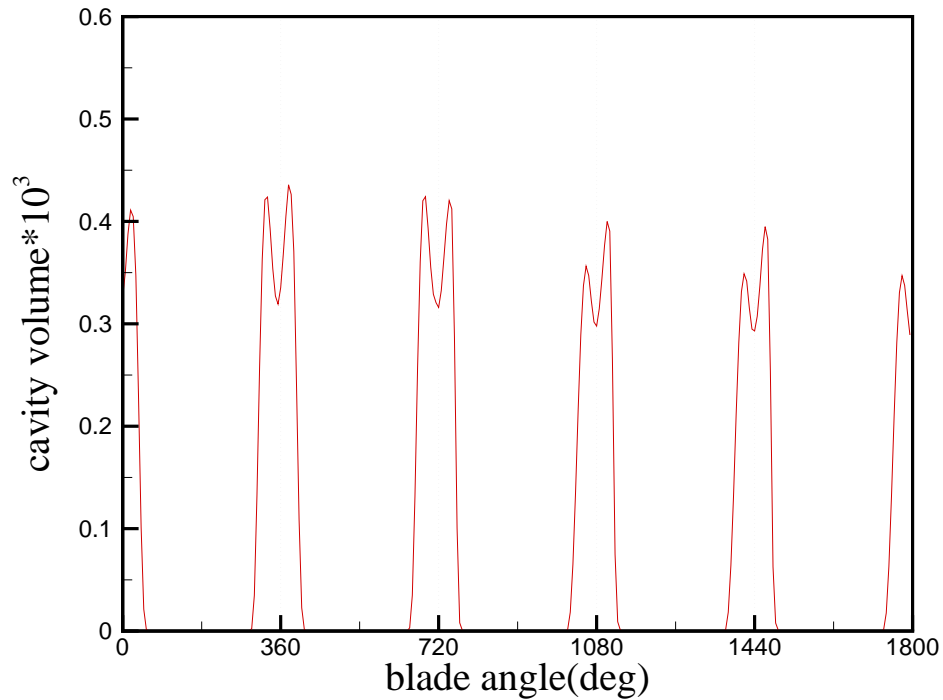
Figure 3.33: Convergence of cavity volumes with number of propeller revolutions for DTMB N4148 propeller: $J_s = 0.9087$, $F_n = 9.159$, and $\sigma_n = 2.576$.

$(x - x_{TE})/R$. x_{TE} is the x-coordinate of blade trailing edge at the tip, and R is a radius of propeller. The circumferential number of panels used for the pressure calculation is 10. Compared with the pressures after wake alignment, the pressures after the adjustment of the tip vortex cavity shape are close to the given cavitation number, $\sigma = 2.576$. In order to reduce the pressure deviation from the cavitation number on tip vortex cavity surface, even more panels are needed along the tip vortex circumference, as shown in the case of 2-D tip vortex cavity, described in Section 3.2.
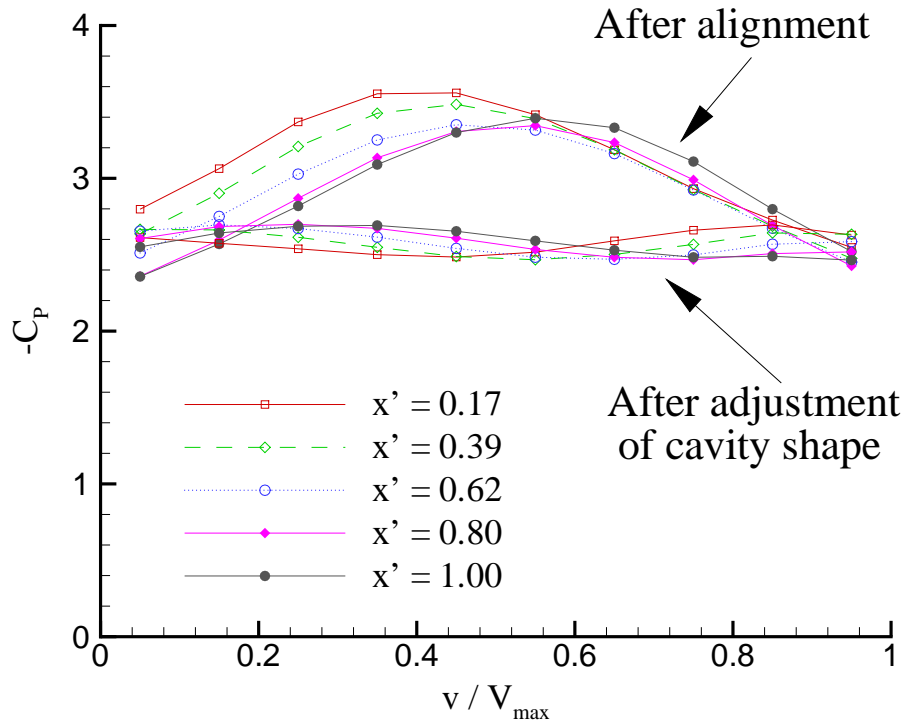
Figure 3.34: Comparisons of pressure distributions on developed tip vortex cavity before and after adjustment of cavity shape at 5 downstream locations for DTMB N4148 propeller: $J_s = 0.9087$, $F_n = 9.159$, and $\sigma_n = 2.576$.

The predicted unsteady pressures on the tip vortex cavity circumference at the different key blade angles are drawn in Fig. 3.35. The unsteady pressure predicted by the current method seems to be in reasonable agreement with the given cavitation number.

Figure 3.36 shows the pressure distribution computed along the x-direction at different key blade angles. The differences between the given cavitation number and the circumferentially averaged pressures at each blade angle are shown in

Fig. 3.37. Even though there are some pressure discrepancies as shown in Figs. 3.35 and 3.36, the averaged pressures are close to the given cavitation number, and the maximum pressure difference is about 1.5%.

(a) Key blade position : 0°

$\sigma = 2.576$

-C_P

v / V_{max}

x = 0.1864
x = 0.3822
x = 0.5850
x = 0.7908
x = 0.9993

(b) Key blade position : 88°

$\sigma = 2.576$

-C_P

v / V_{max}

x = 0.1863
x = 0.3847
x = 0.5886
x = 0.7913
x = 0.9994
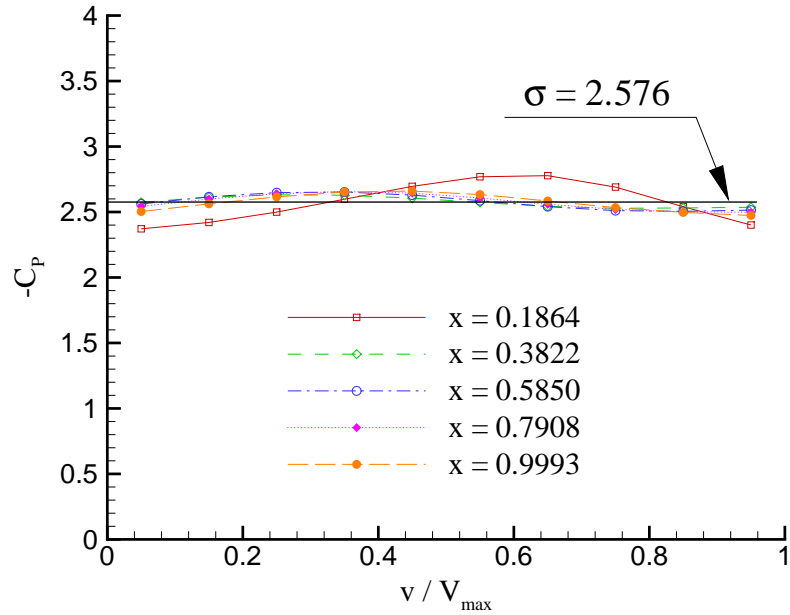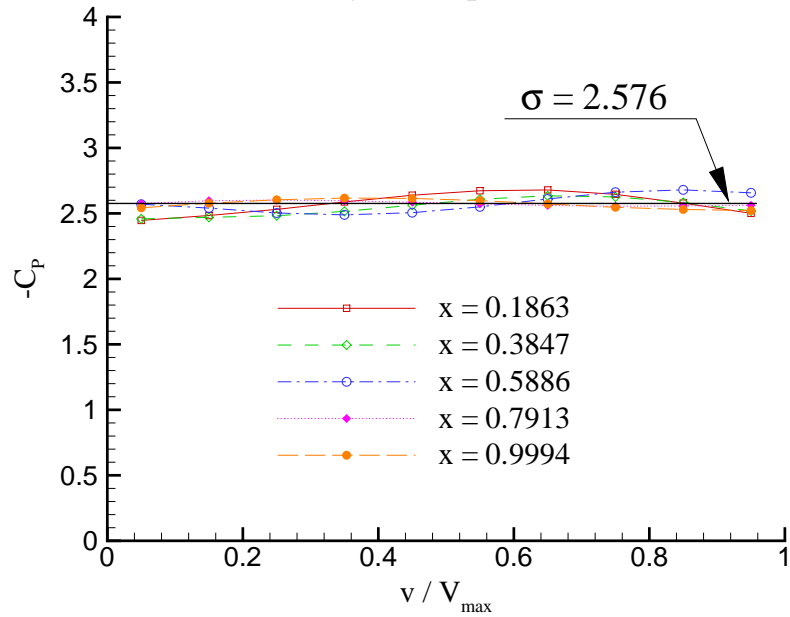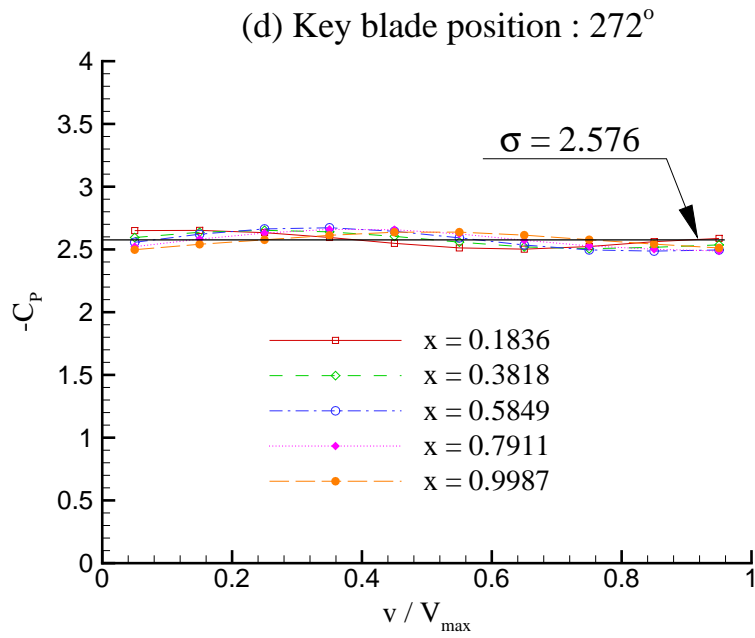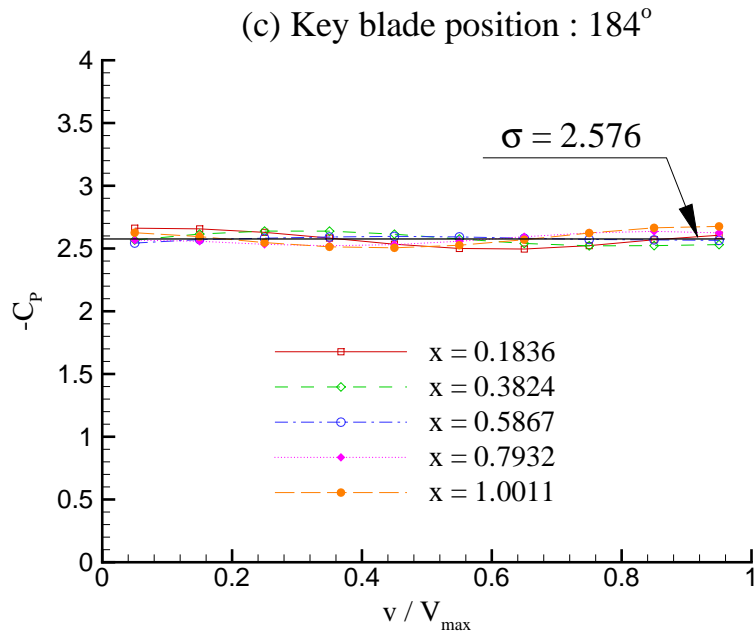
Figure 3.35: Circumferential pressure distributions on developed tip vortex cavity for DTMB N4148 propeller. The pressures are depicted at key blade positions of (a) $\theta = 0^o$, (b) $\theta = 88^o$, (c) $\theta = 184^o$, and (d) $\theta = 272^o$: $J_s = 0.9087$, $F_n = 9.159$, and $\sigma_n = 2.576$.

(a) Key blade angle : 0°

σ = 2.576

wake

θ

θ = 18°
θ = 90°
θ = 162°
θ = 234°
θ = 306°

x / R

-C$_P$

(b) Key blade angle : 88°

σ = 2.576

wake

θ

θ = 18°
θ = 90°
θ = 162°
θ = 234°
θ = 306°

x / R

-C$_P$

150

(c) Key blade angle : 184°
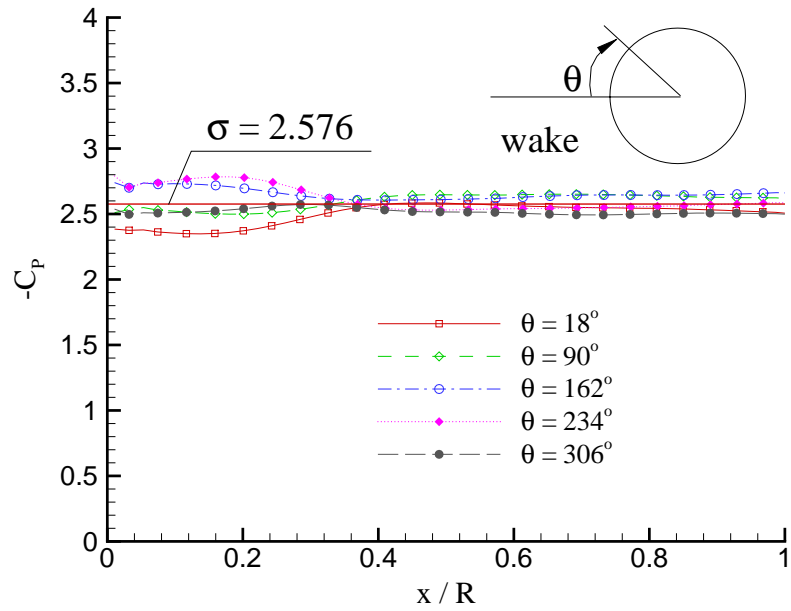
(d) Key blade angle : 272°
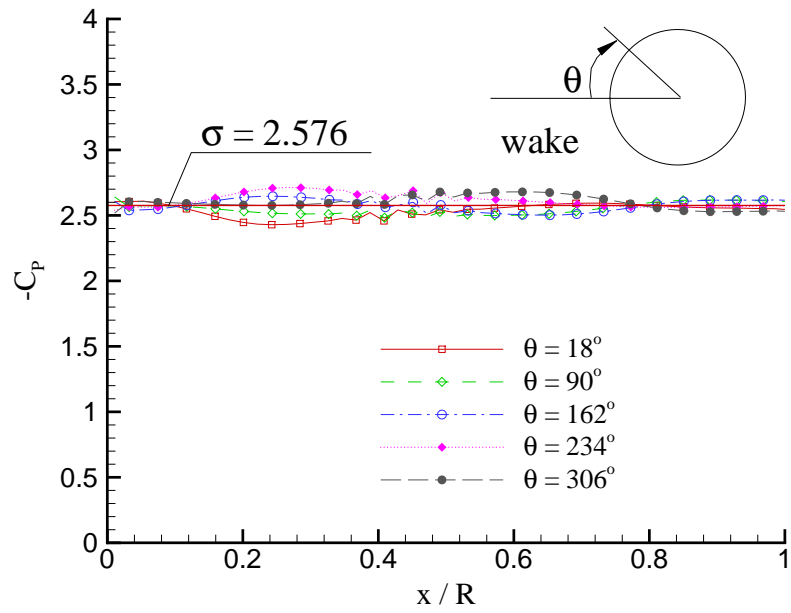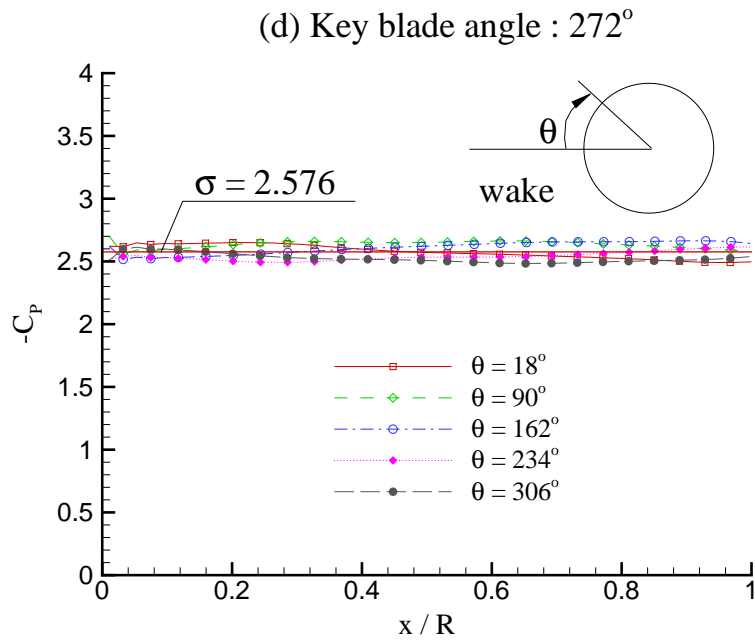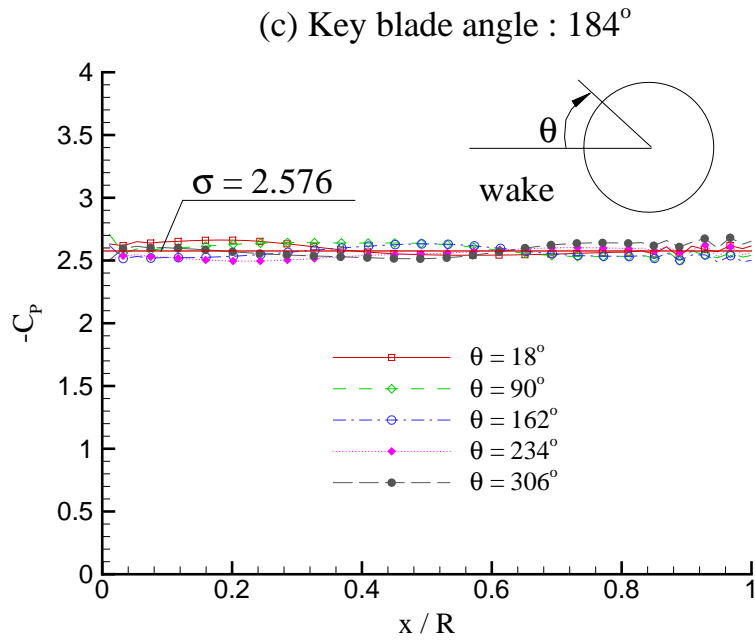
Figure 3.36: X-direction pressure distributions on developed tip vortex cavity for DTMB N4148 propeller. The pressures are depicted at key blade positions of (a) $\theta = 0^o$, (b) $\theta = 88^o$, (c) $\theta = 184^o$, and (d) $\theta = 272^o$: $J_s = 0.9087$, $F_n = 9.159$, and $\sigma_n = 2.576$.
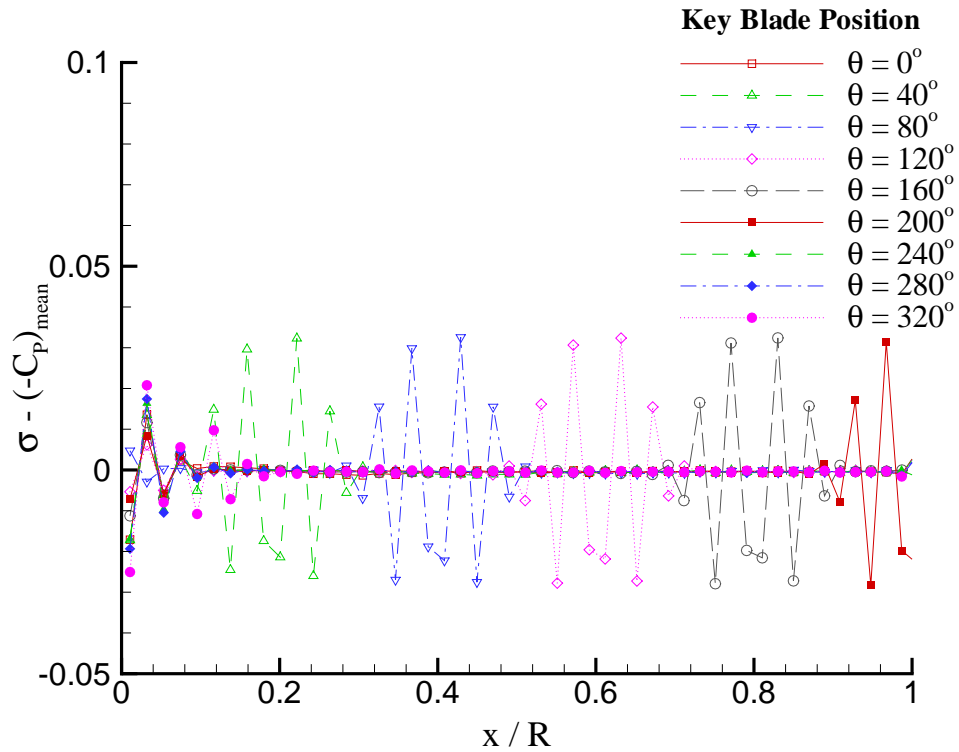
Figure 3.37: Pressure differences between cavitation number ($\sigma = 2.576$) and circumferentially averaged pressures at key blade positions of 0°, 40°, 80°, 120°, 160°, 200°, 240°, 280°, and 320° for DTMB N4148 propeller: $J_s = 0.9087$, $F_n = 9.159$, and $\sigma_n = 2.576$.

3.5 PROPCAV

In this section, the main features of the computer codes which have been developed and modified to analyze performance of marine propellers, using the boundary element method, are addressed.

- PSF-10 (Propeller Steady Flow)

  PSF-10 is a potential based boundary element code that treats fully wetted

propeller steady flows with hub model [Lee 1987; Kerwin et al. 1987]. The following features are included in the original PSF-10 code.

– Fully wetted steady performance analysis

– Planar panels on blade and wake surfaces

– Iterative Pressure Kutta condition

– Iterative block matrix solver

– Wake geometry is aligned with circumferentially averaged inflow (PSF2-type wake alignment) [Greeley and Kerwin 1982]

The original version of PSF-10 was improved by including hyperboloidal panels on blade and wake surfaces by [Hsin et al. 1991; Kinnas and Hsin 1992]

• PUF-10 (Propeller Unsteady Flow)

PUF-10 was developed based on PSF-10 to analyze the unsteady performance of marine propellers. It handles fully wetted conditions in non-axisymmetric inflow [Hsin 1989; Kinnas and Hsin 1992]. The followings are the main characteristics of PUF-10 code.

– Steady & unsteady fully wetted flow analysis

– Hyperboloidal panels on blade and wake surface

– Unsteady Iterative Pressure Kutta condition

– Linear dipole distribution on wake for unsteady analysis

153

– wake geometry is aligned with circumferentially averaged inflow (PSF2-type wake alignment) [Greeley and Kerwin 1982]

- PROPCAV (PROPeller CAVity analysis)

PROPCAV includes the ability of cavitating flow analysis, as well as fully wetted performance analysis [Fine 1992b; Kinnas and Fine 1992; Fine and Kinnas 1993a]. The fully wetted parts of PROPCAV are the same as those of PSF-10 and PUF-10. In addition to the ability of fully wetted steady & unsteady analysis of PSF-10 and PUF-10, the following are features of the original PROPCAV code.

– Steady & unsteady back cavity analysis

– Prescribed cavity detachment location

– Split panel method for cavitating analysis

– Iterative Pressure Kutta condition for fully wetted steady flow analysis

PROPCAV was extended by including several features as following:

– Leading edge and Mid-chord partial cavity on either the face or back of the blade [Mueller and Kinnas 1997; Mueller 1998; Mueller and Kinnas 1999].

– Leading edge and Mid-chord partial cavity on both the face and back of the blade simultaneously [Young and Kinnas 1999b, 2001a].

154

– Supercavitating propellers with non-zero trailing edge thickness as well as surface piercing propellers [Young and Kinnas 2001b; Young 2002; Young and Kinnas 2002]

The following are the contributions of the present work to the latest version of PROPCAV.

– Unsteady wake alignment

– Prediction of unsteady developed tip vortex cavitation

– Unsteady iterative Pressure Kutta condition for the cavitating analysis

3.6   Summary

A numerical technique which predicts blade sheet and developed tip vortex cavity has been developed by using a low order boundary element method. The developed method has been applied on the 2-D tip vortex cavity, 3-D hydrofoil and marine propeller problems. Details of formulation, boundary conditions, and solution methods were described. The numerical results were presented to validate the present method.

The shapes of blade sheet and developed tip vortex cavities were determined in an iterative manner by using the appropriate boundary conditions. On the blade sheet cavity surfaces, the perturbation potential was evaluated by using the dynamic boundary condition. The planform of the sheet cavity was determined by solving the partial differential equation for the cavity height which was derived from the

155

kinematic boundary condition. On the other hand, the developed tip vortex cavity was initially assumed as a solid body. The shape of tip vortex cavity was updated to satisfy the dynamic boundary condition by using a method based on the Jacobian of the pressure with respect to the adjustments on the cavity shape. The solution of the boundary value problem and the updating of the cavity shapes were repeated, until both blade sheet and tip vortex cavity shapes were converged. In addition, the wake alignment algorithm was applied, in order to improve the convergence of developed tip vortex cavity shapes.

The method was applied to the following problems to validate the present method.

- 2-D tip vortex cavity problem

The method was first applied to determine the tip vortex cavity shape of simple 2-D vortex system. The effects of circulation strengths on the tip vortex cavity shape were studied. Also, the convergence of the tip vortex cavity shapes and pressures with number of panels were presented. The cavity shapes and pressure distributions predicted from the direct and Jacobian methods compared very well to each other. Even though the computation of tip vortex cavity shape and the evaluation of pressure were programmed to use double precision on 64 bit workstation, the improvement of the pressure distribution on the tip vortex cavity surface appears to have a limitation due to the small radius of the tip vortex cavity.

- 3-D hydrofoil problem

156

The method was applied to the prediction of tip vortex cavity shape of 3-D elliptic hydrofoil. The dependence of the pressure distributions and the mean radius of tip vortex cavity on the number of panels was investigated. The results were found not to be sensitive to the number of panels in this case. Also, the convergence of the tip vortex cavity shapes with number of iterations was presented.

- 3-D propeller problem

A comparison of predicted cavity shapes was presented in the case of the DTMB N4148 propeller. The blade sheet cavity planform of DTMB N4148 propeller was compared well with those observed in the experiment and the computed using MPUF-3A (Vortex Lattice Method). The present method also was able to predict a developed tip vortex cavity that visually matched that of the experiment. The convergence of the forces with number of panels, time step size, and number of propeller revolutions was studied. The dependence of the blade sheet cavity planforms on number of panels and time step size were also investigated. In general, the present method shows stable convergence with number of panels, time step sizes and number of propeller revolutions.

Since no measurements on details of tip vortex cavity on marine propeller have been found in published papers, the systematic comparison with experiment has not been done in this thesis However, The pressure on the converged tip vortex cavity predicted to be close to the given cavitation number in the case of steady and unsteady inflows.

157

Examples of required CPU times for DTMB N4148 propeller in the case of blade sheet and tip vortex cavity analysis are shown in Table 3.1. The approximate times are only for the cavity calculation, i.e. all results computed from the unsteady fully wetted analysis are already stored in the computer (hard disk), and the cavity analysis uses those results by reading from the stored hard disk. The CPU times for the unsteady fully wetted analysis are shown in Table 2.1.

Blade Grid	Tip Vortex Grid	Cavity Analysis
40x10	60x10	2.15 hours
60x20	60x10	6.0 hours

Table 3.1: Approximate CPU time required on a COMPAQ DS20E with 2-833 MHz Processor (approximately 3-times as fast as an 1-GHz Pentium PC) for cavity analysis for DTMB N4148 propeller subjected to non-axisymmetric inflow.: J_s=0.9087, F_n=9.159, $\Delta\theta = 6^o$, 6 revolutions for unsteady cavity (blade sheet and tip vortex cavity) analysis.

Chapter 4

Bursting of Tip Vortex Cavity

4.1 Introduction

As mentioned in Section 1.2, the common problems caused by the occurrence of tip vortex cavity are erosion and unsteady pressure fluctuations on the ship hull. In particular, when the propeller blade passes through the wake peak region where the flow velocities change or decrease abruptly, the developed tip vortex cavity shows the bursting phenomenon. Even though the tip vortex cavity bursting is not a common phenomenon on propellers, it generates pressure fluctuations on hull once it occurs. The bursting of a tip vortex cavity is often known as *vortex bursting* or *vortex breakdown*. However, the behavior of the tip vortex cavity bursting is different from that of stationary vortex bursting.

The vortex bursting is often observed to occur over delta wings at large angle of attacks, and in axisymmetric swirling flows in tubes. [Sarpkaya 1971] performed vortex breakdown experiments in swirling flows in a diverging cylindrical tube, and observed three basic types of stationary vortex breakdown: double helix, spiral, and axisymmetric. Also, he noticed that the vortex breakdown phenomenon is governed by hydrodynamic instability and finite transition of flow condition.

On the other hand, the main parameter of tip vortex cavity bursting is the

159

variation of vortex strength. The tip vortex cavity experiences an increasing vortex strength inside the wake peak region, and as a result the diameter of the tip vortex cavity increases. After the tip vortex cavity passes the wake peak region, the strength of the vortex decreases and so does the diameter of tip vortex cavity. [Kuiper 2001] observed the bursting of tip vortex cavitation on a Navy oiler on a 5 bladed controllable pitch propeller. According to his experiments, contrary to the phenomenon of vortex bursting, the tip vortex cavity does not disappear after the burst, and the tip vortex cavity core is continued without weakening of the vortex. Therefore, this phenomenon should be called as a *blowing up* of the tip vortex cavity rather than a *vortex bursting* [Kuiper 2001].

4.2   Objectives

In order to understand the hydrodynamic mechanisms of bursting of a tip vortex cavity on a marine propeller, it is necessary to initiate a systematic study starting with unsteady bursting of a tip vortex cavity in 2-D. Even though the theoretical basis and computational tools on 2-D cavity bursting problem are not fully developed in this work, the proposed method is addressed here rather than in the next chapter of recommendations, in order to help future studies.

The objectives of this chapter are as follows :

- Develop a simple 2-D unsteady model relating to the 3-D bursting of a tip vortex cavity.

- Derive numerical formulations for 2-D unsteady bursting problem.

- Produce preliminary results of the 2-D problem.

4.3 Formulation

The numerical modeling on 2-D bursting of a tip vortex cavity and some preliminary results are presented in this section.

4.3.1 Problem definition

Since the main parameter of the bursting of a tip vortex cavity on marine propellers is the variation of the vortex strength in the fluid domain, the 2-D vortex bursting has to be modeled with variable vortex strength. By applying a circulation with variable strengths of Γ, 2-D tip vortex cavity model defined in Section 3.2 can be extended for modeling of the tip vortex cavity bursting. The tip vortex cavity is modeled as shown in Fig. 3.1, and the variation of circulation is given by

$$\Gamma(t) = \Gamma_o + \Delta\Gamma \sin \omega t \tag{4.1}$$

where Γ_o and $\Delta\Gamma$ are the mean circulation and the amplitude of circulation varia-
tion, respectively. $\omega = \frac{2\pi}{T}$ is the frequency of the fluctuating circulation, and T is the fluctuating period. The upward velocity[1] is defined as

$$U_{up}(t) = \frac{\Gamma(t)}{2\pi R} = U_\infty \sin \alpha_{up} \tag{4.2}$$

---

[1]This velocity is necessary to cancel the induced velocity of the non-cavitating vortex, as explained in Section 3.2.

4.3.2 Formulation

Details on the BEM formulation on 2-D tip vortex cavity problem are addressed in Section 3.2.2, except that potential, ϕ, and circulation, Γ are now functions of time, t.

The boundary conditions which have to be satisfied on the tip vortex cavity surface are as follows :

- Dynamic boundary condition

The dynamic boundary condition can be derived by applying the unsteady Bernoulli's equation[2].

$$\frac{P_o}{\rho} + \frac{|\vec{q}_{in}|^2}{2} = \frac{P}{2} + \frac{|\vec{q}_t|^2}{2} + \frac{\partial \phi}{\partial t} \tag{4.3}$$

where $\vec{q}_{in} = (0, U_{up})$, and P_o and P are the reference pressure far upstream and the pressure on tip vortex cavity surface. $\vec{q}_t$ is the total velocity on tip vortex cavity, which is given by

$$\vec{q}_t = \left(\frac{\partial \phi}{\partial n} + \vec{q}_{in} \cdot \vec{n} \right) \vec{n} + \left(\frac{\partial \phi}{\partial v} + \vec{q}_{in} \cdot \vec{v} \right) \vec{v} \tag{4.4}$$

where $\vec{n}$ and $\vec{v}$ represent the normal and tangential unit vectors on the tip vortex cavity surface.

- Kinematic boundary condition

---

[2]The unsteady terms due to the inflow potential, $\frac{\partial \Phi_{in}}{\partial t}$, on both sides of Bernoulli's equation are canceling each other.

The kinematic condition on the tip vortex cavity requires the fluid particles to move with that surface :

$$\frac{\partial h}{\partial t} = \frac{\partial \phi}{\partial n} + \vec{q}_{in} \cdot \vec{n} \tag{4.5}$$

where h is the increment of tip vortex cavity radius.

By combining Eqns. 4.3 and 4.5, the equation for the unsteady pressure can be obtained as follows :

$$\begin{aligned}
-C_P &= \frac{P_o - P}{\frac{1}{2}\rho U_\infty^2} \\
&= \left(\frac{\partial \phi}{\partial v} + \vec{q}_{in} \cdot \vec{v}\right)^2 - \sin^2 \alpha_{up} + \left(\frac{\partial h}{\partial t}\right)^2 + 2\frac{\partial \phi}{\partial t}
\end{aligned} \tag{4.6}$$

Since the potential is evaluated on the updated tip vortex cavity surface, the time derivative of this potential represents the substantial derivative. Therefore, the partial derivative of potential is derived as follows:

$$\begin{aligned}
\frac{\partial \phi}{\partial t} &= \frac{D\phi}{Dt} - \frac{\partial \phi}{\partial n}\frac{\Delta h}{\Delta t} \\
&= \frac{D\phi}{Dt} + \left(\vec{U}_{in} \cdot \vec{n} - \frac{\partial h}{\partial t}\right)\frac{\partial h}{\partial t}
\end{aligned} \tag{4.7}$$

By substituting Eqn. 4.7 into Eqn. 4.6, the pressure for the unsteady problem can be derived as follows :

$$-C_P = \left(\frac{\partial \phi}{\partial v} + \vec{q}_{in} \cdot \vec{v}\right)^2 - \sin^2 \alpha_{up} + 2\frac{D\phi}{Dt} + 2\left(\vec{q}_{in} \cdot \vec{n}\right)\frac{\partial h}{\partial t} - \left(\frac{\partial h}{\partial t}\right)^2 \tag{4.8}$$

The pressure on the tip vortex cavity surface at each time step can be evaluated by including the time derivatives of the potential and the cavity radius increment, as shown in Eqn. 4.8

163

4.4   Numerical Implementation

In Section 3.2.2, two methods were applied to solve for the tip vortex cavity problem : the direct and the Jacobian method. The Jacobian method is applied to solve the unsteady bursting problem, and the unsteady terms are evaluated by using the averaged 3-point backward scheme [Young et al. 2001].

$$\frac{D\phi}{Dt} = \frac{\phi^t + \phi^{t-1} + \phi^{t-2}}{3(2\Delta t)} - \frac{\phi^{t-2} + \phi^{t-3} + \phi^{t-4}}{3(2\Delta t)} \tag{4.9}$$

, and

$$\frac{\partial h}{\partial t} = \frac{h^t + h^{t-1} + h^{t-2}}{3(2\Delta t)} - \frac{h^{t-2} + h^{t-3} + h^{t-4}}{3(2\Delta t)} \tag{4.10}$$

At each time step, Green's formula, Eqn. 3.7, is solved with respect to the unknown potential, ϕ, on the tip vortex cavity surface for the corresponding vortex strength, $\Gamma(t)$. Once the potential is evaluated on the tip vortex surface, the pressure can be computed by using Eqn. 4.8. If the updated pressure is not equal to the given cavitation number, σ, the new shape of tip vortex cavity is computed using the Jacobian method described in Section 3.2.4.

4.5   Numerical Results

The proposed numerical method is applied to the tip vortex cavity problem with the following conditions : $\Gamma_o = 1.0$ (m^2/sec), $\Delta\Gamma = 0.2$ (m^2/sec), $\omega = 0.1, 0.2, 0.5,$ and 1.0 $(1/sec)$, $\sigma = 1.0$, and $\Delta t = \frac{T}{100}$ (sec).

The predicted tip vortex cavity shapes for various vortex strengths and frequencies are shown in Fig. 4.1. As the frequency increases, the motion of tip vortex cavity becomes more irregular.

Figure 4.2 shows the pressure distributions predicted on the tip vortex surfaces shown in Fig. 4.1. Even though the pressures are required to satisfy the dynamic boundary condition, the predicted pressures show some discrepancy from the given cavitation number, $\sigma = 1.0$. However, the circumferentially averaged pressures along the tip vortex circumference seem to be very close to cavitation number.

4.6 Summary

A boundary element method was applied to the preliminary analysis of 2-D unsteady bursting of tip vortex cavity. The numerical method proposed in this chapter is still under development, and this chapter is introduced as a subsidiary part of the recommendations.

Two dimensional tip vortex cavity bursting was modeled by applying the variable vortex strength as a function of frequency. A Jacobian method was applied to evaluate the new tip vortex shape which is required to satisfy the dynamic and kinematic boundary conditions. The predicted results show the expected vortex fluctuations with the variation of vortex strength, however, the predicted pressures on the tip vortex surface show some discrepancy from the given cavitation number. This subject requires further investigation in the future.

(a) ω = 0.1

	t = 0.00 sec, Γ = 1.0
	t = 15.08 sec, Γ = 1.2
	t = 31.42 sec, Γ = 1.0
	t = 46.50 sec, Γ = 0.8

(b) ω = 0.2

	t = 0.00 sec, Γ = 1.0
	t = 7.54 sec, Γ = 1.2
	t = 15.71 sec, Γ = 1.0
	t = 23.25 sec, Γ = 0.8

166
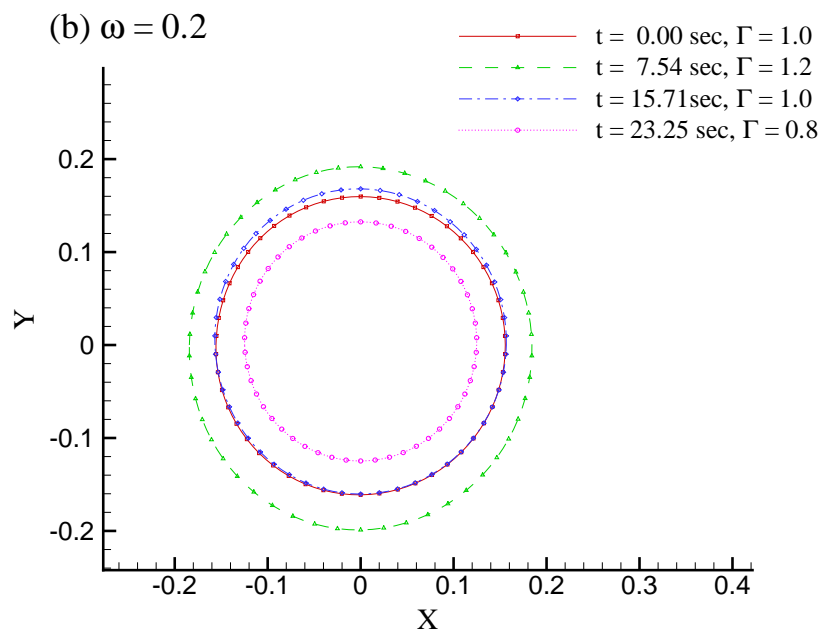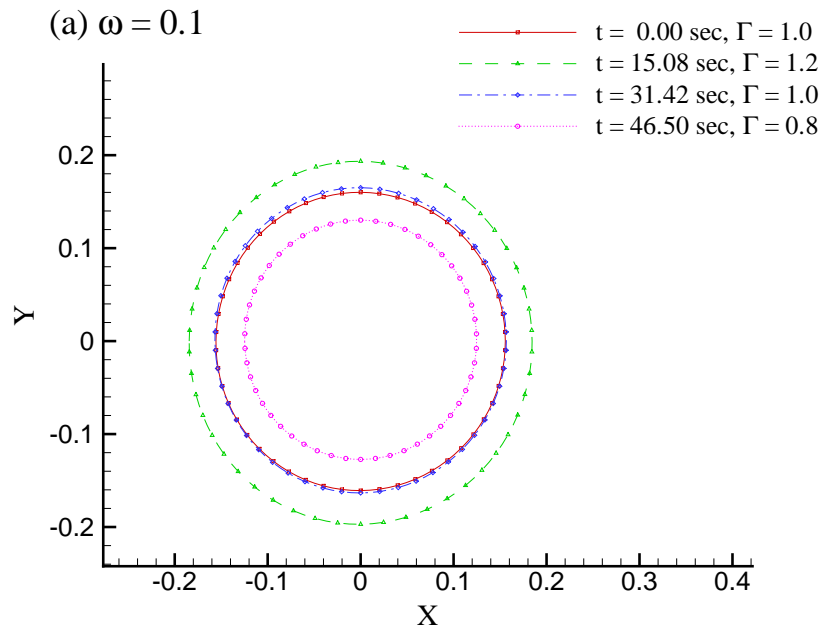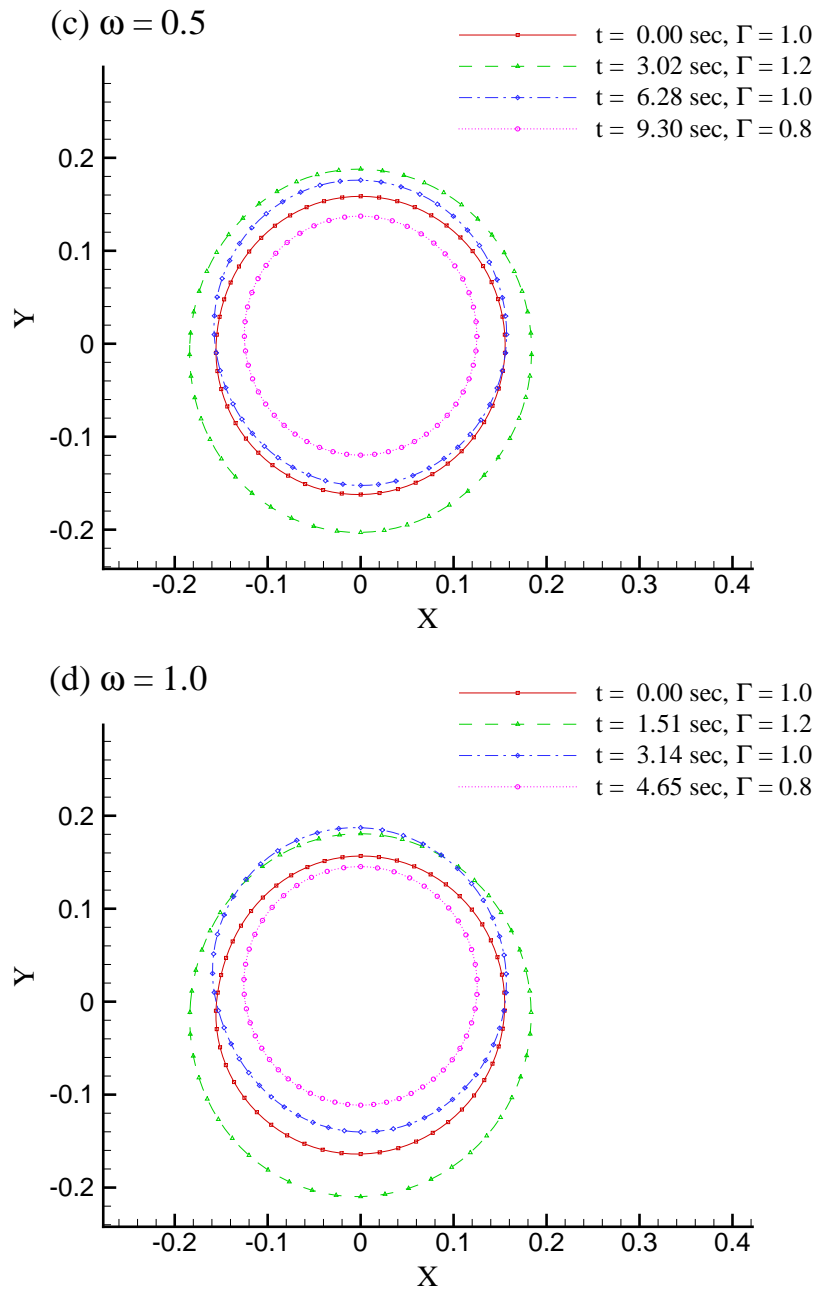
Figure 4.1: Comparisons of tip vortex cavity shapes with the variation of vortex strengths at each frequency: (a) $\omega = 0.1$, (b) $\omega = 0.2$, (c) $\omega = 0.5$, and (d) $\omega = 1.0$.

(a) $\omega = 0.1$

t = 0.00 sec, $\Gamma = 1.0$
t = 15.08 sec, $\Gamma = 1.2$
t = 31.42 sec, $\Gamma = 1.0$
t = 46.50 sec, $\Gamma = 0.8$

(b) $\omega = 0.2$

t = 0.00 sec, $\Gamma = 1.0$
t = 7.54 sec, $\Gamma = 1.2$
t = 15.71 sec, $\Gamma = 1.0$
t = 23.25 sec, $\Gamma = 0.8$

168

(c) $\omega = 0.5$

(d) $\omega = 1.0$
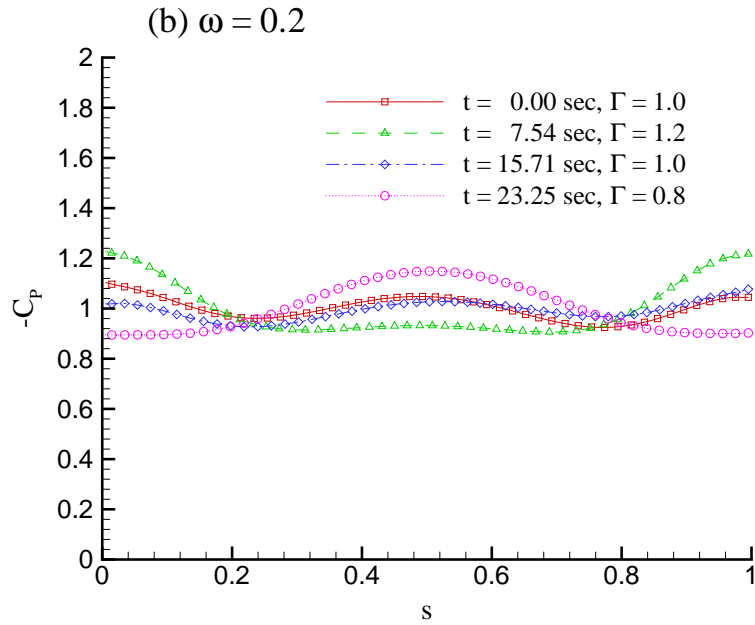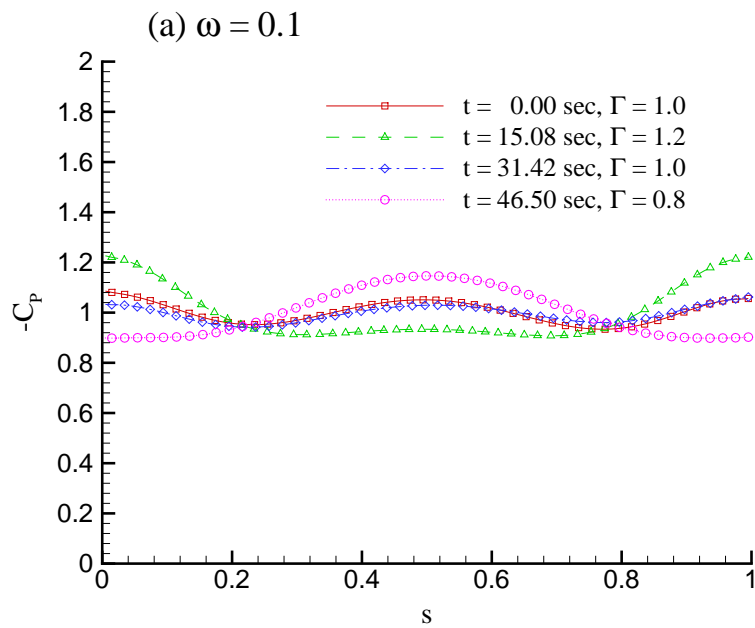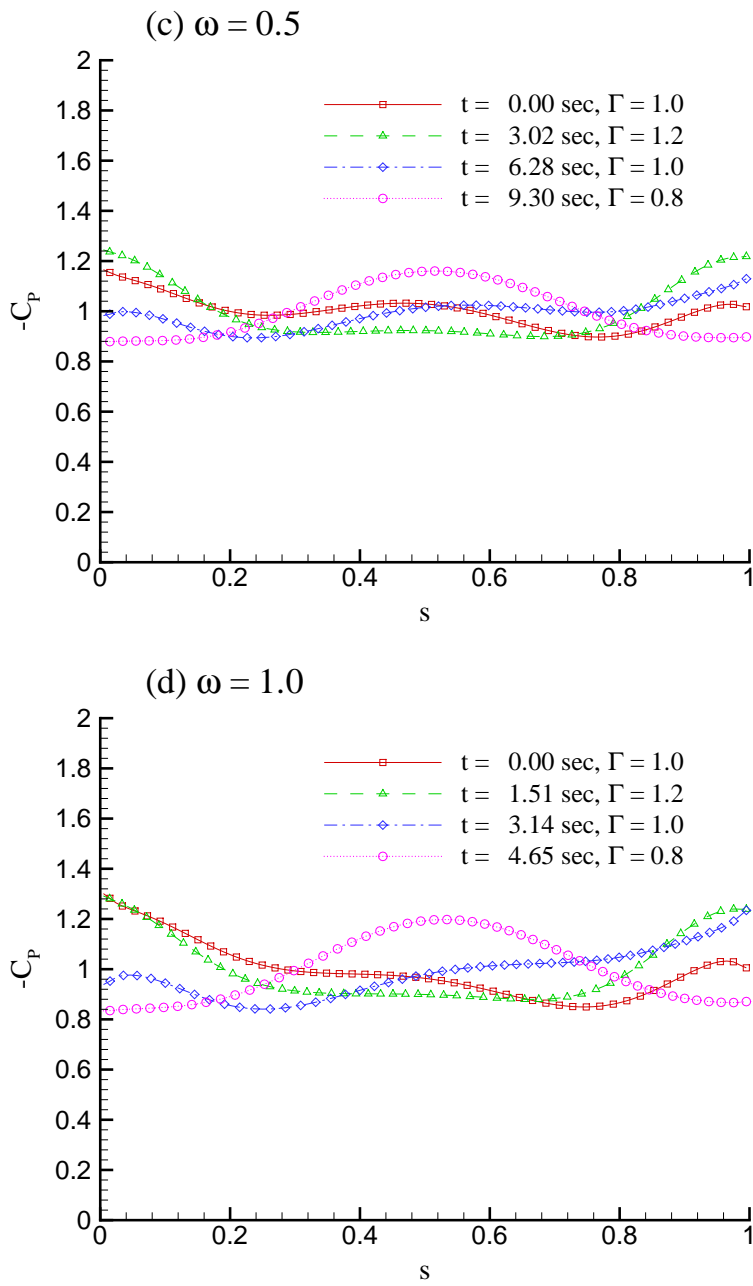
Figure 4.2: Pressure comparisons on tip vortex cavity shapes with the variation of vortex strengths at each frequency: (a) $\omega = 0.1$, (b) $\omega = 0.2$, (c) $\omega = 0.5$, and (d) $\omega = 1.0$.

169

Chapter 5

Conclusions and Recommendations

5.1 Conclusions

In this thesis, a robust and reliable numerical method for the prediction of blade sheet and developed tip vortex cavitation has been developed by using a low order boundary element method.

The main contributions of the present work are :

• Prediction of the aligned unsteady wake geometry using a low order boundary element method: Previous methods for the alignment of the propeller wake geometry addressed steady flow. Also, the wake geometry in the case of unsteady flows was fixed in time, and was determined in the circumferentially averaged flow field. In addition, wake contraction and roll-up motion were modeled using prescribed values which were measured from experiments. In the present work, a fully unsteady wake alignment scheme was developed using a low order boundary element method. The wake sheet is determined to satisfy the force free condition on the wake surface. In order to avoid numerical instability, the induced velocities are evaluated at a certain distance from the actual control point, and the tip vortex core was introduced at the wake tip end. The contraction and roll-up of the wake sheet are directly determined while the wake geometry is aligned to satisfy the force-

free condition. In the case of unsteady inflow, the wake geometry is aligned in a fully unsteady manner by updating the wake geometry at each time step. The method is extensively validated by numerical convergence and consistency tests for 2-D vortex roll-up, for 3-D hydrofoils in steady flow, for propellers in uniform and non-axisymmetric flow, and for propellers in an inclined flow.

• Prediction of unsteady blade sheet and developed tip vortex cavitations: A numerical method which predicts developed tip vortex cavities, in addition to blade sheet cavities, on propellers is developed by using a low order BEM. The shape of the developed tip vortex cavities are iteratively determined by using the dynamic and kinematic boundary conditions on each panel on the cavity surface. The developed tip vortex cavity shape is determined by satisfying the dynamic boundary condition using a method based on the Jacobian of the pressures with respect to the surface adjustments. The method is applied on 2-D tip vortex cavity, 3-D hydrofoil in steady flow, and propeller in unsteady flow.

5.2   Recommendations

Even though the present method predicts accurately the shapes of blade sheet and developed tip vortex cavities on propellers, the following may be included to improve the present numerical scheme.

- Regrid the 3-D wake sheet : The regridding scheme which is applied for the 2-D roll-up problem, is possible to implement not only for the aligned wake geometry but also for the trailing vortex strength in the cases of 3-D hydrofoil

and propeller problems. A regridding scheme may improve the prediction of wake contraction and vortex roll-up by distributing more panels near the wake tip region.

- Include a sub-panel near the blade trailing edge : The present method uses constant panel size on wake surface to easily treat the unsteady vortex shedding. In order to predict more accurately the wake contraction near the blade trailing edge, it is essential to use a finer grid for several panels on the wake surface. It should be possible to implement a sub-panel method on several consecutive panels close to the blade trailing edge, such as the one developed by [Kinnas and Hsin 1992].

  Other recommendations for further research follow:

- Modeling of hub vortex cavitation : Hub vortex cavitation is a vortex type of cavitation like the tip vortex cavitation, which occurs at the hub of the propeller. Even though hub vortex cavitation forms a rope-like cavity with strands corresponding to the number of propeller blades, it may be initially modeled as a circular cylinder, and then the exact shape may be determined by using the scheme that has developed for tip vortex cavities in this thesis. Fig. 5.1 shows the proposed numerical modeling of hub vortex cavitation on a propeller. The detachment location of the hub vortex cavitation on hub surface may be determined by using the same algorithm which was used to find the detachment points on blade surface [Kinnas et al. 1997; Mueller and

172
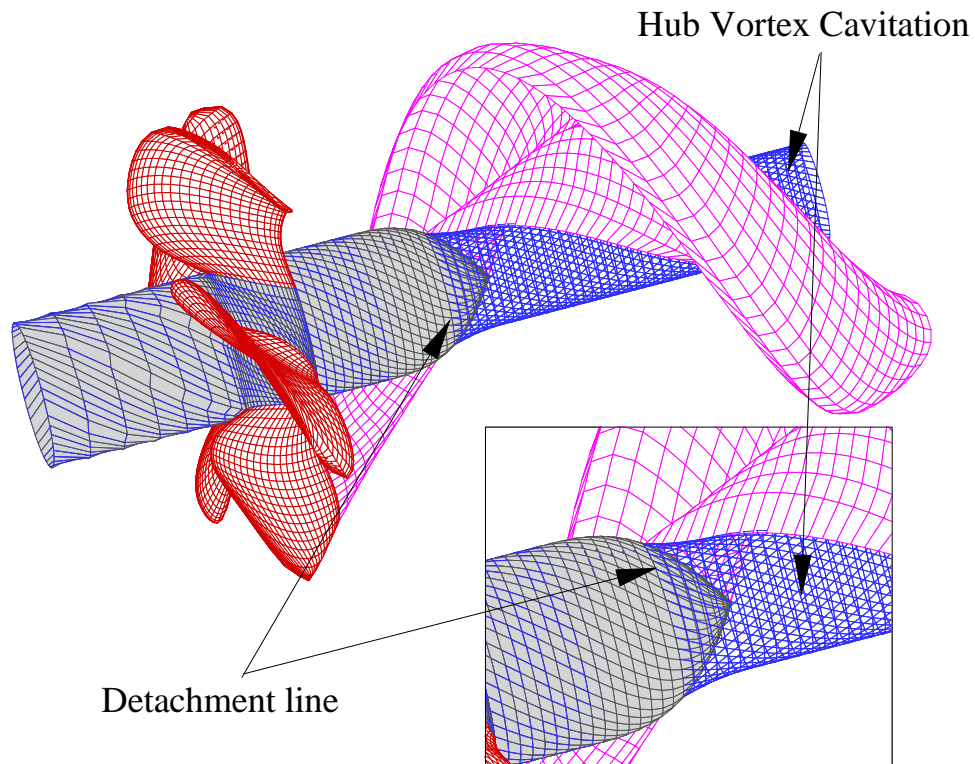
Figure 5.1: Modeling of hub vortex cavitation.

Kinnas 1997; Mueller 1998; Mueller and Kinnas 1999; Young and Kinnas 1999b, 2001a].

- Modeling of bursting of tip vortex cavity : The proposed 2-D tip vortex cavity bursting problem in Section 4 requires systematic convergence and consistency tests with varying frequencies, vortex strengths and cavitation numbers. Also, the 3-D unsteady bursting problem can be treated by using the algorithm developed to solve the tip vortex cavity problem. As the propeller blade passes through the top of the wake region where the inflow velocity is

173

slow, the tip vortex cavity initially can be modeled as a solid body of constant radius. By updating a vortex strength as the propeller rotates in an unsteady manner, the shape of the bursting tip vortex cavity will be adjusted so that the dynamic and kinematic boundary conditions are satisfied.

- Determining the pressure fluctuations on the hull due to blade sheet and developed tip vortex cavitations : As mentioned in Section 1.2, one of the common problems due to developed tip vortex cavitation is pressure fluctuations (or broadband excitations) of the hull. In order to determine the hull pressure fluctuations, the present method has to be incorporated with the numerical solver which can solve ship hull diffraction problem. A BEM code, HULLFPP, solves for the propeller induced hull pressures arising from intermittent blade cavitation, loading and thickness [Kinnas 1996; Young and Kinnas 1999a]. Currently HULLFPP is coupled with MPUF-3A which uses the Vortex Lattice Method. Once the unsteady cavity problem is solved by using the present method, the induced potential on the ship hull due to the propeller and cavitations are determined from the Green's formula, as shown in Eqn. 5.1

$$4\pi\phi^P = \iint_{S_P} \left[\phi_q \frac{\partial}{\partial n_q} \frac{1}{R} - \frac{\partial \phi_q}{\partial n_q} \frac{1}{R} \right] dS + \iint_{S_W} \Delta\phi_w \frac{\partial}{\partial n_q} \frac{1}{R} ds \qquad (5.1)$$

where ϕ^P is the potential on the ship hull induced by the propeller. S_P represents the blade, hub and cavity surfaces, and S_W represents the wake surface. A function R is a distance between a field point on ship hull and a singular point (or source point, q) on S_P and S_W. Once the induced potential on

174

ship hull is determined, the boundary value problem for the ship hull can be derived by including the effect of propeller as follows [Breslin et al. 1982]:

$$2\pi\phi^H - \iint_{S_H} \phi^H \frac{\partial}{\partial n_q} \frac{1}{R} dS = 4\pi\phi^P \qquad (5.2)$$

where ϕ^H denotes the potential on the ship hull, and S_H represents the ship hull surface.

- Performing systematic series of experiments on blade sheet and developed tip vortex cavitation on propellers : Experiments should be used to validate the numerical results developed for the prediction of propeller sheet and developed tip vortex cavitations. The planform of blade sheet cavity should be measured through cavity observation tests in steady and unsteady flow. The size or radius of developed tip vortex cavity should be determined by using LDV or PIV systems. In addition, the propeller thrust and torque in steady and unsteady flows should be measured and compared with those of computed values, specially in the case of cavitating propellers. The effects of Reynolds number, cavitation number, advance ratio, and air and bubble or nuclei contents on the tip vortex cavity radius should also be investigated.

175

Bibliography

Achkinnadze, A. and Krasilnikov, V. (2001). A velocity based boundary element method with modified trailing edge for prediction of the partial cavities on the wings and propeller blades. In *CAV 2001: Fourth International Symposium on Cavitation*, Pasadena, CA. California Institute of Technology.

Acosta, A. (1955). A Note on Partial Cavitation of Flat Plate Hydrofoils. Technical Report No. E-19.9, California Institute of Technology, Hydrodynamics Laboratory.

Almosnino, D. (1985). High Angle-of-Attach Calculations of the Subsonic Vortex Flow on Slender Bodies. *AIAA Journal*, 23(8):1150–1156.

Ando, J. and Nakatake, K. (2001). Calculation of three-dimensional unsteady sheet cavitation by a simple surface panel method sqcm. In *CAV 2001: Fourth International Symposium on Cavitation*, Pasadena, CA. California Institute of Technology.

Arndt, R., Arakeri, V., and Higuchi, H. (1991). Some observations of tip-vortex cavitation. *Journal of Fluid Mech.*, 229:269–289.

Arndt, R. and Dugue, C. (1992). Recent advances in tip vortex cavitation research. In *International Symposium on Propulsors and Cavitation*, Hamburg, Germany.

Arndt, R. and Keller, A. (1992). Water quality effects on cavitation inception in a trailing vortex. *Journal of Fluid Enginnering*, 114:430–438.

Astolfi, J.-A., Fruman, D., and Billard, J.-Y. (1999). A model for tip vortex roll-up in the near field region of three-dimensional foils and the prediction of cavitation onset. *European Journal of Mechanics-B/Fluids*, 18:757–775.

Baker, G. (1980). A test of the method of Fink and Soh for following vortex sheet motion. *Journal of Fluid Mechanics*, 100(1):209–220.

Bal, S., Kinnas, S., and Lee, H. (2001). Numerical analysis of 2-d and 3-d cavitating hydrofoils under a free surface. *Journal of Ship Research*, 45:34–49.

Batchelor, G. (1964). Axial flow in trailing line vortices. *Journal of Fluids Mechanics*, 20:645–658.

Billet, M. and Holl, J. (1981). Scale effects on various types of limited cavitation. *Journal of Fluids Engineering*, 103:405–414.

Boswell, R., Jessup, S., Kim, K., and Dahmer, D. (1984). Single-Blade Loads on Propellers in Inclined and Axial Flows. Technical Report DTNSRDC-84/084, DTNSRDC.

Breslin, J., Van Houten, R., Kerwin, J., and Johnsson, C.-A. (1982). Theoretical and experimental propeller-induced hull pressures arising from intermittent blade cavitation, loading, and thickness. *Trans. SNAME*, 90.

177

Briançon-Marjolet, L. and Merle, L. (1996). Inception, development, and noise of a tip vortex cavitation. In *21th Symposium on Naval Hydrodynamics*, pages 278–290, Trondheim, Norway.

Brown, C. (1973). Aerodynamics of Wake Vortices. *AIAA Journal*, 11:531–536.

Carlton, J. (1994). *Marine Propellers and Propulsion*. Butterworth Heinemann Ltd.

Chesnakas, C. and Jessup, S. (1998). Experimental characterization of propeller tip flow. In *22st Symposium on Naval Hydrodynamics*, USA, Washington D.C.

Choi, J. and Kinnas, S. (2000). An unsteady three-dimensional euler solver coupled with a cavitating propeller analysis method. In *The 23rd Symposium on Naval Hydrodynamics*, Val de Reuil, France.

Choi, J.-K. and Kinnas, S. (1998). A 3-D Euler Solver and Its Application on the Analysis of Cavitating Propellers. In *25th American Towing Tank Conference*, Iowa City, IA.

Choi, J.-K. and Kinnas, S. (2001). Prediction of non-axisymmetric effective wake by a 3-D Euler solver. *Journal of Ship Research*, 45(1):13–33.

Chorin, A. and Bernard, P. (1973). Discretization of a Vortex Sheet, with an Example of Roll-Up. *Journal of Computational Physics*, 13:423–429.

Clements, R. and Maull, D. (1973). The rolling up of a trailing vortex sheet. *The Aeronautical Journal*.

178

Esposito, P. and Salvatore, F. (2000). Optimal design of cavitating blade sections by genetic algorithms. In *NCT50, International Conference on Propeller Cavitation*, Newcastle upon Tyne, England.

Fine, N. (1992a). *Nonlinear Analysis of Cavitating Propellers in Nonuniform Flow*. PhD thesis, M.I.T., Department of Ocean Engineering.

Fine, N. and Kinnas, S. (1993a). The nonlinear numerical prediction of unsteady sheet cavitation for propellers. In *Sixth International Conference On Numerical Ship Hydrodynamics*, University of Iowa, Iowa.

Fine, N. E. (October, 1992b). *Nonlinear Analysis of Cavitating Propellers in Nonuniform Flow*. PhD thesis, Department of Ocean Engineering, MIT.

Fine, N. E. and Kinnas, S. (1993b). A boundary element method for the analysis of the flow around 3-d cavitating hydrofoils. *Journal of Ship Research*, 37:213–224.

Fink, P. and Soh, W. (1978). A New Approach to Roll-Up Calculations of Vortex Sheets. In *Proceedings of the Royal Society of London,Series A*, volume 362, pages 195–209.

Fruman, D., Cerrutti, P., Pichon, T., and Dupont, P. (1995). Effect of hydrofoil planform on tip vortex roll-up and cavitation. *Journal of Fluids Engineering*, 119:162–169.

Fruman, D., Dugué, C., Pauchet, A., Cerruti, P., and Briançon-Marjolet, L. (1992). Tip vortex roll-up and cavitation. In *Proceedings of Nineteenth Symposium on Naval Hydrodynamics*, Seoul ,Korea.

Geurst, J. and Timman, R. (1956). Linearized Theory of Two-Dimensional Cavitational Flow Around a Wing Section. *IX International Congress of Applied Mechanics*.

Gowing, S., Briançon-Marjolet, L., Frechou, D., and Godefrroy, V. (1995). Dissolved gas and nuclei effects on tip vortex cavitation inception and cavitating core size. In *Proceedings of 5th International Symposium on Cavitation*, pages 173–180, Deauville, France.

Greeley, D. and Kerwin, J. (1982). Numerical methods for propeller design and analysis in steady flow. *Trans. SNAME*, 90.

Guiraud, J. and Zeytounian, R. (1977). A double-scale investigation of the asymptotic structure of rolled-up vortex sheets. *Journal of Fluid Mechanics*, 79:93–112.

Hess, J. L. and Valarezo, W. (1985). Calculation of steady flow about propellers by means of a surface panel method. In *23rd Aerospace Sciences Meeting*, Reno, Nevada. AIAA.

Hoeijmakers, H. and Bennekers, B. (1979). A computational method for the calculation of the flow about wings with leading edge vortices. *AGARD-CP-247*, page Pap. 25.

Hoeijmakers, H. and Vaatstra, W. (1983). A Higher-Order Panel Method Applied to Vortex Sheet Roll-Up. *AIAA Journal*, 21:516–523.

Hsiao, C. and Chahine, G. (2002). Prediction of vortex cavitation inception using coupled spherical and non-spherical models and unrans computations. In *The 24rd Symposium on Naval Hydrodynamics*, Fukuoka, Japan.

Hsin, C. (1989). *Development and Analysis of Panel Methods for Propellers in Unsteady Flow*. PhD thesis, M.I.T., Department of Ocean Engineering.

Hsin, C.-Y., Kerwin, J., and Kinnas, S. (1991). A panel method for the analysis of the flow around highly skewed propellers. In *Propellers/Shafting '91 Symposium*, pages 1–13 (paper No. 11), Virginia Beach, VA. Soc. Naval Arch. & Marine Engnrs.

Hsu, C. (1991). Studies of scaling of tip vortex cavitation inception on marine lifting surfaces. *Journal of Fluids Engineering*, 113:504–508.

Jessup, S. (1989). *An Experimental Investigation of Viscous Aspects of Propeller Blade Flow*. PhD thesis, The Catholic University of America.

Jiang, C. and Leehey, P. (1977). A Numerical Method for Determining Forces and Moments on Supercavitating Hydrofoils of Finite Span. In *Second Int'l Conf. Numer. Ship Hydrodynamics*, Berkeley.

Johnson, F., Tinoco, E., Lu, P., and M.A., E. (1980). Three-dimensional flow over wings with leading edge vortex separation. *AIAA Journal*, 18:367–380.

Kaden, H. (1931). Aufwicklung einer unstabilien Unstetigkeitsflache. *Ingenieur Archiv*, Vol 2.

Kandil, O. (1985). Computational Technique for Compressible Vortex Flows Past Wings at Large Incidence. *Journal of Aircraft*, 22(9):750–755.

Keenan, D. P. (1989). *Marine Propellers in Unsteady flow*. PhD thesis, Massachusetts Institute of Technology.

Kerwin, J., Kinnas, S., Lee, J.-T., and Shih, W.-Z. (1987). A surface panel method for the hydrodynamic analysis of ducted propellers. *Trans. SNAME*, 95.

Kerwin, J., Kinnas, S., Wilson, M., and J., M. (1986). Experimental and analytical techniques for the study of unsteady propeller sheet cavitation. In *Sixteenth Symposium on Naval Hydrodynamics*, Berkeley, California.

Kerwin, J. and Lee, C.-S. (1978). Prediction of Steady and Unsteady Marine Propeller Performance by Numerical Lifting-Surface Theory. *Trans. SNAME*, 86.

Kim, Y.-G. and Lee, C.-S. (1993). Prediction of unsteady cavity behavior around 2-d hydrofoil in heave or gust. In *The Second Japan-Korea Joint Workshop on Ship and Marine Hydrodynamcs*, pages 299–308.

Kim, Y.-G. and Lee, C.-S. (1996). Prediction of unsteady performance of marine propellers with cavitation using surface-panel method. In *21st Symposium on Naval Hydrodynamics*, Trondheim, Norway.

Kim, Y.-G., Lee, C.-S., and Suh, J.-C. (1994). Surface panel method for prediction of flow around a 3-d steady or unsteady cavitating hydrofoil. In *Second International Symposium on Cavitation*, pages 113–120, Tokyo, Japan.

Kinnas, S. (1984). Cavity shape characteristics for supercavitating hydrofoils. Technical Report 84-13, MIT, Department of Ocean Engineering.

Kinnas, S. (1985a). Cavity shape characteristics for partially cavitating hydrofoils. Technical Report 85-1, MIT, Department of Ocean Engineering.

Kinnas, S. (1985b). Non-linear corrections to the linear theory for the prediction of the cavitating flow around hydrofoils. Technical Report 85-10, MIT, Department of Ocean Engineering.

Kinnas, S. (1991). Leading-edge corrections to the linear theory of partially cavitating hydrofoils. *Journal of Ship Research*, 35(1):pp. 15–27.

Kinnas, S. (1992). A general theory for the coupling between thickness and loading for wings and propellers. *Journal of Ship Research*, 36(1):59–68.

Kinnas, S. (1996). An international consortium on high-speed propulsion. *Marine Technology*, 33(3):pp. 203–210.

Kinnas, S., Choi, J., Lee, H., and Young, J. (2000). Numerical cavitation tunnel. In *NCT50, International Conference on Propeller Cavitation*, Newcastle upon Tyne, England.

Kinnas, S. and Coney, W. (1992). The generalized image model - an application to the design of ducted propellers. *Journal of Ship Research*, 36(3):197–209.

Kinnas, S. and Fine, N. (1989). Theoretical prediction of the midchord and face unsteady propeller sheet cavitation. In *Fifth International Conference on Numerical Ship Hydrodynamics*, pages 685–700, Hiroshima, Japan.

Kinnas, S. and Fine, N. (1990). Non-Linear Analysis of the Flow Around Partially or Super-Cavitating Hydrofoils by a Potential Based Panel Method. In *Proceedings of the IABEM-90 Symposium of the International Association for Boundary Element Methods*, Rome, Italy.

Kinnas, S. and Fine, N. (1992). A nonlinear boundary element method for the analysis of unsteady propeller sheet cavitation. In *Nineteenth Symposium on Naval Hydrodynamics*, pages 717–737, Seoul, Korea.

Kinnas, S. and Fine, N. E. (1993). A numerical nonlinear analysis of the flow around 2-d and 3-d partially cavitating hydrofoils. *Journal of Fluid Mechanics*, 254:151–181.

Kinnas, S., Griffin, P., Choi, J.-K., and Kosal, E. (1999). Automated design of propulsor blades for high-speed ocean vehicle applications. *Trans. SNAME*, 106.

Kinnas, S., Griffin, P., and Mueller, A. (1997). Computational tools for the analysis and design of high speed propulsors. In *The International CFD Conference*, Ulsteinvik, Norway.

Kinnas, S. and Hsin, C. (1992). A boundary element method for the analysis of the unsteady flow around extreme propeller geometries. *AIAA Journal*, 30(3):688–696.

Kinnas, S., Lee, H., and Mueller, A. (1998). Prediction of propeller blade sheet and developed tip vortex cavitation. In *22nd Symposium on Naval Hydrodynamics*, pages 182–198, Washington, D.C.

Kinnas, S., Mishima, S., and Brewer, W. (1994). Nonlinear analysis of viscous flow around cavitating hydrofoils. In *Twentieth Symposium on Naval Hydrodynamics*, pages 446–465, University of California, Santa Barbara.

Kinnas, S. and Pyo, S. (1997). Propeller wake alignment models in uniform and inclined inflow. In *Propellers/Shafting '97 Symposium*, Virginia Beach, VA. Soc. Naval Arch. & Marine Engnrs.

Kinnas, S. and Pyo, S. (1999). Cavitating propeller analysis including the effects of wake alignment. *Journal of Ship Research*, 43(1):38–47.

Krasny, R. (1986). Desingularization of periodic vortex sheet roll-up. *Journal of Computational Physics*, 65.

Krasny, R. (1987). Computation of vortex sheet roll-up in the Trefftz plane. *Journal of Fluid Mechanics*, 184:123–155.

Kudo, T. and Kinnas, S. (1995). Application of unsteady vortex/source lattice method on supercavitating propellers. In *24th American Towing Tank Conference*, Texas A&M University.

Kuiper, G. (2001). New developments around sheet and tip vortex cavitation on ship propellers. In *CAV 2001: Fourth International Symposium on Cavitation*, Pasadena, CA. California Institute of Technology.

Kuwahara, K. and Takami, H. (1973). Numerical Studies of Two Dimensional Vortex Motion by a System of Point Vortices. *Journal of Physical Society of Japan*, 34:247–253.

185

Lee, C.-S. (1979). *Prediction of Steady and Unsteady Performance of Marine Propellers with or without Cavitation by Numerical Lifting Surface Theory*. PhD thesis, M.I.T., Department of Ocean Engineering.

Lee, C.-S. (1981). Prediction of the transient cavitation on marine propellers. In *Thirteenth Symposium on Naval Hydrodynamics*, pages 41–64, Tokyo, Japan.

Lee, C.-S., Kim, Y.-G., and Lee, J.-T. (1992). A potential-based panel method for the analysis of a two-dimensional super- or partially- cavitating hydrofoil. *Journal of Ship Research*, 36(2):pp. 168–181.

Lee, H. and Kinnas, S. (2001a). Modeling of unsteady blade sheet and developed tip vortex cavitation. In *CAV 2001: Fourth International Symposium on Cavitation*, Pasadena, CA. California Institute of Technology.

Lee, H. and Kinnas, S. (2001b). MPUF3A (version 1.2) user's manual. Ocean Engineering Report 01-2, Ocean Engineering Group, UT Austin, Austin, TX.

Lee, J.-T. (1987). *A Potential Based Panel Method for The Analysis of Marine Propellers in Steady Flow*. PhD thesis, M.I.T., Department of Ocean Engineering.

Lemonnier, H. and Rowe, A. (1988). Another approach in modelling cavitating flows. *Journal of Fluid Mechanics*, vol 195.

Mangler, K. and Smith, J. (1959). A theory of the flow past a slender delta wing with leading-edge separation. In *Proceedings of the Royal Society of London,Series A*, volume 251, pages 200–217.

McCormick, B. (June, 1954). *A Study of the Minimum Pressure in a Trailing Vortex System*. PhD thesis, The Pennsylvania State University.

McCormick, B. J. (1962). On Caviation Produced By a Vortex Trailing From a Lifting Surface. *Journal of Basic Engineering*.

McCune, J., Lam, C., and Scott, M. (1990). Nonlinear aerodynamics of two-dimensional airfoils in severe maneuver. *AIAA Journal*.

Mishima, S. and Kinnas, S. (1996). HPUF-3A version 1.1. User's Manual 96-1, MIT, Department of Ocean Engineering.

Mishima, S., Kinnas, S., and Egnor, D. (1995). The CAvitating PRopeller EXperiment (CAPREX), Phases I & II. Technical report, Department of Ocean Engineering, MIT.

Mokry, M. and Rainbird, W. (1975). Calcualtion of Vortex Sheet Roll-Up in a Rectangular Wind Tunnel. *Journal of Aircraft*, 12:750–752.

Moore, D. (1971). The discrete vortex approximation of a vortex sheet. Technical Report AFOSR-1084-69, Cal. Inst. of Tech. Report.

Moore, D. (1974). A Numerical Study of the Roll-Up of a Finite Vortex Sheet. *Journal of Fluid Mechanics*, 63(2):225–235.

Moore, D. (1975). The rolling up of a semi-infinite vortex sheet. In *Proceedings of the Royal Society of London,Series A*, volume 345, pages 417–430.

Morino, L. and Kuo, C.-C. (1974). Subsonic Potential Aerodynamic for Complex Configurations : A General Theory. *AIAA Journal*, vol 12(no 2):pp 191–197.

Mueller, A. (1998). Development of face and mid-chord cavitation models for the prediction of unsteady cavitation on a propeller. Master's thesis, UT Austin, Dept. of Civil Engineering.

Mueller, A. and Kinnas, S. (1997). Cavitation predictions using a panel method. In *ASME Symposium on Marine Hydrodynamics and Ocean Engineering*, volume 14, pages 127–137, Dallas, TX.

Mueller, A. and Kinnas, S. (1999). Propeller sheet cavitation predictions using a panel method. *Journal of Fluids Engineering*, 121:282–288.

Nagati, M., Iversen, J., and Vogel, J. (1987). Vortex Sheet Modeling with Curved High-Order Panels. *Journal of Aircraft*, 24(11):776–782.

Naubes, B. and Arndt, R. (1997). Tip vortex formation and cavitation. *Journal of Fluids Engineering*, 119:413–419.

Newman, J. N. (1977). *Marine Hydrodynamics*. MIT Press.

Pellone, C. and Rowe, A. (1981). Supercavitating hydrofoils in non-linear theory. In *Third International Conference on Numerical Ship Hydrodynamics*, Paris, France. Basin d'essais des Carènes.

Platzer, G. and Souders, W. (1980). Tip vortex cavitation characteristics and delay on a three-dimensional hydrofoil. In *19th American Towing Tank Conference*.

Pullin, D. (1978). The large-scale structure of unsteady self-similar rolled-up vortex sheets. *Journal of Fluid Mechanics*, 88:401–430.

Pullin, D. and Phillips, W. (1981). On a generalization of kaden's problem. *Journal of Fluid Mech.*, 104.

Pyo, S. (1995). *Numerical Modeling of Propeller Tip Flows with Wake Sheet Roll-Up in Three Dimensions*. PhD thesis, Department of Ocean Engineering, MIT.

Pyo, S. and Kinnas, S. (1997). Propeller wake sheet roll-up modeling in three dimensions. *Journal of Ship Research*, 41(2):81–92.

Ramsey, W. (1996). *Boundary Integral Methods for Lifting Bodies with Vortex Wakes*. PhD thesis, M.I.T., Department of Ocean Engineering.

Rom, J., Almosnino, D., and Gordon, R. (1981). Method for the Calculation of the Non-Linear Aerodynamic Characteristics of Thick Wings and Bodies Including Symmetric Vortex Separation in Subsonic Flows. Technical Report No 437, Department of Aero. Eng., Technion.

Rosenhead, L. (1931). The formation of vortices from a surface of discontinuity. In *Proceedings of the Royal Society of London,Series A*, volume 134, pages 170–192.

Rule, J. and Bliss, D. (1998). Prediction of viscous trailing vortex structure from basic loading parameters. *AIAA Journal*, 36:208–218.

Salvatore, F. and Esposito, P. (2001). An improved boundary element analysis of cavitating three-dimensional hydrofoils. In *CAV 2001: Fourth International Symposium on Cavitation*, Pasadena, CA. California Institute of Technology.

Sarpkaya, T. (1971). On stationary and traveling vortex breakdowns. *Journal of Fluid Mechanics*, 45:545–559.

Schlichting, H. (1979). *Boundary Layer Theory*. McGraw-Hill, Inc.

Smith, J. (1968). Improved calculations of leading-edge seperation from slender, thin, delta wings. In *Proceedings of the Royal Society of London,Series A*, volume 306, pages 67–90.

Smith, J. (1986). Vortex flows in aerodynamics. In *Annual Review of Fluid Mechanics*, volume 18, pages 221–242.

Suciu, E. and Morino, L. (1977). Nonlinear Steady Incompressible Lifting-Surface Analysis with Wake Roll-Up. *AIAA Journal*, 15:54–58.

Szantyr, J. (1994). A method for analysis of cavitating marine propellers in nonuniform flow. *International Shipbuidling Progress*, 41:223–242.

Takami, H. (1964). A numerical experiment with discrete vortex approximation with reference to the rolling up of a vortex sheet. Technical Report SUDAER 202, Dept. of Aero. and Astro., Stanford University.

Tavares, T. and McCune, J. (1993). Aerodynamics of maneuvering slender wings with leading-edge separation. *AIAA Journal*, 31:977–986.

Tulin, M. (1953). Steady Two-Dimensional Cavity Flows About Slender Bodies. Technical Report 834, DTMB.

Tulin, M. (1955). Supercavitating Flow Past Foils and Struts. In *Symposium on Cavitation in Hydrodynamics*, NPL, Tenddington, England.

Tulin, M. and Hsu, C. (1980). New applications of cavity flow theory. In *13th Symposium on Naval Hydrodynamics*, Tokyo, Japan.

Uhlman, J. (1987). The surface singularity method applied to partially cavitating hydrofoils. *Journal of Ship Research*, 31(No. 2):107–124.

Uhlman, J. (1989). The surface singularity or boundary integral method applied to supercavitating hydrofoils. *Journal of Ship Research*, 33(No. 1):16–20.

Westwater, F. (1935). Rolling Up of the Surface of Discontinuity Behind an Aerofoil of Finite Span. *Aeronautical Research Council, R & M (No 1962)*.

Widnall, S. (1966). Unsteady Loads on Supercavitating Hydrofoils. *Journal of Ship Research*, 9:pp. 107–118.

Young, Y. and Kinnas, S. (1999a). Hllfpp (version 1.2), hull field point potential, user's manual. Ocean Engineering Report 99-6, Department of Civil Engin., The Univ. of Texas at Austin, Austin, TX.

Young, Y. and Kinnas, S. (1999b). Numerical and experimental validation of a cavitating propeller bem code. In *Cavitation and Multiphase Flow Forum*, San Fransisco, CA. 3rd ASME/JSME Joint Fluids Engineering Conference.

Young, Y. and Kinnas, S. (2001a). A bem for the prediction of unsteady midchord face and/or back propeller cavitation. *Journal of Fluids Engineering*, 123.

Young, Y. and Kinnas, S. (2001b). Numerical modeling of supercavitating and surface-piercing propeller flows. In *CAV 2001: Fourth International Symposium on Cavitation*, Pasadena, CA. California Institute of Technology.

Young, Y. and Kinnas, S. (2002). Numerical modeling of supercavitating propeller flows. *Journal of Ship Research*, Accepted for publication.

Young, Y., Lee, H., and Kinnas, S. (2001). PROPCAV (version 1.2) user's manual. Ocean Engineering Report 01-4, Ocean Engineering Group, UT Austin, Austin, TX.

Young, Y. L. (2002). *Numerical Modeling of Supercavitating and Surface-Piercing Propellers*. PhD thesis, Department of Civil Engineering, The University of Texas at Austin.

Zhu, P., Shou, W., and Luo, S. (1981). Nonlinear predictions of subsonic aerodynamic loads on wings and bodies at high angles of attack. *Computational Methods for Applied Mechanical Engineering*, 26:305–319.

Vita

Hanseong Lee was born in Woonju, South Korea on April 20, 1965, the son of Kwansoo and Ilsun Kwon. He graduated from Jeonra High School, Jeonju in February 1984. He received a Bachelor of Science degree at the department of Ocean Engineering and Naval Architecture of Seoul National University in February 1988, and completed Masters degree at the same university in 1990. After he finished his graduate school, he worked for Agency for Defense Development (ADD) as a researcher from 1990 through 1996. He started his doctoral study at ASE/EM department in the University of Texas at Austin in 1996, and transfered to the Ocean Engineering Group at the Civil Engineering Department in 1997.

Permanent address: 234 Jangsunri Woonjumyun Wanjugoon, Jeonbook,
Korea

This dissertation was typeset with LaTeX† by the author.

---

†LaTeX is a document preparation system developed by Leslie Lamport as a special version of Donald Knuth's TeX Program.